Latitudinal distribution and magnetic signatures of magnetospheric substorms

Pro Gradu

Jussi Laitinen

Physics Degree Programme
Space Physics and Astronomy research unit
Space Climate research group
University of Oulu

9.12.2022

Contents

1 Introduction

Near-Earth space is governed by the Earth's magnetic field, shielding the Earth from the continuous stream of plasma from the Sun, called the solar wind. The Earth's magnetic field forms a magnetic cavity inside the solar wind, called the magnetosphere. The magnetosphere is not closed, but is constantly opened at the dayside, as the interplanetary magnetic field carried by the solar wind interacts and reconnects with the Earth's dayside magnetic field. This leads to geomagnetic activity, as the magnetic topology of the magnetosphere changes due to the reconnection and flow of the solar wind. The intensity of geomagnetic activity depends on the energy input of the solar wind, which depends on the activity of the Sun. The energy input of the solar wind increases strongly during transient events, e.g., coronal mass ejections and high speed streams.

The magnetosphere has a systemic way of unloading the loaded energy from the solar wind, called the magnetospheric substorm. Substorms happen at the night side of the magnetosphere in the tail of the magnetosphere, called the magnetotail. Substorms are violent and explosive releases of energy, where the inner magnetic field lines of the magnetotail go through topological changes due to reconnection. Substorms are associated with field-aligned currents (FAC) and particle precipitation. The FAC divert magnetospheric currents into and out of the ionosphere, connecting to the westward auroral electrojet, which is an ionospheric current flowing horizontally closing upward and downward FAC. The westward electrojet enhances during the substorm expansion phase. The increased particle precipitation leads to glorious visual phenomenon known as the aurorae. The aurorae go through distinct morphological changes during each substorm.

The enhanced westward electrojet depresses the Earth's magnetic field. This depression can be seen in ground-based magnetic field measurements at auroral latitudes. Thus, geomagnetic indices can be formed to describe the activity of the westward (and eastward) electrojet. The depressions are systematic enough, so that they can be found from geomagnetic indices using an automated algorithmic approach. In this thesis, a geomagnetic index called the IL index is formed using the IMAGE magnetometer network. A substorm identification algorithm is defined and implemented to form a list of substorms found in the IL index. The solar cycle and seasonal variation of substorm number, duration and amplitude are studied. Their correlations with the solar cycle, yearly solar wind speed and IMF intensity, and occurrence of transient events (coronal mass ejections and high speed streams) is studied on a yearly scale. Latitudinal distribution of the substorms is studied using a subset of eleven stations from the IMAGE network. A standardized $IL(st)$ index is created for each station in the subset. Magnetic signatures in the $IL(st)$ indices during substorms are studied with superposed epoch analysis. A substorm identification algorithm is implemented and eleven substorm lists are created from the $IL(st)$ indices.

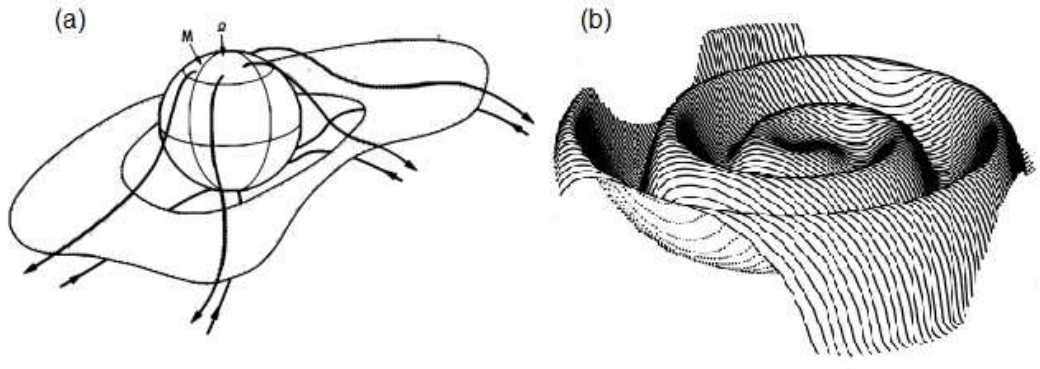

Figure 1: (**a**) Illustration of the heliospheric current sheet between the oppositely directed IMF field lines at the equator (Smith & Tsurutani, 1978). (**b**) An illustration of the wavy nature of the HCS (Jokipii & Thomas, 1981).

2 Solar wind

Solar wind is continuous stream of high conducting plasma flowing from the Sun. It is the Sun's corona expanding radially, filling the whole solar system and interacting with the bodies within. The solar wind plasma forms the so called heliosphere (Kivelson & Russell, 1995; Russell et al., 2017). Due to the frozen-in theorem of high conducting plasmas, the Sun's photospheric magnetic field travels along with the plasma, resulting to the solar wind to have magnetic properties. This magnetic field that travels along with the solar wind plasma, is called the interplanetary magnetic field (IMF), or the heliospheric magnetic field (HMF) (Owens & Forsyth, 2013).

Figure 1a shows the large-scale structure of the Sun's magnetic field. Due to the Sun's magnetic dipole being tilted compared to the rotation axis, the open IMF field lines will create a wavy heliospheric current sheet (HCS) between the oppositely directed magnetic field lines, as seen in Figure 1b. Figure 1b also shows the spiral nature of the HCS, which is due to the spiral nature of the IMF field lines. The IMF field lines can be modeled via the Archimedean spiral in the equatorial plane. The spiral of the heliospheric field lines is also known as the Parker spiral (Parker, 1958). The Parker spiral models the IMF carried by the solar wind in a steady state, i.e., as idealized plasma with an exactly radial outflow of constant speed, independent of radial and latitudinal position. However in reality, the properties of the solar wind vary with the activity of the Sun, especially during transient events, e.g., coronal mass ejections (CMEs) (Forbes, 2000) and high speed streams (HSS) from coronal holes (Zirker, 1977).

2.1 Coronal mass ejections

CMEs, or interplanetary CMEs (ICMEs) if detected in the heliosphere, are large-scale plasma ejections from the lower corona of the Sun. Figure 2a shows a schematic of an

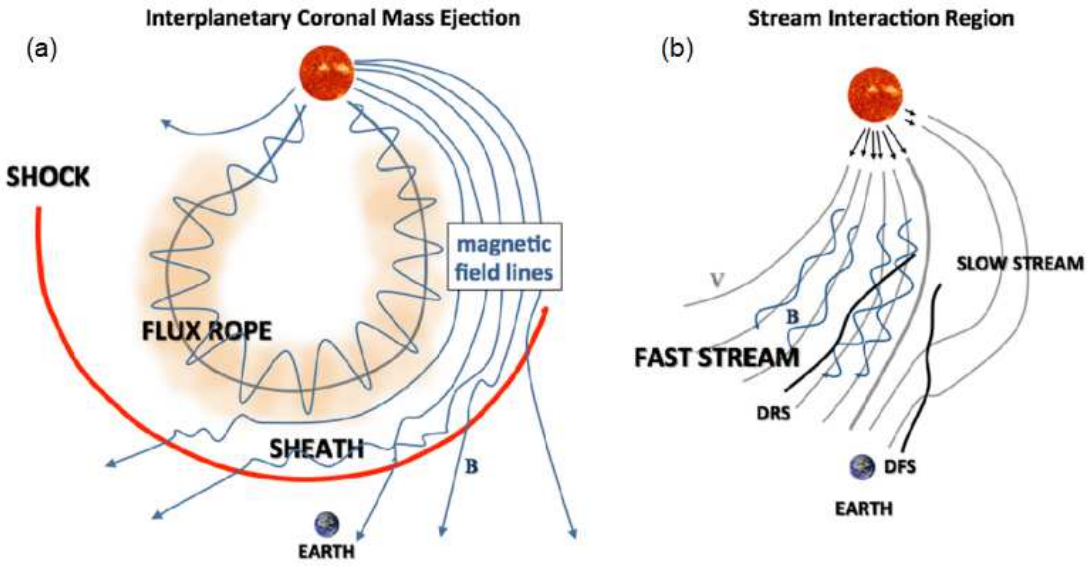

Figure 2: (**a**) schematic of an Interplanetary Coronal Mass Ejection (ICME) and the associated shock (red arc) and sheath. The ICME here is accompanied with a magnetic cloud or a flux rope structure. It's important to note that not all ICMEs are fast enough to have shocks and clear sheaths. (**b**) schematic of a Co-rotating Interaction Region (CIR). Near Earth orbit CIRs are typically bounded by a developing fast forward-fast reverse shock pair (DFS and DRS) (Kilpua et al., 2017).

CME. As the CME erupts, its velocity can exceed the slower velocity of the upstream plasma. If the velocity difference between the CME front and the surrounding plasma is greater than the local magnetosonic speed, a shock will form ahead of the CME that propagates supersonically into the upstream solar wind. The CME sheath will form between the CME front and the shock. Figure 2a also shows a magnetic cloud structure. Magnetic clouds are a subset of CMEs (Burlaga et al., 1981). Only one third or less of CMEs shows clear indications of magnetic clouds. This is most often due to the measuring station located at the edge of the magnetic cloud, which results to weaker, unclear magnetic signatures (Balogh & Erdõs, 2013; Kilpua et al., 2017). The magnetic structure of the magnetic cloud can also deform as it flows through the interplanetary medium. Magnetic clouds are modelled as force-free magnetic flux robes, where the current density is proportional to the magnetic field everywhere, thus with Ampère's law (Lepping et al., 1990)

$$\nabla \times \mathbf{B} = \mu_0 \mathbf{J} = \alpha \mathbf{B}, \tag{2.1}$$

where the coefficient α is a function of position, $\mathbf{J}$ is the current density and $\mathbf{B}$ is the magnetic field.

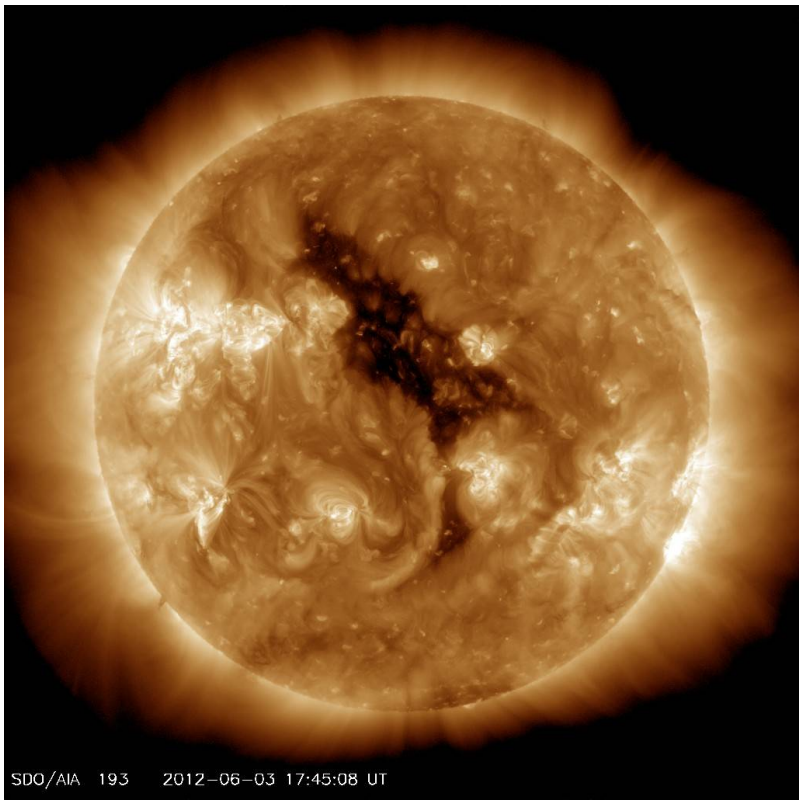

Figure 3: An image of a coronal hole on the Sun. The image is from the Solar Dynamics Observatory (SDO) (`https://www.nasa.gov/multimedia/imagegallery/image_feature_2268.html`).

2.2 Coronal holes and high speed streams

Coronal holes, the source of the HSS co-rotate with the Sun, typically lasting several rotations. Thus, a HSS is seen at 1 AU in 27 day periods with each solar rotation. Figure 3 shows an image of a coronal hole on the Sun. HSS form regions of compressed magnetic fields and plasma, as the fast solar wind ($750 - 800\,\mathrm{km/s}$) reaches the slower solar wind ahead ($300 - 400\,\mathrm{km/s}$). These regions are called co-rotating interaction regions (CIR). Figure 2b shows a schematic of fast solar wind and a CIR. The CIR is between the interfaces of the fast and slow solar wind, where the compression enhances the magnetic field and plasma pressure. Typically a fast forward-fast reverse shock pair is developed, that bounds the CIR between them. HSS are associated with Alfvén waves propagating parallel to the magnetic field line. These Alfvén waves can have peak-to-peak amplitude of 1-2 times the background magnetic field, thus creating large magnetic fluctuations in the fast solar wind together with the compressed magnetic field (Tsurutani et al., 2006).

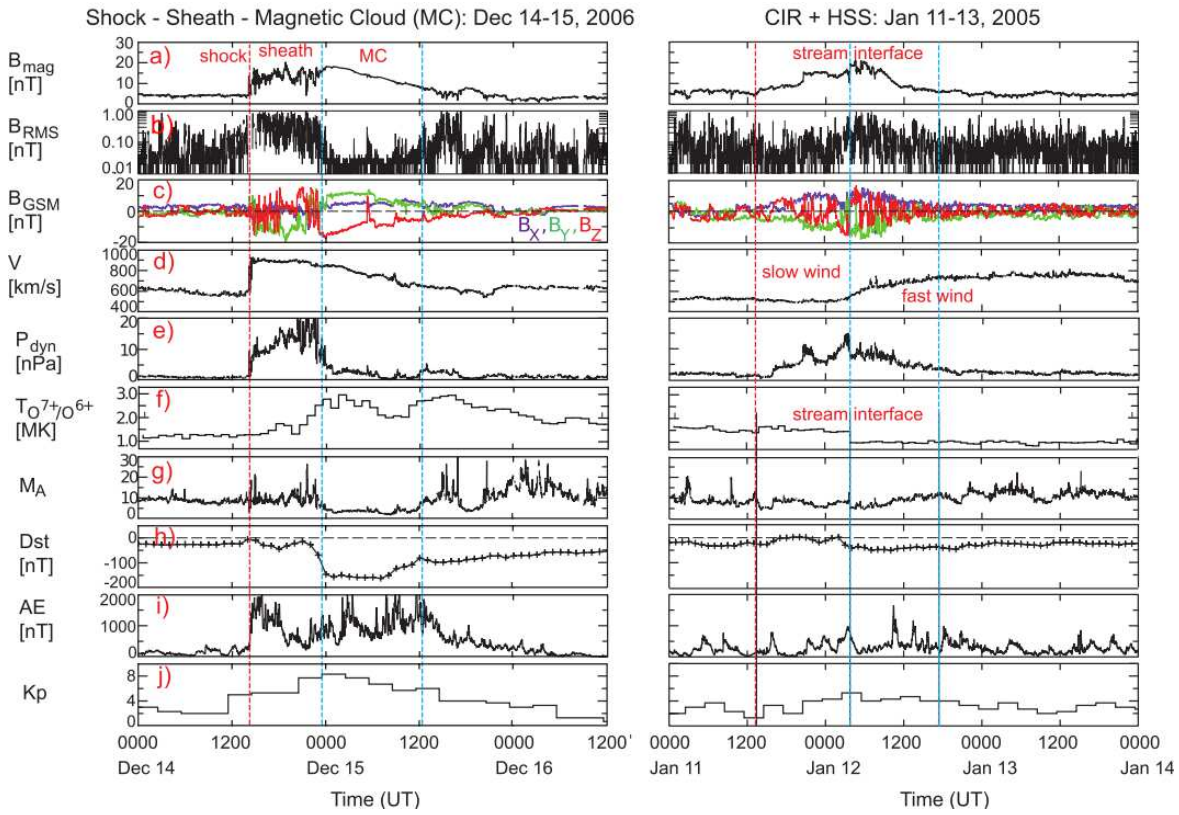

Figure 4: Solar wind measurements and geomagnetic response from OMNI database. Left: CME on 14-15 December 2006; right: CIR on 11-13 January 2005. Panels (**a**) shows the solar wind magnetic field magnitude. (**b**) the root-mean-square (RMS) of the solar wind magnetic field magnitude; (**c**) the IMF components in the GSM coordinates; (**d**) solar wind speed; (**e**) the dynamical pressure of the solar wind; (**f**) O^{7+}/O^{6+} ratio (CIR ratio is multiplied by a factor of ten); (**g**) Alfvén Mach number (the ratio of the solar wind speed and the Alfvén speed); (**h**) Dst index; (**i**) AE index; (**j**) Kp index. Solar wind and AE measurements have 1-minute resolution and Dst and Kp 1-hour resolution. On the left the red dashed line shows the CME shock. Between the red and blue dashed line is the sheath and between the blue dashed lines is the magnetic cloud. On the right the vertical lines show in order the start of the CIR, the stream interface and the end of the CIR. Solar wind speed is slow before the interface and fast after. Left and right panels have the same scales (Kilpua et al., 2017).

2.3 Solar wind at 1 AU

Figure 4 shows spacecraft measurements (from OMNI database) of the solar wind properties at 1 AU during an CME with a shock, sheath and a magnetic cloud (left column) and during a CIR associated HSS (right column). Figure 4a shows the solar wind magnetic field magnitude B_{mag}. In the case of the CME, the B_{mag} stays unchanged until the shock, when it increases abruptly and is about $10 - 15\,\mathrm{nT}$ during

the sheath phase. Large magnetic fluctuations are seen during the sheath. As the magnetic cloud arrives, the B_{mag} increases slightly, and then decreases steadily. Fluctuations are much smaller in the magnetic cloud. In the case of the CIR and HSS, the B_{mag} increases rather steadily towards the stream interface prior to the fast solar wind. The B_{mag} peaks slightly after the interface, and decreases after the CIR. In Figure 4b, in the case of the CME, the root-mean-square (RMS) of the magnetic field magnitude B_{RMS} increases before the shock, stays high during the sheath phase and decreases abruptly during the magnetic cloud. In the case of the CIR and HSS, the B_{RMS} increases slightly prior to the stream interface and decreases thereafter.

Figure 4c shows the B components in geocentric solar magnetospheric (GSM) coordinates, which is a cartesian coordinate system, with the origin being in the center of the Earth, X pointing towards the Sun, Z pointing towards the geomagnetic north perpendicular to X, and Y being their cross product pointing approximately towards dusk. In the case of the CME, the components are slightly disturbed before the shock and get strongly disturbed at the shock. As the magnetic cloud arrives, the B_X remains roughly constant, the B_Y is positive but slowly decreasing, and the B_Z is negative and slowly increasing, (and has a large positive spike in the half way of the cloud). These changes denote the typical rotation of the IMF within the cloud. In the case of the CIR and HSS, B_Y and B_Z fluctuate increasingly towards the stream interface. After the interface, the fluctuations slowly decrease.

In Figure 4d, in the case of the CME, the solar wind speed v increases abruptly to $\sim 900\,\mathrm{km/s}$ at the shock, and stays high during the sheath phase. At the magnetic cloud, the v decreases steadily. The v stays slightly increased long after the CME. In the case of the CIR and HSS, the v is low ($\sim 450\,\mathrm{km/s}$) before the interface, and increases steadily to $\sim 700\,\mathrm{km/s}$ after the interface.

In Figure 4e, in the case of the CME, the dynamical pressure P_{dyn} stays very small until the shock, but increases abruptly at the arrival of the shock. The P_{dyn} keeps increasing during the sheath phase, and fluctuates between 10 and 20 nPa at the end of the sheath. As the magnetic cloud arrives, the P_{dyn} decreases abruptly to low values. In the case of the CIR and HSS, the P_{dyn} starts increasing prior to the interface, as the v is still low, but the magnetic fields and plasma density start increasing. After the interface the P_{dyn} decreases steadily but slowly to small value.

In Figure 4f, in the case of the CME, the oxygen ion charge state ratio $T_{O^{7+}/O^{6+}}$ stays unchanged through the shock, and increases towards the end of the sheath phase to $\sim 2.5\,\mathrm{MK}$. The $T_{O^{7+}/O^{6+}}$ remains high $\sim 2-3\,\mathrm{MK}$ during the magnetic cloud, and even long thereafter. In the case of the CIR and HSS, the $T_{O^{7+}/O^{6+}}$ stays unchanged at $\sim 1.5\,\mathrm{MK}$ before the stream interface, and abruptly drops to $\sim 1\,\mathrm{MK}$, where it stays relatively unchanged. $T_{O^{7+}/O^{6+}}$ shows the origin of the solar wind of such temperature. Higher $T_{O^{7+}/O^{6+}}$ means that the origin is from solar corona of higher temperature. Figure 4f shows that the $T_{O^{7+}/O^{6+}}$ is higher in the case of the CME, than in the case of the CIR and HSS. This means that the origin of the CME is from the corona with the higher temperature. Correspondingly, in the case of the CIR and HSS the abrupt

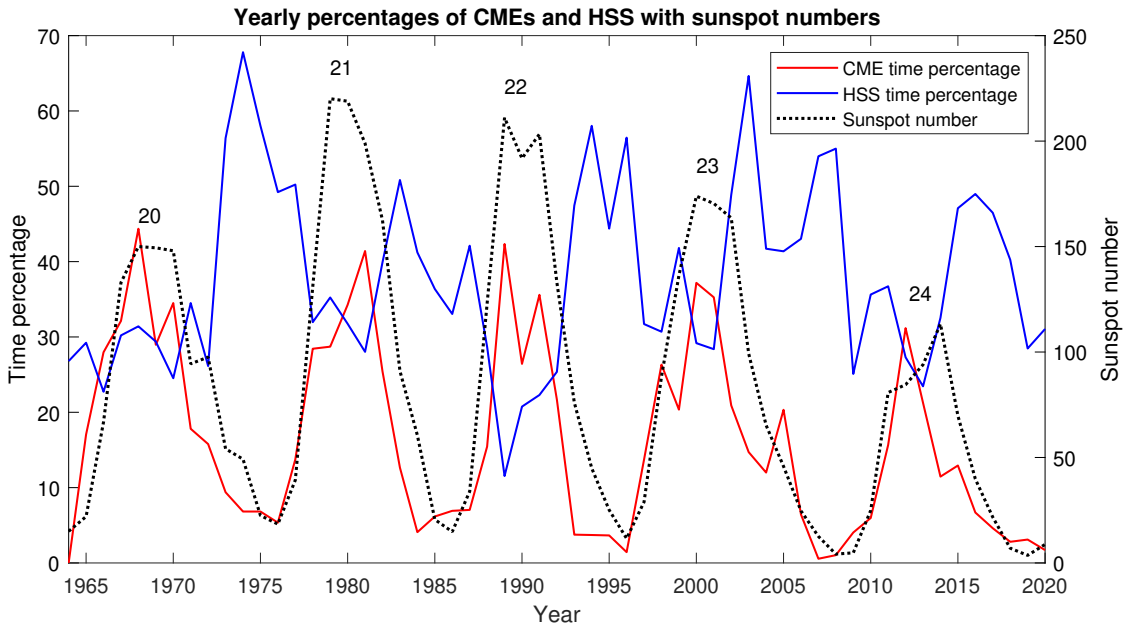

Figure 5: Yearly percentages of time when CME-associated flows and high-speed streams were present. Sunspot numbers for years 1964-2020 (solar cycles 20-24) (`https://www.sidc.be/silso/`).

drop at the stream interface shows that the HSS is from corona with lower temperature (coronal hole).

In Figure 4g, in the case of the CME, the Alfvén Mach number M_A, which is the ratio of the solar wind speed and the Alfven speed, stays roughly unchanged at 10 through the shock, while starting to fluctuate between $10 - 20$ in the sheath. As the magnetic cloud arrives, the M_A decreases to about zero, where it stays relatively unchanged with little fluctuation. In the case of the CIR and HSS, the M_A stays more stable during the CIR, than during the slow wind before, or in the fast wind after the CIR.

Figures 4h-4j show the geomagnetic response to these two events, via three geomagnetic indices: Dst, AE and Kp. The general picture is that during the CME, the geomagnetic response is considerably larger than during the CIR. Especially the ring current Dst index is affected considerably more during the CME, than during the CIR, which indicates larger geomagnetic storm during the CME. The auroral AE index and the planetary Kp index also show larger deviations during the CME than the CIR. These results can be generalized so that CMEs typically produce larger geomagnetic activity than CIR. However, CIRs are capable of producing elongated periods of enhanced geomagnetic activity, albeit more weaker in nature than geomagnetic storms. Often, this activity is in the form of recurring substorms. This is seen in Figure 4i, where in the case of the CIR and HSS the activity in the AE index is stronger at the end, while in the case of the CME the activity of the AE index decreases after the magnetic cloud.

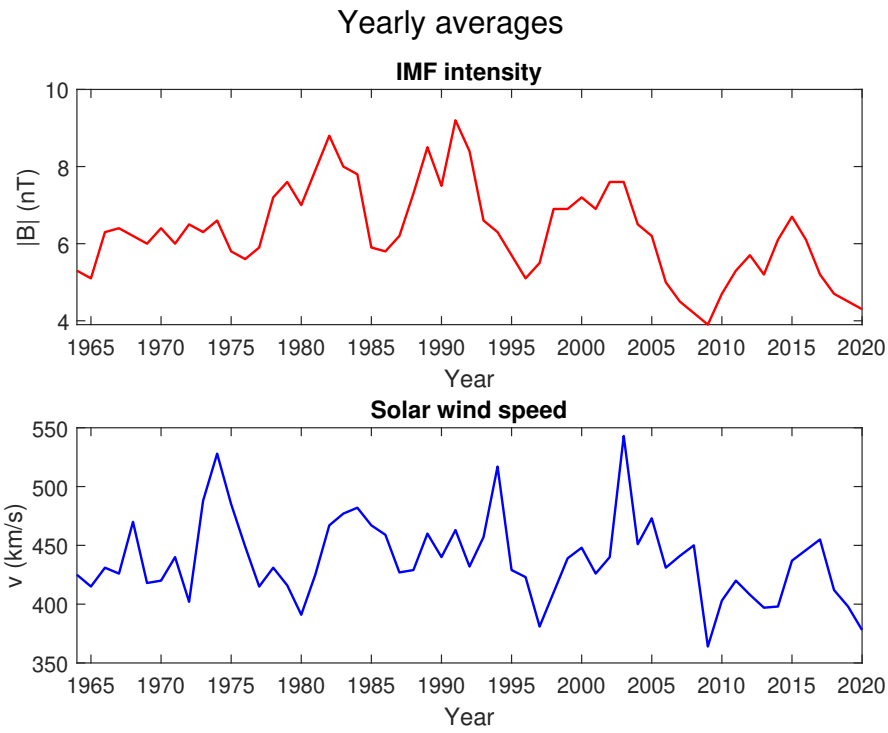

Figure 6: The IMF and solar wind speed during the space age. Yearly averages of the near-Earth IMF scalar magnetic field intensity from the OMNI dataset (`https://omniweb.gsfc.nasa.gov/`).

2.4 Solar cycle variation

The Sun's magnetic activity changes in 11-year periods, known as the solar cycle. The cycle is divided into four phases: the solar minimum, the ascending phase, the solar maximum and the declining phase. The cycles are defined to start at the minimum and to end at the next minimum. At the maximum of every cycle, the polarity of the Sun's long-scale magnetic field is flipped. Sunspot number is the primary parameter defining the solar cycle (Hathaway, 2015).

During the minimum phase of the cycle, the Sun's magnetic activity is weaker, and so is the geomagnetic activity. At the minimum phases the IMF is well approximated with a dipolar-like magnetic field. At the poles, the unipolar magnetic fields give favorable conditions for coronal holes. CMEs are less frequent during this period. As the cycle progresses towards the solar maximum, the magnetic structure gets more complex, and the number of CMEs increases. After the maximum, at the declining phase, the HSS are seen at the Earth more frequently, because the polar coronal holes have extensions to lower latitudes. Figure 5 shows the yearly time percentages of CMEs and HSSs throughout the solar cycle during the years 1964-2020 (solar cycles 20-24). The CME and HSS times are from a list of solar wind types by Richardson et al. (2000, 2002). The percentage of the CMEs correlates with the sunspot number. At the solar maxima, roughly 30-40% of solar wind are CMEs, while at the solar minima,

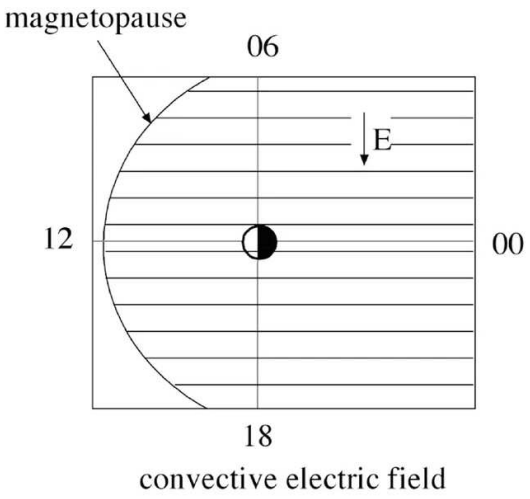

Figure 7: Equipotential lines of the convection electric field in the equatorial plane, with local times (Koskinen, 2011).

CMEs are nearly absent. HSSs are more present throughout the whole solar cycle. Their percentage maximizes during the declining phase of the cycles, when roughly 50-65% of the solar wind type are HSS, depending on the cycle. HSS time percentages decrease to roughly 15-30% during the solar maxima.

Figure 6 shows the yearly averages of the IMF intensity and the solar wind speed in 1965-2020 (King & Papitashvili, 2005). The IMF intensity roughly follows the solar cycle, however lagging sunspots slightly and reaching its peaks during the early declining phases. This time lag is due to the convection of the magnetic field from the intensification of the solar surface magnetic field at the solar maximum to the open magnetic field (IMF), which spreads into the heliosphere along the solar wind. The solar wind speed maximizes at the late declining phase of the solar cycle. This, agrees with the combined CME and HSS percentages in Figure 5, since both add to the mean solar wind speed due to associated fast flows. The IMF intensity and the solar wind speed also contribute to the electric field, known as the convection electric field (Russell et al., 2017)

$$\mathbf{E} = -\mathbf{v}_{sw} \times \mathbf{B}_{sw}, \tag{2.2}$$

where $\mathbf{v}_{sw}$ is the solar wind velocity and $\mathbf{B}_{sw}$ is the IMF. Figure 7 shows the equipotential lines of the convection electric field in the Earth's magnetosphere. The electric field is eastward, when the IMF is southward (the convection ($\mathbf{v}_{sw}$) is anti-sunward).

3 Earth's magnetosphere

The Earth's internal dynamo produces a nearly dipolar magnetic field. The field lines of this magnetic field reach into the surrounding space of the Earth, producing a

region of near-Earth space called the magnetosphere, where the Earth's magnetic field dominates, and is thus in control of the plasma and currents.

The magnetosphere is in constant interaction with the solar wind and the IMF. The dynamics of the solar wind interaction is connected to the magnetospheric dynamics at all scales. Thus, physics of the magnetosphere forms one of the main parts of the field of space physics (Kivelson & Russell, 1995; Russell et al., 2017).

3.1 Structure

Due to the interaction with the solar wind and the IMF, the Earth's magnetic field loses its dipolar structure. The dayside magnetosphere is slightly compressed due to the pressure from the solar wind, settling at a distance $\sim 10.3R_E$ (R_E is the Earth radius) during a quiet time (Petrinec & Russell, 1996). The nightside is greatly stretched, resulting to a long tail for the magnetosphere called the magnetotail, reaching even beyond the Moon's orbit ($\sim 60R_E$) (Ness, 1965). The boundary region between the Earth's magnetosphere and the solar wind is called the magnetopause. The solar wind is supersonic, thus a bow shock is formed in front of the magnetosphere as the magnetosphere becomes an obstacle: a magnetic cavity immersed into the solar wind plasma. The shock front slows down, compresses and heats the solar wind plasma. The region between the bow shock and the magnetosphere is called the magnetosheath, where the heated and compressed plasma is no longer supersonic (Ganushkina et al., 2018).

Figure 8 shows a schematic of the global configuration of the magnetosphere, along with the large-scale current systems in the magnetosphere. At the dayside, the magnetopause current exists due to the effect of the Earth's magnetic field lines on the solar wind plasma particles. Once affected by the Earth's magnetic field via the Lorentz force, positive particles (protons and heavier ions), and negative particles (electrons) move to opposite directions. This separation of particles creates an eastward current in the dayside magnetopause, called the Chapman-Ferraro current (Chapman & Ferraro, 1931; Cahill & Amazeen, 1963; Ganushkina et al., 2018). In the nightside, the magnetotail current known as the cross-tail current flows across the tail near the equatorial plane, where the oppositely directed magnetic field lines maintain a current. The currents in the nightside magnetopause exist largely due to the cross-tail current splitting to up and downward directions, as it reaches the western edge of the magnetotail. Physically, the current has to flow somewhere, thus creating the half cylinder current loops as seen in Figure 9, as the cross-tail current connects to the magnetopause current (Axford et al., 1965).

Closer to Earth, the convection and corotation electric fields and the Earth's dipolar magnetic field play a stronger role in the movement of charged particles. The inner magnetosphere holds four plasma regions: the plasma sheet, the ring current, the radiation belts and the plasmasphere. Each of the plasma populations have slightly different properties of energy and density.

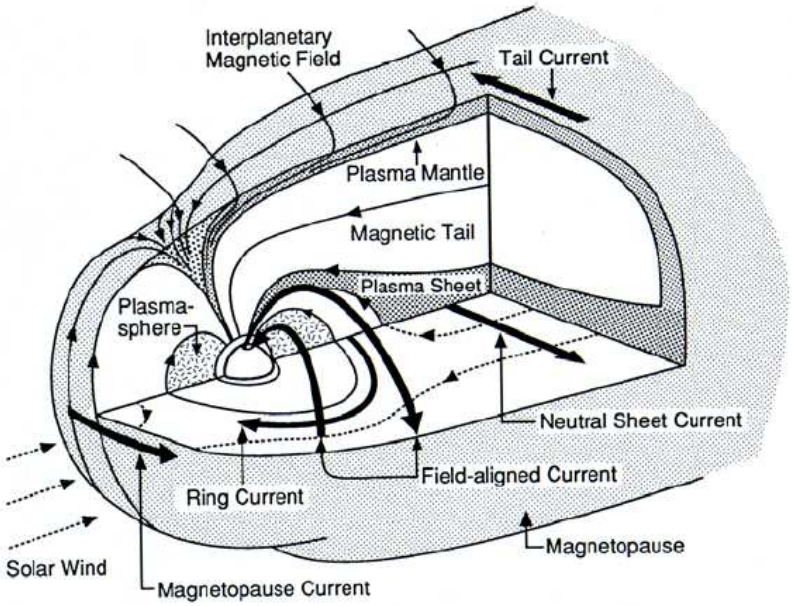

Figure 8: A schematic of the structure of the Earth's magnetosphere under the effect of the solar wind. The schematic shows the large scale current systems in the magnetosphere: the magnetopause currents (Chapman-Ferraro current and the tail current), the cross-tail current (neutral sheet current in the figure), field-aligned currents and the ring current. Plasma mantle, plasma sheet and the plasmasphere are shown as well (Kivelson & Russell, 1995).

3.1.1 Plasma sheet

Due to the stretched configuration of the magnetotail, there occurs an abrupt change of magnetic field direction in the equatorial plane, dividing the magnetotail into two lobes. The cross-tail current flows as a current sheet in the equatorial plane, between these two tail lobes. The cross-tail current implies that the middle of the tail is filled with plasma of enhanced density and energy, preventing the stretched configuration from collapsing. This plasma population, located in the vicinity of the current sheet is called the plasma sheet (Bame et al., 1967). The plasma sheet has a thickness of $4-6R_E$ (at $\sim 17R_E$ midnight meridian), while the current sheet is relatively thin, only 500-5000 km thick. Figure 8 gives an illustration of the location of the plasma sheet near the cross-tail current sheet.

The energy densities of the plasma sheet vary both spatially and temporally. Electrons have a usual (thermal) energy of $100-500\,\mathrm{eV}$ and protons $1-5\,\mathrm{keV}$. The particles usually have a kappa-type energy distribution (quasi-Maxwellian at low energies, power-law at high energies) (Christon et al., 1988). The plasma sheet has dynamical features that change the spatial distribution of the plasma, such as bursty bulk flows (Angelopoulos et al., 1992) flowing earthward and tailward. The energy distributions can vary from event to event, but during the event the distribution maintains its shape.

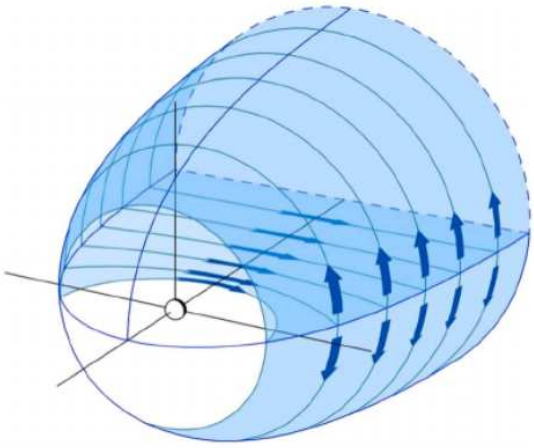

Figure 9: An illustration of the magnetopause currents around the magnetotail. The cross-tail current spreads into up and down directions at the western edge of the magnetotail. (Ganushkina et al., 2018)

3.1.2 Ring current

The ring current is a westward current, flowing at $4-7R_e$ around the Earth. At $\sim 3R_e$ there exists a weak eastward ring current circulating the Earth in the counterclockwise direction (Le et al., 2004). The ring current consists of energetic (10-100 keV) magnetically trapped charged particles, mainly protons from the solar wind. Solar wind plasma gets injected into the Earth's magnetosphere, mainly into the magnetotail. The Earth's ionosphere is also a significant source, due to the magnetosphere-ionosphere coupling. The ionospheric source is responsible for the heavy O^+ and He^+ ions that dominate the ring current during large storms. These particles start to circulate the Earth via gradient and curvature drifts. In 1957 Parker derived an equation for the current density perpendicular to the magnetic field, under static conditions in the case of anisotropic plasma pressure (Lui et al., 1987; Daglis et al., 1999; Ganushkina et al., 2015)

$$\mathbf{J}_\perp = \frac{\mathbf{B}}{B^2} \times \left(\nabla p_\perp + (p_\parallel - p_\perp) \frac{(\mathbf{B} \cdot \nabla)\mathbf{B}}{B^2} \right), \tag{3.1}$$

where the $p_\parallel$ and $p_\perp$ are the plasma pressure components parallel and perpendicular to the magnetic field. In the case of isotropic pressure p this equation can be further simplified to

$$\mathbf{J}_\perp = \frac{\mathbf{B} \times \nabla p}{B^2}. \tag{3.2}$$

Equation (3.2) describes a perpendicular current in a magnetohydrostatic balance. Thus it is a direct result from the MHD momentum equation in the case of static

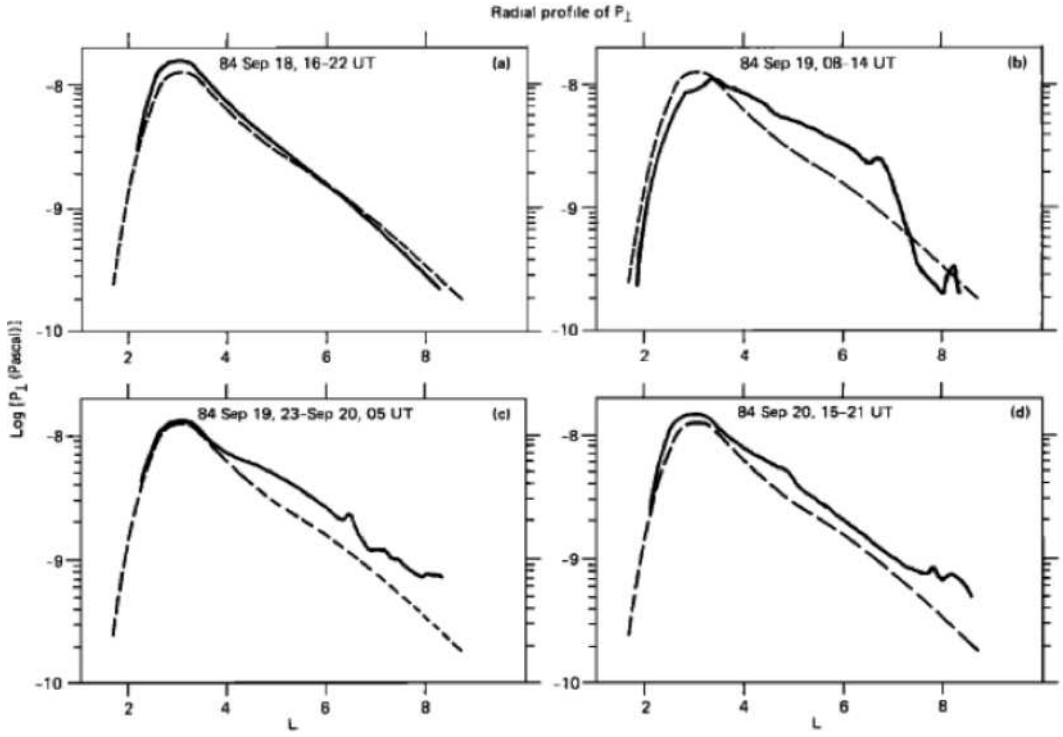

Figure 10: The radial profiles of the particle pressure perpendicular to the magnetic field from four consecutive passes of AMPTE spacecraft during the 18–20 September 1984 storm (Lui et al., 1987).

plasma

$$\mathbf{J} \times \mathbf{B} = \nabla p. \tag{3.3}$$

Equation (3.1) justifies the westward and eastward currents, since the plasma pressure peaks roughly at $3.5R_E$ (Jorgensen et al., 2004; Ganushkina et al., 2015). An example of a plasma pressure distribution during a three day storm (in 1984) can be seen in Figure 10. Such a pressure distribution can result to a ring current consisting of both eastward and westward components. Figure 11 shows a statistical mapping of the intensity of the ring current with four different Dst^* levels, and shows a weak eastward current at $\sim 3R_E$. One should note that the ring current is asymmetric in local time, so not a "ring". The eastward ring current has an intensity of $\sim 2\,\mathrm{nA/m^2}$ during both quiet and storm times, while the westward ring current has a quiet time intensity of $\sim 1 - 4\,\mathrm{nA/m^2}$, but during storms it grows to $\sim 7\,\mathrm{nA/m^2}$, and can reach even higher intensities during larger storms. Also, as seen in Figure 11, the eastward ring current is much smaller in size (smaller surface area $\mathrm{m^2}$) compared to the westward ring current. Thus, the westward ring current dominates the total effect of the two ring currents. The growth of the westward ring current has a fundamental part in the research of magnetospheric physics. The ring current reacts to the increased energy input of the solar wind upon to the magnetosphere, which makes it a good indicator for the storm-time activity of the magnetosphere. As the ring current grows, a

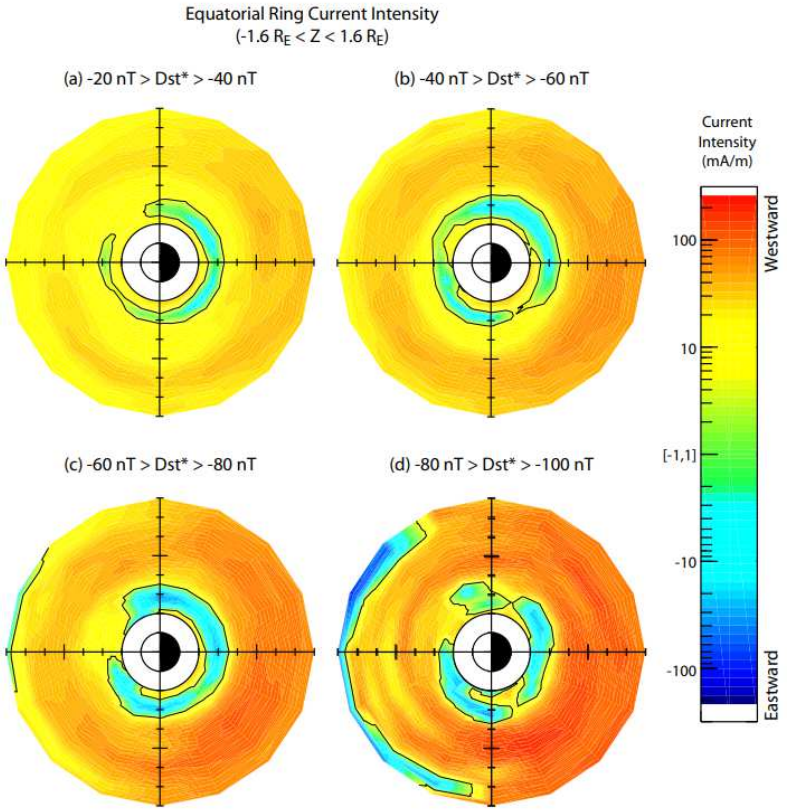

Figure 11: Equatorial ring current intensity as a function of magnetic local time and distance from the dipole axis for each of the four Dst^* levels. 12 LT is at the left side and 00 LT is at the right side of each figure. Color bar has a logarithmic scale (Le et al., 2004).

magnetic field that weakens the magnetic field on the ground grows simultaneously via the Ampère's law. The depression of the magnetic field can be detected on the surface of the Earth with magnetometers at low latitudes. Indices describing this depression (ring current intensity) have been created, e.g., the Dst index (Sugiura, 1964) and its corrected and extended versions, the Dxt and Dcx indices (Karinen & Mursula, 2005, 2006).

3.1.3 Radiation belts

The Earth's dipolar magnetic field has an ability to trap energetic particles in a so called magnetic bottle, via a magnetic mirror. In 1958 Van Allen proved that this was indeed the case for the dipolar magnetic field near the Earth (Allen et al., 1958).

The magnetic mirror rises from the first adiabatic invariant (magnetic moment)

$$\mu = \frac{W \sin^2 \alpha}{B}, \tag{3.4}$$

where W is the kinetic energy, α is the pitch angle and B is the magnetic field intensity.

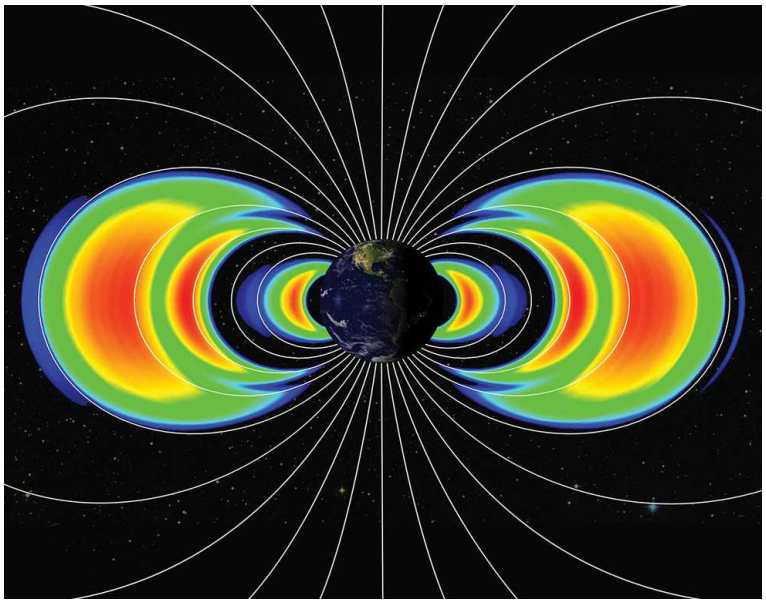

Figure 12: Illustration of the inner and outer radiation belts (NASA Goddard Space Flight Center).

Now if the magnetic moment μ is conserved, between points 1 and 2

$$\frac{\sin^2 \alpha_2}{\sin^2 \alpha_1} = \frac{B_2}{B_1}. \tag{3.5}$$

If the second point has a pitch angle of $\alpha_2 = \alpha_m = 90°$, the equation reduces to

$$\sin \alpha_0 = \sqrt{\frac{B_0}{B_m}}, \tag{3.6}$$

which describes the magnetic mirror, and gives connection between the pitch angle and the magnetic field value where mirroring happens.

The radiation belts consists of two parts as seen in Figure 12. The smaller inner belt is at a distance $2R_E$, and consists of highly energetic (MeV) protons. It is produced by the Cosmic Ray Albedo Neutron Decay (CRAND) mechanism (Singer, 1958), where the cosmic rays hit the neutral atmosphere, producing neutrons with 15-min half life. These neutrons decay to protons in space, which form the belt.

The outer radiation belt is much more dynamical due to injection of energetic (keV-MeV) electrons into the inner magnetosphere. The outer belt is also much larger than the inner belt, extending to distance from $3R_E$ to $7 - 10R_E$, thus partly overlapping with the ring current. A small part overlaps with the inner proton belt as well (Koskinen & Kilpua, 2022).

3.1.4 Plasmasphere

The innermost region of the magnetosphere is the Earth's plasmasphere. The basis for the model of the plasmasphere comes from the convection-corotation electric field

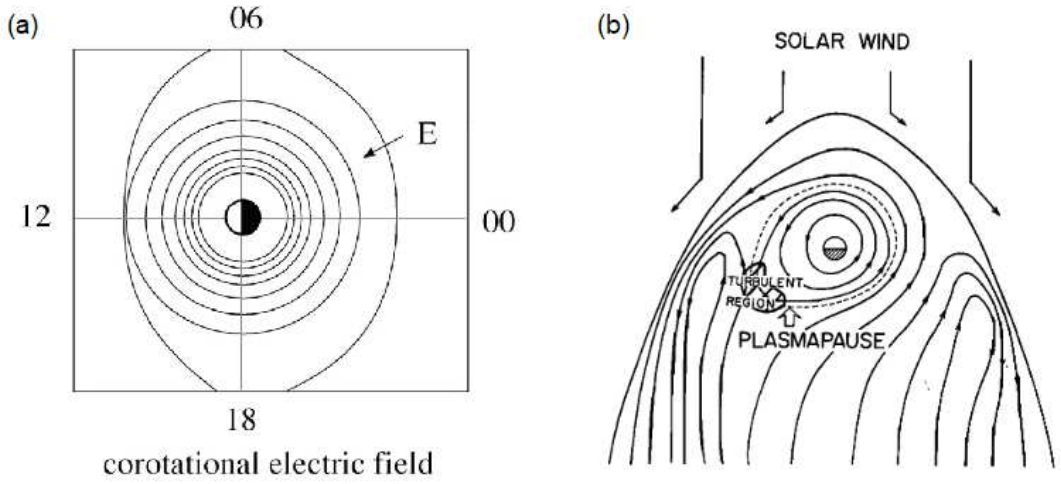

Figure 13: (**a**) Equipotential lines of the corotational electric field in the equatorial plane, with local times (Koskinen, 2011). (**b**) Plasma streamlines under the effects of convection and corotation electric fields. The edge of the plasmapause is also drawn (Nishida, 1966).

model, where the motion of cold plasma ($\mu = 0$) is guided on equipotential surfaces near the Earth. The corotation electric field rises from the fact that the plasma and the Earth's ionosphere rotate along with the Earth's rotation almost perpendicular to the magnetic field, and the plasma is thus affected by an electric field

$$\mathbf{E}_{rot} = -(\Omega \times \mathbf{r}) \times \mathbf{B}, \tag{3.7}$$

where $\Omega \times \mathbf{r}$ is the corotation velocity and Ω is the Earth's angular velocity. Equation (3.7) thus resembles Equation (2.2), with the solar wind velocity $\mathbf{v}_{sw}$ replaced with the corotation velocity. Figure 13a shows the direction and equipotential lines of the corotational electric field inside the magnetosphere. Figure 13b shows an illustration of the combination of the effects of the convection and corotation electric fields on the motion of plasma. One can see notable local time (LT) asymmetry in the closed streamlines; in the evening sector there is a bulge on the plasmasphere, and in the dawn sector the plasmasphere is compressed (tightly packed streamlines). The edge of the plasmapause is located at a usual distance of $4R_E$, which is the average distance where the corotation and magnetotail electric fields are equal (Nishida, 1966). This distance infers that the plasmapause overlaps with the ring current and the inner radiation belts, even though each of these regions contain plasma with very different energies and densities.

The plasmasphere contains cold ($\sim$ 1eV) and very dense ($10^2 - 10^4\,\mathrm{cm}^{-3}$) plasma (mainly protons and electrons). Essentially, it is an extension of the Earth's ionosphere, as the dayside ionosphere expands into space along the magnetic field lines, and creates a torus around Earth (Singh et al., 2011). The plasmasphere has an abrupt decrease of electron density, the plasmapause (Carpenter, 1963, 1966). The plasmasphere grows larger with prolonged low geomagnetic activity, when the ionospheric

source dominates. The plasmasphere can reach as far as $6-7R_E$ during such periods, and the plasmapause essentially fades into a soft edge. As the geomagnetic activity increases and the convection electric field plays a stronger effect, the plasmapause forms a sharper edge located closer to Earth, and the outer plasmasphere is lost into the magnetosphere (Singh et al., 2011).

3.2 Interaction with the solar wind

Historically, two theories were developed to explain the convection of the dayside magnetic field lines to the nightside, forming the stretched structure of the magnetotail. The first suggestion was a reconnection model of an open magnetosphere (Dungey, 1961). The other was a viscous interaction between the solar wind and a closed magnetosphere that forces some of the magnetospheric field lines to move from the dayside magnetosphere to the nightside, stretching them in the process (Axford & Hines, 1961). While the viscous interaction is partly responsible for the magnetotail structure, Dungey's reconnection model is the main model to explain the structure and dynamics of the magnetosphere. In addition, Dungey's model evidently justifies the larger dynamics of the magnetosphere (storms and substorms), as it is the model to describe the coupling between the IMF and magnetosphere. It describes how the energy from the solar wind transfers into the magnetosphere, forcing the magnetosphere to respond accordingly.

The main evidence which supports Dungey's theory, is that the dayside reconnection rate is more effective when the IMF southern component B_S (B_S is $B_z(B_z < 0)$ or $0(B_z > 0)$) is strong, i.e., the IMF is southward oriented (Burton et al., 1975; Kamide et al., 1977; Baker et al., 1983; Gonzales et al., 1994). When this happens, the IMF B_S component points antiparallel to the magnetospheric field lines, which enables reconnection to happen between the IMF and the magnetosphere in the magnetopause, and Dungey's cycle to start.

Figure 14 shows an illustration of Dungey's cycle (magnetospheric convection) in 9 steps. In the beginning, the IMF reconnects with the dayside magnetospheric field lines in the magnetopause (step 1). The opened field lines having their other end in the solar wind and other end in the Earth, start to convect to the nightside along with the solar wind flow (steps 2-5). In the tail, the growth of the magnetic flux increases the magnetic pressure in the tail lobes, which makes the inner magnetic field lines move closer to the cross-tail current. The field lines get so close together that reconnection happens in the middle of the tail (step 6). Immediately after the reconnection, the inner part of the field dipolarizes and experiences high magnetic tension due to its highly bent shape. The tension acts as a force and moves the field line closer to the Earth (step 7-8). Magnetic field lines travel back to the dayside, and the cycle restarts (step 9). The outer part of the reconnected field travels out of the magnetosphere along the solar wind flow (step 7').

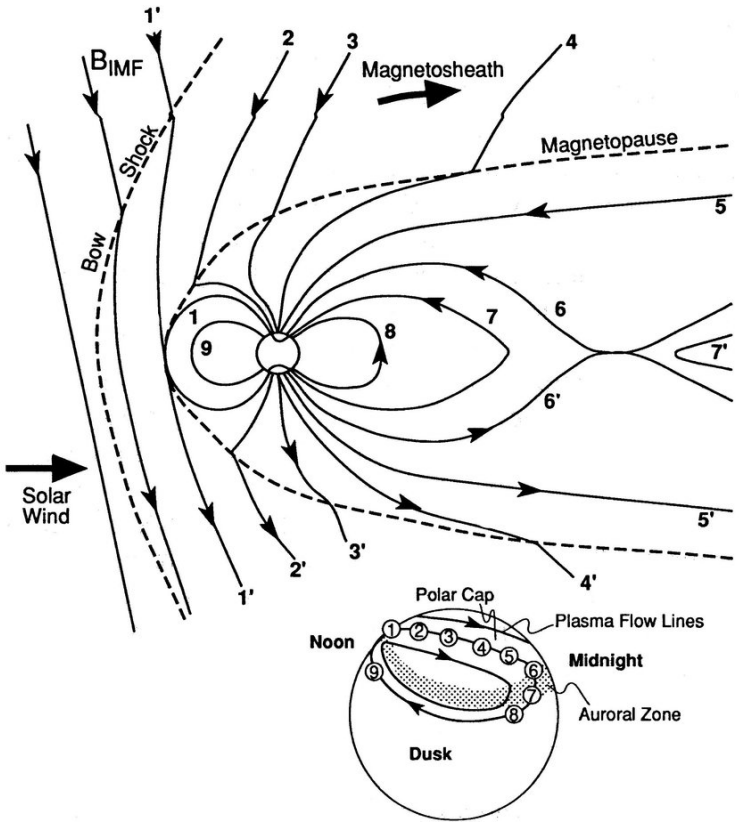

Figure 14: An illustration of the magnetospheric convection cycle in 9 steps (Hughes, 1995).

3.2.1 Coupling functions

Solar wind-magnetosphere coupling functions are combinations of solar wind parameters, formed analytically or empirically to examine how much each of the parameters contribute to the magnetospheric response (geomagnetic indices or other additional measurements) (Newell et al., 2007; Lockwood et al., 2019). The southern IMF component B_S and the solar wind speed v are the main drivers for the coupling between the solar wind and the magnetosphere. Their product vB_S, forms the first basic coupling function (Burton et al., 1975). The vB_S is equivalent to the convection electric field E_y according to Equation (2.2). In the magnetosphere, this eastward electric field strengthens the magnetotail currents via a generator effect between the solar wind and the magnetosphere (Stern, 1983), and increases the electric potential of the charges in the cross-tail current. Solar wind kinetic energy is transferred to electric power via a dynamo effect, as the the bent magnetic field lines (Figure 14, step 4) are affected by a sunward magnetic tension force opposing the convection in the tail lobes. Thus, kinetic energy is extracted by the magnetosphere.

Over the years, multiple more complex coupling functions have been developed also. They are usually being a variant of the ϵ power parameter ($\epsilon = vB^2 \sin(\frac{\theta}{2})$) (Perreault & Akasofu, 1978) or a function of the solar wind electric field (Kan & Lee,

1979). Here as an example, a "universal" coupling function is presented (Newell et al., 2007)

$$\Phi = v^{4/3} B_T^{2/3} \sin^{8/3} \frac{\theta}{2}, \tag{3.8}$$

which is the Newell coupling function, where Φ is the reconnection rate of magnetic flux in the dayside magnetopause, v is the solar wind speed, $B_T = \sqrt{B_z^2 + B_y^2}$ is the transverse component of the IMF and $\theta = \arctan(B_y/B_z)$ is the clock angle of the IMF. Like many coupling functions, Φ is nonlinear in v and B_T, which is why Φ does not have a physical unit, unlike vB_S (V/m), although it is designed to describe the rate magnetic flux is opened at the magnetopause.

3.2.2 Expanding/contracting polar cap

The boundary between open and closed magnetic field lines mark the boundary for the ionospheric polar cap (PC). As the dayside reconnection opens the Earth's dayside magnetic field lines, the volume of open flux in the magnetosphere increases, because the nightside reconnection rate adjusts itself only with a delay to match the dayside reconnection rate. So, once the open magnetic flux increases, the PC expands simultaneously, making the PC boundary to descend to lower latitudes. Respectively, as the open flux decreases via the nightside reconnection, the PC contracts (Siscoe & Huang, 1985). This way of thought is called the expanding/contracting polar cap (ECPC) paradigm (Cowley & Lockwood, 1992; Milan et al., 2007). The ECPC can be described quantitatively as a formulation of the Faraday's law

$$\frac{dF_{PC}(t)}{dt} = \Phi_D(t) - \Phi_N(t), \tag{3.9}$$

where F_{PC} is the total flux mapping into both of the northern and southern PCs, and Φ_D and Φ_N are the dayside and nightside reconnection rates. The reconnection rates are in units of Wb/s (or volts). Equation (3.9) states that if the dayside reconnection rate Φ_D is larger than the nightside reconnection rate Φ_N, the open flux F_{PC} mapping into the PCs increases, and if the Φ_N is larger, the F_{PC} decreases. The F_{PC} is defined as

$$F_{PC} = \int_{PC} \mathbf{B} \cdot d\mathbf{A}, \tag{3.10}$$

where the $\mathbf{B}$ is the Earth's dipole field in the PC area $d\mathbf{A}$. The area of the PC can be measured, if the PC boundary is known at all local times (Milan et al., 2003). However, the location of the PC boundary is not usually known exactly. The F_{PC} can also be estimated from direct measurements of the magnetic field and ion plasma parameters n and T_p in or near the plasma sheet, and estimating then the tail lobe radius as the area of the PC (Shukhtina et al., 2004). The amount of dayside reconnected magnetic flux, i.e., the dayside reconnection rate (in Wb/s) can be estimated as (Milan et al., 2007)

$$\Phi_D = L_{eff} v B_T \sin^4 \frac{1}{2}\theta, \tag{3.11}$$

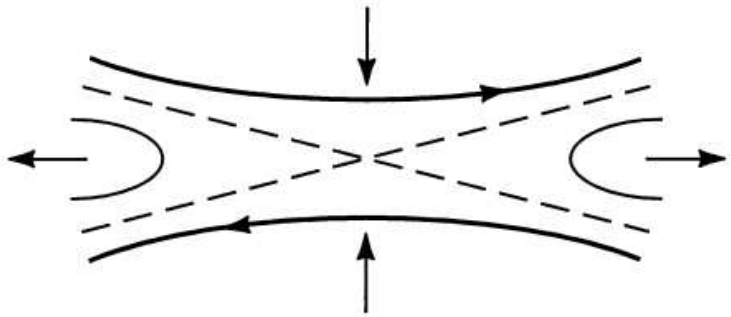

Figure 15: Plasma flows of forward and away from the X-point of the Sweet-Parker model of reconnection (Biskamp, 1996).

where the L_{eff} is the effective length of the dayside reconnection line. However, the dayside reconnection rate can be further approximated to

$$\Phi_D = \begin{cases} L_{eff} v |B_z|, & B_z < 0 \\ 0, & B_z > 0 \end{cases}, \tag{3.12}$$

due to the fact that the factor $\sin^4 \frac{1}{2}\theta = 0$ for $B_Z > 0$, i.e., dayside reconnection is close to zero for northward IMF.

3.2.3 Magnetic reconnection

Magnetic reconnection is an essential phenomenon in plasma physics, explaining the transfer of magnetic energy to kinetic and thermal energy of plasma. It can describe many transient phenomenona in space physics that require intense bursts of energy, e.g., solar flares, CMEs and magnetospheric substorms. Even though magnetic reconnection is long studied both by observations and simulations, the exact physics is still unknown. The reconnection models have problems in predicting the right rate of the reconnection process, usually predicting too slow reconnection. Some models predict fast enough reconnection, but have been proven false with observations and numerical simulations (Biskamp, 1996; Yamada et al., 2010).

The first theory for magnetic reconnection was the Sweet-Parker reconnection model (Sweet, 1958; Parker, 1963). The Sweet-Parker reconnection model produces a stable reconnection rate for ideal plasma, with a point of high magnetic diffusion. The magnetic diffusion is an MHD phenomenon, which is included in the magnetic induction equation.

$$\frac{\partial \mathbf{B}}{\partial t} = \nabla \times (\mathbf{v} \times \mathbf{B}) + \frac{1}{\mu_0 \sigma} \nabla^2 \mathbf{B}, \tag{3.13}$$

where the μ_0 is vacuum permeability and σ is the conductivity of the plasma. The first term on the right hand side describes magnetic convection, and the second term magnetic diffusion. According to Equation (3.13), finite conductivity σ results in the diffusion of the magnetic field over time. On the other hand for infinite σ (ideal

plasma), the magnetic field does not diffuse, but travels along the plasma with velocity **v**, and is thus frozen into the plasma.

In the Sweet-Parker model, two oppositely directed magnetic fields (two plasma regions) flow towards each other, while bending slightly, usually due to magnetic pressure. The bending results in an X-shape of the two magnetic fields, and an X-point is formed, where the low conductivity of the plasma diffuses the magnetic field to zero. In this magnetic null point, the plasma particles are reorganized so that the magnetic field seems like it has been cut and reconnected. The two new magnetic field lines are highly bent, so magnetic tension force accelerates them outward of the reconnection point. A simple illustration of the X-point and the inflows and outflows are seen in Figure 15. The idea behind the Sweet-Parker model has been found to be close to reality, however the problem lies in the diffusion rate in the X-point, which in reality is much faster than Equation (3.13) predicts. Also the exact plasma physics on a particle level is unknown, because the MHD theory approximates plasma as a fluid.

The second theory for reconnection was Petschek's slow-shock model (Petschek, 1964). Petschek's model uses slow MHD shocks that speed up the Sweet-Parker reconnection process via faster outflow of the plasma. A Sweet-Parker X-point is needed in both models. However Petschek's model eliminates the need for resistivity in the reconnection rate. Petschek's model was found erroneous for constant resistive MHD plasma (Yamada et al., 2010).

3.3 Magnetosphere-ionosphere coupling

Magnetospheric currents close with ionospheric currents via field-aligned currents (FAC), that flow along the magnetic field lines into and out of the ionosphere. From an ionospheric perspective, the FAC can be separated into region 1 (R1) and region 2 (R2) currents via closing points of these currents. Figure 16 shows an illustration of the basic idea of the FAC into and out of the ionosphere, as well as the plasma streamlines and electric fields in the ionosphere. The first mapping for the R1 and R2 currents was done by Iijima and Potemra (Iijima & Potemra, 1967), which showed that the R1 currents flow a little more poleward than the R2 currents, and the R1 and R2 currents flow in opposite directions (also seen in Figure 16).

The source for the R1 currents is formed by the magnetopause currents, powered by the generator effect between the solar wind and the magnetopause (Iijima & Potemra, 1982; Stern, 1983). Closed field lines can also hold R1 currents, one notable system generating such currents is the substorm current wedge (McPherron, 1972). The source for the R2 currents is the so called charge separation in the dusk and dawn sectors, as more electrons drift around the Earth through the dawn, and more ions through the dusk sector (also known as the Alfvén layers) (Ganushkina et al., 2015). R2 currents close with the R1 currents in the ionosphere through Pedersen currents, thus the R2 currents flow into the ionosphere in the dusk sector, and out of the ionosphere via the dusk sector R1 currents, and vice versa in the dawn sector. However the R1 and R2

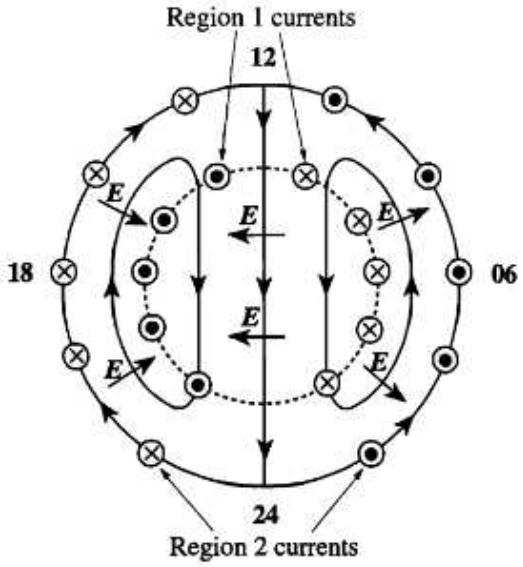

Figure 16: Illustration of region 1 and 2 FAC connection to the ionosphere, as well as the plasma streamlines due to magnetospheric convection. Arrowed solid lines show the streamlines, and the short arrows show the electric fields in the ionosphere (Cowley, 2000).

are not equal in intensity, because the incoming R1 current mainly closes through the polar cap to the outgoing R1 current. In the magnetosphere, the Alfvén layers are closed via the so called partial ring current that flows through the night sector from dawn to dusk.

3.3.1 Field-aligned currents

The physical basis for the FAC in the magnetosphere comes from the fact that space plasma is neutral and continuous, and thus does not generate currents itself. In mathematical terms

$$\nabla \cdot \mathbf{J} = 0, \tag{3.14}$$

which is the equation for current continuity and states that the currents are closed and sourceless. Furthermore, one can separate the currents to parallel and perpendicular components with the magnetic fields, thus

$$\nabla \cdot (\mathbf{J}_\parallel + \mathbf{J}_\perp) = 0 \quad \Rightarrow \quad \nabla \cdot \mathbf{J}_\parallel = -\nabla \cdot \mathbf{J}_\perp, \tag{3.15}$$

which means that since the source for the field-aligned current is the negative divergence of the perpendicular currents, a perpendicular current leads to a field-aligned current and vice versa.

Another immediate implication for the FAC comes from Equation (3.3), which in the case of tenuous or homogeneous plasma $\nabla p \approx 0$ is

$$\mathbf{J} \times \mathbf{B} \approx 0, \tag{3.16}$$

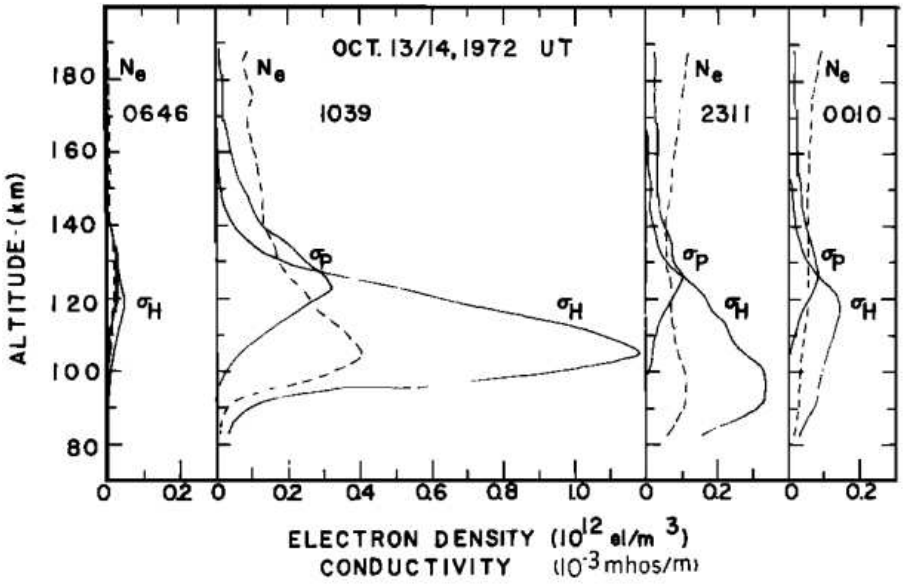

Figure 17: An example of electron density and Hall and Pedersen conductivity profiles for four different UT intervals; quiet evening time (0646 UT), disturbed nighttime (1039 UT), disturbed daytime (2311 UT) and quiet daytime (0010 UT). Measurements were made by an incoherent scatter radar (Brekke et al., 1974).

so the **J** flows parallel to the magnetic field. In the case for such currents, the magnetic field **B** is a combination of the background magnetic field and the magnetic field produced by the current **J**. In result, the **B** resembles a spiral, i.e., a magnetic flux robe, a force-free magnetic field following Equation (2.1).

3.3.2 Auroral electrojets

Ionospheric electrons and ions are affected by the horizontal $\mathbf{E} \times \mathbf{B}$ drift, with velocity

$$\mathbf{v}_d = \frac{\mathbf{E} \times \mathbf{B}}{B^2}. \tag{3.17}$$

This drift results to two types of currents in the ionospheric E region, as the $\mathbf{E} \times \mathbf{B}$ drift is disrupted by the ion-neutral and electron-neutral collisions. As the altitude decreases, the density of neutral atoms increases and ion mobility decreases. Ion and electron mobilities are described by the collision frequencies ν_{in} and ν_{en} affecting the gyrofrequencies ω_i and ω_e. With increasing density of neutrals, charged particles gyrate less and less after each collision. This depletion of gyration results to ions moving (still slightly gyrating) along the electric field **E** (electrons along $-\mathbf{E}$), thus carrying the so called Pedersen current, which flows along the electric field **E** and perpendicular to the magnetic field **B**. Pedersen currents are mainly carried by ions, while electrons drift more freely in the $\mathbf{E} \times \mathbf{B}$ direction. At lower altitudes (110 km) the ion-neutral collision frequency ν_{in} increases further, so the Hall electron mobility becomes greater than the Hall ion mobility. Both ions and electrons drift in the $\mathbf{E} \times \mathbf{B}$ direction, while

ions lag behind, creating a current carried mainly by electrons, opposite to the drift direction ($-\mathbf{E}\times\mathbf{B}$). Thus Hall currents are directed perpendicular to both the electric field and the magnetic field (opposite to the plasma streamlines in Figure 16). Hall currents also carry the westward and eastward electrojets, and they produce the main magnetic disturbances detected on Earth at auroral latitudes. The eastward electrojet flows from afternoon to midnight and the westward electrojet flows from dawn to midnight (Ganushkina et al., 2015).

Pedersen and Hall ion and electron mobilities are defined as

$$k_{iP} = \frac{1}{eB}\frac{\omega_i\nu_{in}}{\omega_i^2+\nu_{in}^2} \tag{3.18}$$

$$k_{iH} = \frac{1}{eB}\frac{\omega_i^2}{\omega_i^2+\nu_{in}^2} \tag{3.19}$$

$$k_{eP} = \frac{1}{eB}\frac{\omega_e\nu_{en}}{\omega_e^2+\nu_{en}^2} \tag{3.20}$$

$$k_{eH} = -\frac{1}{eB}\frac{\omega_e^2}{\omega_e^2+\nu_{en}^2}, \tag{3.21}$$

and produce the Pedersen and Hall conductivities defined as

$$\sigma_P = \frac{n_e e}{B}\left(\frac{\omega_i\nu_{in}}{\omega_i^2+\nu_{in}^2}+\frac{\omega_e\nu_{en}}{\omega_e^2+\nu_{en}^2}\right) \tag{3.22}$$

$$\sigma_H = \frac{n_e e}{B}\left(-\frac{\omega_i^2}{\omega_i^2+\nu_{in}^2}+\frac{\omega_e^2}{\omega_e^2+\nu_{en}^2}\right). \tag{3.23}$$

The general equation for the horizontal currents in the ionosphere can be derived from the generalized Ohm's law

$$\mathbf{J}_\perp = \sigma_P\mathbf{E} - \sigma_H\frac{\mathbf{E}\times\mathbf{B}}{B}. \tag{3.24}$$

Figure 17 shows an example of the Pedersen and Hall conductivity profiles. One can see that the σ_H tends to be larger than the σ_P in general, and the σ_H peaks slightly lower in altitude ($\sim 110\,\mathrm{km}$) than σ_P ($\sim 125\,\mathrm{km}$). The conductivities increase during the day due to photoionization by solar illumination, which is the main reason for the conductivity of the ionosphere; photoionization frees more electrons to the currents. Solar illumination has seasonal difference, since the available daylight differs between the two hemispheres. This creates seasonal variations to the conductivity profiles.

An important feature can be seen during the disturbed nighttime in Figure 17, as the σ_H increases greatly. This is explained by the fact that the precipitation of charged particles increases the electron density. Because energetic particles tend to ionize the E region below the altitude of 125 km, more electrons are freed to the Hall currents, resulting to ionization in the lower altitudes as seen in Figure 17 (third UT interval). Due to this, the electrojets, especially the westward electrojet, is enhanced during particle precipitation.

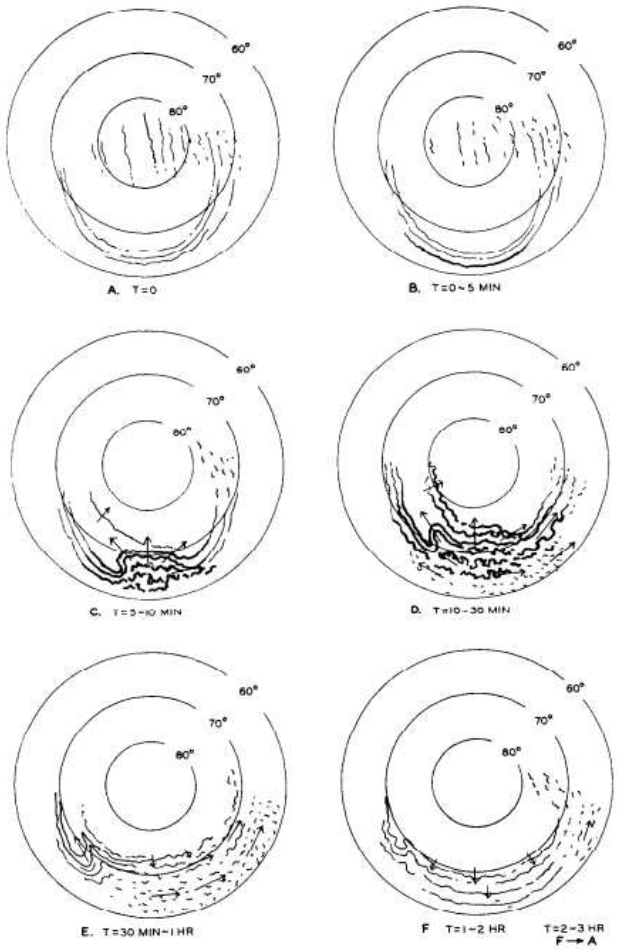

Figure 18: A schematic diagram of the development of the growth, expansion and recovery phases of an auroral substorm. The center is the geomagnetic north pole, the Sun is at the top of each circle (Akasofu, 1964).

4 Substorms

Substorms are a key part of the dynamics of the magnetosphere. As a phenomenon, it explains how the configuration of the magnetosphere is forced to change under the effect of increased energy input by the solar wind, i.e., as magnetic energy from the solar wind is stored into the magnetotail by enhanced dayside reconnection (southward turning of the IMF), and released explosively into the ionosphere via FAC. Substorms also play a role in magnetospheric convection (Figure 14) (Milan et al., 2008), but while the magnetospheric convection is a steady feature of the magnetosphere with balanced dayside and nightside reconnection rates, the substorms are more energetic and violent, with distinct features (McPherron, 1972, 1979).

Substorms affect three near-Earth space features: magnetospheric configuration, ionospheric currents (via FAC) and auroral emissions. Due to the latter feature, substorms are historically called auroral substorms due to distinct morphological changes in the aurorae associated with substorms (Akasofu, 1964). Later the substorms were

found to be a more global phenomenon in the magnetosphere, thus named magnetospheric substorms (McPherron, 1970).

Substorms include three distinct phases: the growth phase ($\sim 1\,\mathrm{h}$), the expansion phase ($\sim 30\,\mathrm{min}$) and the recovery phase ($\sim 1-2\,\mathrm{h}$) (Rostoker et al., 1980). Each of these phases are evident in morphological changes of aurorae that stem from the temporal and topological changes of the magnetic field lines, which lead into diversion of the currents in the nightside magnetosphere and energetic particle precipitation. During the growth phase, the strengthened southward IMF component increases the dayside reconnection, enhancing the convection of the magnetic field lines to the nightside. The auroral oval (polar cap) expands to lower latitudes (Milan et al., 2007), strengthening the FAC (Coxon et al., 2014). As the polar cap expands, the Pedersen and Hall currents also move to lower latitudes. Referring to the ECPC model, during the growth phase, Equation (3.9) has a negligible nightside reconnection rate.

At the expansion phase (substorm onset), a reconnection happens in the middle of the magnetotail, leading to an explosive release of energy into the ionosphere. The reconnected field lines dipolarize as magnetic flux flow earthward from the reconnection site (flow burst), while disrupting and diverting the magnetotail cross-tail current to the ionosphere via FAC. During the expansion phase, the nightside reconnection rate dominates, resulting to a decreasing of the polar cap open flux and contracting of the polar cap area. After the expansion phase, the currents start to decay as an indication of the recovery phase. At the recovery phase, the magnetic field lines convect back to the dayside and the substorm subsides. The magnetosphere goes back to its quiet time configuration, and another substorm may begin to grow. Multiple onsets are possible, when the energy input of the solar wind is continuous. Then, the first substorm may show signatures of the growth phase, but the subsequent substorm goes straight to the expansion phase.

Figure 18 shows the original diagram of the expansion and recovery phases of an auroral substorm (Akasofu, 1964). The growth phase is inherently included in Figure 18, although not yet recognized as an essential phase of the substorm in 1964 (e.g., McPherron, 1972). As stated in Figure 18, the auroral substorm has a life time of 1-3 hours. Steps A and B depict the beginning of the growth phase, as the most equatorward part of the quiet-time auroral arc brightens and moves slowly southward. Step C shows the subsequent brightening and rapid westward, poleward and eastward expanding of the auroral arc (substorm onset), forming the so called auroral bulge around the midnight sector. In step D, westward propagating auroral folds start to appear in the evening sector, as the bulge keeps expanding. These propagating folds form the bright westward traveling surge (WTS). Steps E and F depict the recovery phase. After the poleward edge of the auroral bulge reaches its highest latitude, the expansion stops and the poleward edge starts to descend southward, and the bulge diminishes. The WTS weakens, and may reduce to small independent auroral folds that travel a short distance in the middle of the evening sector before disappearing.

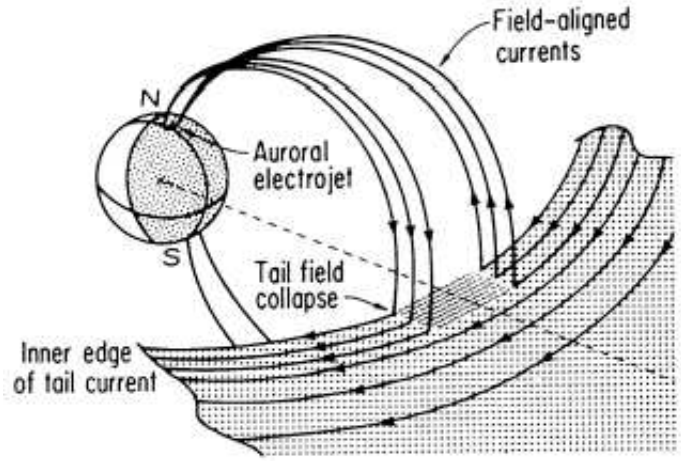

Figure 19: A sketch of the substorm current wedge (McPherron et al., 1973).

4.1 Substorm current wedge

The substorm current wedge (SCW) is a wedge-like current structure that forms in the nightside of the Earth due to the nightside reconnection in the tail and velocity shear associated with the dipolarization of the magnetic field lines at the expansion phase. Unlike the name suggests, the SCW can also be formed during smaller scale magnetospheric disturbance, but is most dramatic during substorms. Figure 19 shows the original line model for the SCW, where the dipolarization diverts the magnetotail current to the ionosphere via strong FACs. The FACs flow into the ionosphere in the east and out in the west, thus resembling R1 currents. In fact, the R1-type SCW FACs flow roughly at the same latitudes as the regular R1, however, unlike the regular R1 currents, the SCW closes via the westward electrojet, while enhancing it greatly, creating magnetic disturbances at auroral latitudes. Meridional "local current closure" also exists in the ionosphere, which affects the currents at auroral latitudes (Kepko et al., 2015).

The SCW is the magnetospheric cause to the auroral substorm. Thus, the WTS is actually an auroral display of the western edge of the enhanced westward electrojet, i.e., the upward current of the SCW. The upward currents are associated with electron precipitation, increasing the conductivity of the ionosphere and brightening the aurorae. However in reality, Figure 19 is oversimplified. Weaker R2-type currents also flow in the SCW, and the current system actually has a complicated substructure due to the varying conductivity of the ionosphere. Still, the line model can be thought of as the net effect of all the combined substructures, and so it forms the basis for the understanding of the magnetic signatures seen on the ground and in nightside sector.

The SCW can be modeled with MHD equations via simulations, which increases the theoretical knowledge in understanding the measurements. The models follow the continuity equation (3.15), so that the parallel current can be calculated from the diversion of the perpendicular current. From the momentum equation, the $\mathbf{J}_\perp$ in

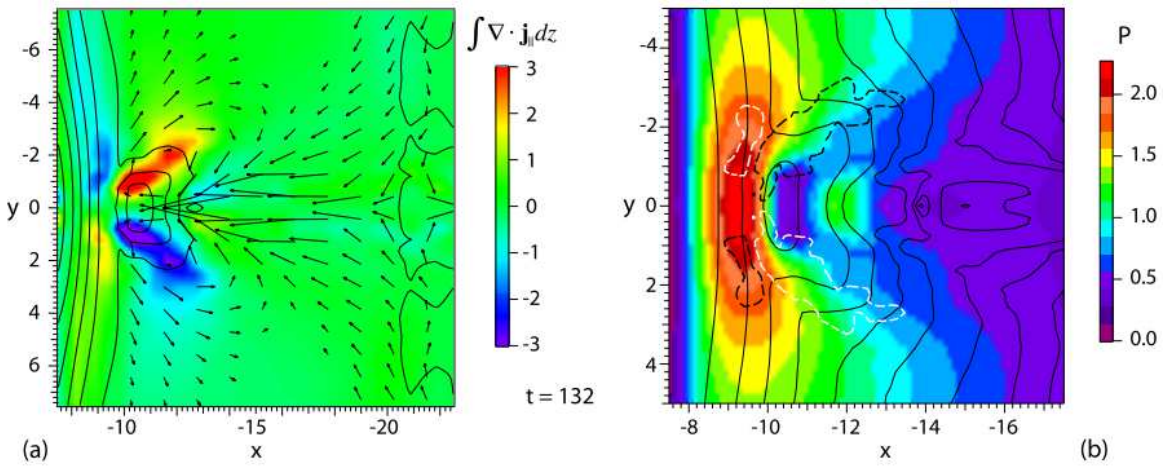

Figure 20: (**a**) Diversion of perpendicular into parallel currents, based on an MHD simulation of near-tail reconnection and earthward flow. Color shows the magnitude of the $\nabla \cdot \mathbf{J}_{\parallel}$ in $z = 0$, integrated over z. Arrows show velocity vectors and the solid lines are contours of constant B_z. (**b**) FAC sources from Vasyliunas' equation (4.4) for the state from (**a**). Color shows the plasma pressure in $z = 0$. Solid black lines are contours of constant flux tube volume, and dashed black and white contours are outlines for the regions of enhanced non-aligned pressure and flux tube volume gradients $|\nabla P \times \nabla \int \frac{ds}{B}|$ (Kepko et al., 2015; Birn et al., 2011).

Equation (3.15) becomes (Kepko et al., 2015)

$$\nabla \cdot \mathbf{J}_{\parallel} = -\nabla \cdot \left(\frac{\mathbf{B}}{B^2} \times \rho \frac{d\mathbf{V}}{dt} + \frac{\mathbf{B}}{B^2} \times \nabla p \right), \tag{4.1}$$

where ρ is the plasma density and $\mathbf{V}$ is the velocity. This results into an integral

$$J_{\parallel} = -\frac{B_i}{2} \int \nabla \cdot \left(\frac{\mathbf{B}}{B^2} \times \rho \frac{d\mathbf{V}}{dt} + \frac{\mathbf{B}}{B^2} \times \nabla p \right) \frac{ds}{B}, \tag{4.2}$$

where the B_i is the field at the ionospheric end of the flux tube, ds is the element of the magnetic field line, and the integral is taken along the field between two ionospheric ends of the flux tube. The first term on the right hand side is called the inertial current, which exists during (positive or negative) acceleration of the magnetic field lines, i.e., during the dipolarizing flows of the magnetic field lines. This term is known to play a smaller (on short timescales) role, so it can be approximated to zero, which reduces the $\mathbf{J}_{\perp}$ into a current in a magnetohydrostatic balance from Equation (3.2), and the integral becomes

$$J_{\parallel} = -\frac{B_i}{2} \int \nabla \cdot \left(\frac{\mathbf{B}}{B^2} \times \nabla p \right) \frac{ds}{B}, \tag{4.3}$$

which can be expressed as (Vasyliunas, 1970)

$$J_{\parallel} = -\frac{B_i}{2}\frac{\mathbf{B}}{B^2} \cdot \left(\nabla p \times \nabla \int \frac{ds}{B}\right), \tag{4.4}$$

where the $\int \frac{ds}{B}$ is the volume of the flux tube of unit magnetic flux. This form shows that the (R1-type) FAC are formed from an earthward directed pressure gradient and azimuthally directed gradient of flux tube volume.

The inertial current term of Equation (4.2) plays an additional role in the formation of the FAC, with the curl of the velocity. The curl of the velocity is plasma vorticity

$$\mathbf{\Omega} = \nabla \times \mathbf{V}, \tag{4.5}$$

with which the inertial current term 4.2 results into (Keiling et al., 2009)

$$J_{\parallel} = -\frac{B_i}{2}\int \frac{\rho \mathbf{B}}{B^3} \cdot \frac{\mathrm{d}\mathbf{\Omega}}{\mathrm{d}t} ds, \tag{4.6}$$

which shows that the temporal changes of plasma vortices play a part in forming the FAC.

Figure 20a shows the result of the direct integration of $\nabla \cdot \mathbf{J}_{\parallel}$, which reveals the basic structure of the SCW. Plasma flow vectors show that closer to Earth (10-11R_E), the flow diverts azimuthally outwards, resulting into two oppositely directed plasma vortices. In the middle of these vortices, (R1-type) FACs are seen to flow upwards (earthward) in the clockwise vortex, and downwards (from the Earth into magnetosphere) in the counterclockwise vortex (Keiling et al., 2009; Yao et al., 2012). Figure 20b shows a similar current structure attained from Equation (4.4). The areas showing enhanced $|\nabla P \times \nabla \int \frac{ds}{B}|$ (dashed contours), clearly indicate the formation of R1-type FAC, as the pressure increases earthwards, and flux tube volume decreases azimuthally outwards. Similarly, R2-type currents are formed closer to Earth, due to the pressure increasing towards midnight, and flux tube volume increasing radially outwards. The increased pressure in Figure 20b shown in red, is due to the earthward flow from the reconnection site, bringing compressed plasma to near-Earth space in front of it. The decreasing of flux tube volumes is also due to the reconnection, as magnetic flux flows to near-Earth region. The earthward flows are thus critical drivers in the formation of the SCW.

4.2 Substorm models

One of the great tasks in the research of substorms is to form a comprehensive model to explain all substorm phases and their appearance in the magnetosphere. Several models have been proposed to explain features and phases of substorms, mostly the expansion phase (Lui, 1991). The most comprehensive model remains the near-Earth neutral line model (NENL) (Baker et al., 1996). The NENL explains the whole substorm process via three reconnection points, shown in Figure 21. The N1 reconnection

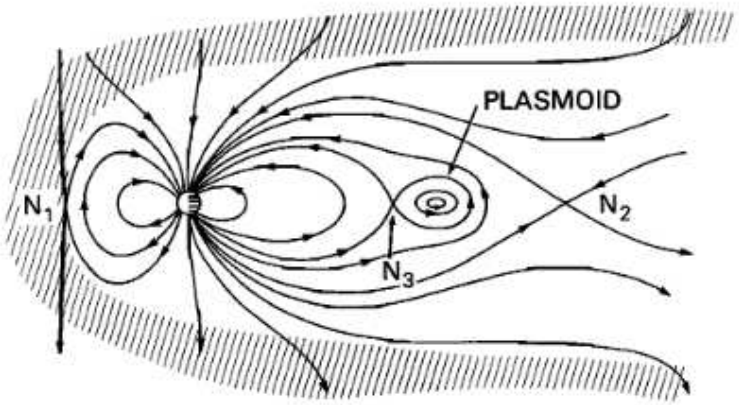

Figure 21: Schematic view of the formation of a near-Earth neutral line (NENL) and a plasmoid (Stern, 1989).

point marks the dayside reconnection with the IMF and the N2 the distant neutral point (e.g., present in magnetospheric convection). During the substorm growth phase as the dayside and nightside reconnection rates between these two points become unbalanced, a large amount of magnetic flux starts to accumulate in the tail, increasing the magnetic energy (pressure) in the tail lobes and thinning the plasma sheet, eventually forming the near-Earth neutral point N3 (at $\sim$ 20-30R_E). The reconnection points N2 and N3 form the so called plasmoid in the magnetotail, which is essentially a magnetic bubble flowing tailward, out of the magnetosphere. The reconnected magnetic field closer to Earth dipolarizes and drives the formation of the SCW as described in Section 4.1.

The plasmoid has particular research interests due to the associated fast tailward flow and closed magnetic field structure. This magnetic field creates signatures in the magnetic measurements further in the tail (beyond $20R_E$) as the plasmoid flows tailward. Simultaneous, closely located regions of southward field (plasmoid) and northward field associated with the earthward flows of the dipolarized field, are considered evidence for the NENL model and magnetic reconnection (Nagai et al., 1998).

Even though supported by a large body of empirical with the evidence, the NENL model is not perfect. The main problem lies at the triggering and time evolution of the substorm onset and the subsequent formation of the SCW. As stated in Section 4.1, plasma flows from the reconnection point could drive the formation of the SCW. However, the observed auroral signatures somewhat disagree with this theory. The brightening of aurorae start slightly equatorward of the polar cap (at the equatorward edge of the auroral oval), implying that the very first brightening stems from closed dipole-like magnetic field lines at $\sim 10R_E$. The aurorae take 5-10 min to expand poleward to the region, where they would map to the near reconnection point at $\sim 20R_E$. Thus dipole-like magnetic field configuration seems to exist before the magnetotail driving.

One model to explain this is called the current disruption (CD) model (Lui, 1996).

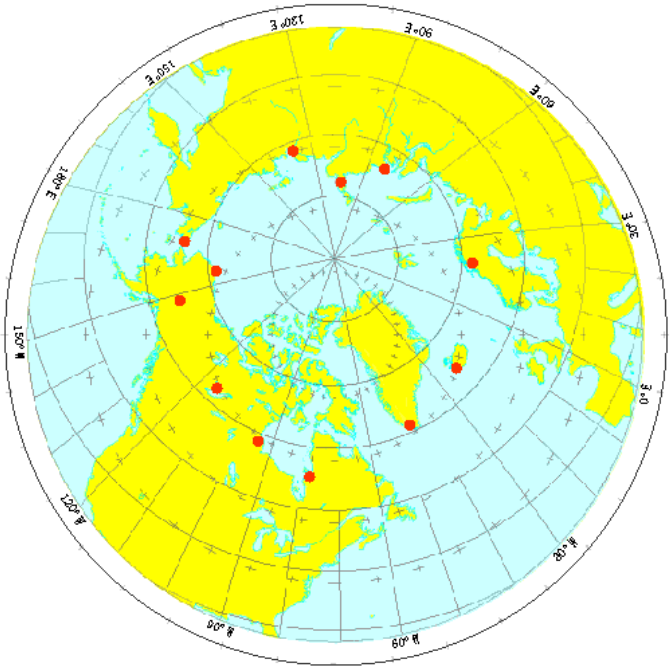

Figure 22: Distribution of the 12 *AE* stations (`https://wdc.kugi.kyoto-u.ac.jp/aedir/ae2/AEObs.html`).

According to the CD model, the SCW forms due to plasma instabilites leading into spontaneous disruption of the tail current (without reconnection), diverting the current into the ionosphere via FAC, forming the SCW. CD has the spatial domain at about $10R_E$, thus agreeing with the auroral observations. Both models have merit and can coexist. However, current evidence suggests that reconnection triggers the substorm onset (Angelopoulos et al., 2008), and the local instabilities in the tail current may follow as a consequence (Sergeev et al., 2012) from the BBFs. Also it may be possible that the highly dynamic magnetosphere has many ways to unload the energy from the solar wind.

4.3 Substorm indices

In general, geomagnetic indices are created and used to acquire quantitative measures from ground-based geomagnetic data. They form very comprehensive data sets with good temporal (and spatial) coverage. Since placing magnetometers on ground is relatively easy compared to sending spacecrafts into orbit, indices are effective tools in the research of the magnetosphere and space physics (Rostoker, 1972).

The largest short-term variations seen in geomagnetic data are due to the two current systems most affected by the energy unloadings in the magnetosphere: the auroral electrojets and the ring current. The ring current creates a sudden global depression of the Earth's magnetic field during geomagnetic storms, measured at low latitudes, while the auroral electrojets create distinct negative (westward electrojet)

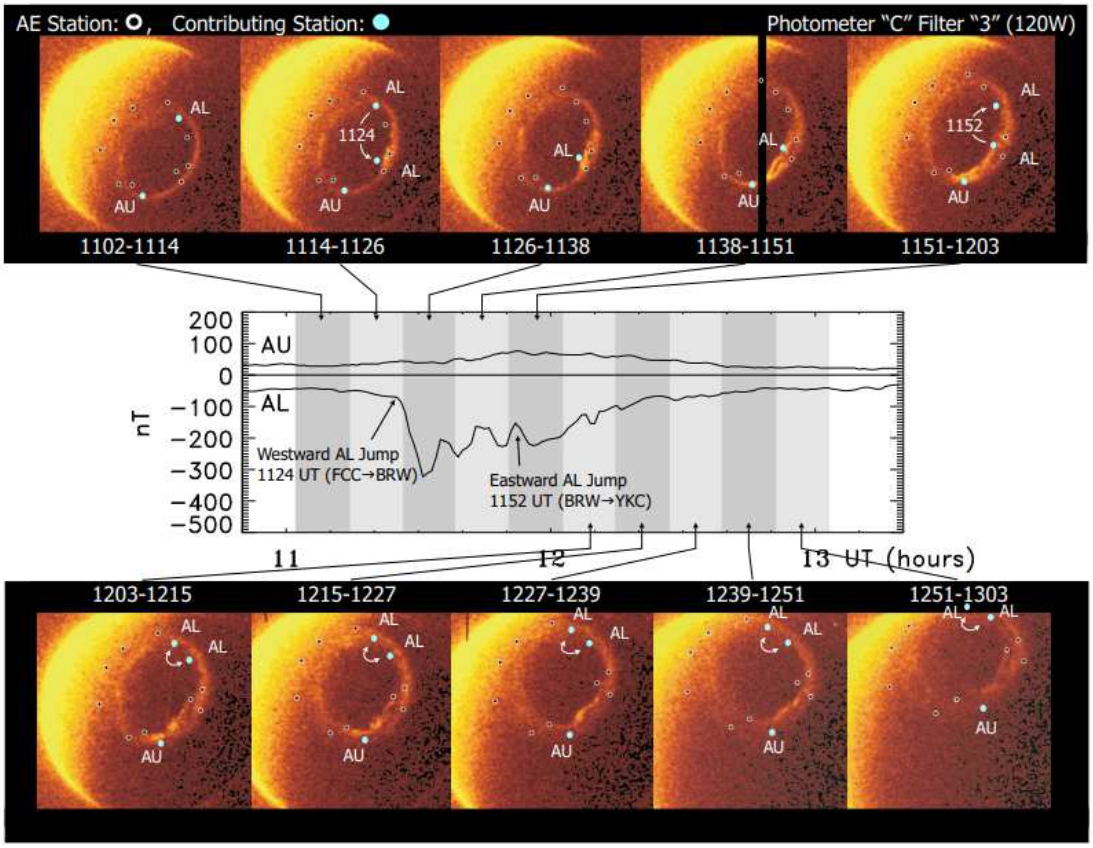

Figure 23: Global auroral images of a classic bulge-type auroral substorm and auroral indices AU and AL from 9 November 1981. Superposed onto images are the 12 AE stations. Single arrows indicate that during the 12-min exposure the contributing station changed from one station to another, while double arrows indicate that the two stations were alternating (Gjerloev et al., 2004).

and positive (eastward electrojet) disturbances at auroral latitudes. Certain indices can be created to measure the (maximum) effect of electrojets to the geomagnetic field at auroral latitudes, as measure of the amplitude of the current. As electrojets, especially the westward electrojet, are known to enhance during substorms, these type of indices are used to describe the electrojet behavior during a substorm. It is good to note that the indices that are created to describe a certain current system (e.g., the *AE* and *Dst* indices) cannot include or describe the effects of all other existing current systems. Thus, these indices take only a partial account of disturbances of all currents, but try to take a complete account of the current it tries to measure.

4.3.1 *AE* indices

The original index measuring the electrojet amplitude is called the auroral electrojet (*AE*) index (Davis & Sugiura, 1966). It is formed from superposed geomagnetic data from 10-13 stations, each at auroral latitudes, globally distributed in longitude as

shown in Figure 22. The data resolution has varied over the years, but a 1-min resolution is the most common. The measured magnetic components of the magnetic field for each station are in a geographic cartesian X (north), Y (east), Z (down) coordinate system. The horizontal H component is calculated as

$$H = \sqrt{X^2 + Y^2}, \tag{4.7}$$

of which the disturbances are then determined. To normalize the disturbances, a base value for each station needs to be determined. This base value marks the quiet time value for the magnetic field (baseline), of which the absolute disturbance is then calculated by subtracting the base value from the measured H-component at every time step. The baselines in the formation of the standard AE index are determined with the so called international quietest days, which are certain days, when the geomagnetic activity is known to be minimal. The five quietest days are selected monthly, and the average of the field during these five days is then selected as the base value for each of the stations. The monthly (or more frequent) update of the baseline is necessary, due to the seasonal variation of the geomagnetic field. The baseline selection can be questioned, since no exactly correct method exists. The results can be affected even by rather small modifications, so the research should be done understanding that the results are bound to the baseline selection (e.g., Gjerloev, 2012).

After the baseline subtraction, the AE index is defined as

$$AE = AU - AL, \tag{4.8}$$

where the AU is the largest measured H component (highest positive amplitude), and the AL is the smallest H component (largest negative amplitude). Every time step, the one station measuring the largest value contributes to the AU index and the one station measuring the smallest value contributes to the AL index. AU and AL are physical indices, as the AL index describes the westward electrojet (substorms) and the AU index the eastward electrojet. The AE index is the total effect of the electrojets. Figure 23 shows the 12 AE stations under auroral oval during a classic bulge-type substorm, as well as the magnetic signatures seen in the AU and AL indices. The AL index is affected more by the substorm acitivity, as the westward electrojet enhances. Also, the arrows in Figure 23 show that the change of stations contributing to the AL index can be large in distance. Figure 23 also shows the weakness of the AL index. The auroral oval can descent to lower latitudes than the stations, due to the narrow latitudinal distribution. In situations like this, the amplitude of the AL index does not correctly describe the intensity of the westward electrojet, since the electrojet might be most enhanced at the lower latitudes.

4.3.2 *IL* index

The AE indices form the primary data in the research of substorms via ground-based measurements. Similar indices can be formed using any magnetometer network, e.g.,

Station (IAGA code)	Geogr. lat (°)	Geogr. lon (°)	Start date	Overall NaN %
Ny Ålesund* (NAL)	78.92	11.95	1993-10-01	5.0%
Longyearbyen (LYR)	78.80	15.82	1993-10-01	7.1%
Hornsund (HOR)	77.00	15.60	1993-10-01	1.8%
Hopen Island (HOP)	76.51	25.01	1993-10-01	19.3%
Bear Island* (BJN)	74.50	19.20	1993-10-01	4.7%
Nordkapp (NOR)	71.09	25.79	2007-10-01	9.9%
Sørøya (SOR)	70.54	22.22	1982-10-01	7.8%
Kevo* (KEV)	69.76	27.01	1982-10-01	4.5%
Tromsø* (TRO)	69.66	18.94	1993-10-01	0.4%
Masi (MAS)	69.46	23.70	1991-09-01	15.0%
Andenes (AND)	69.30	16.03	1996-01-01	5.5%
Kilpisjärvi (KIL)	69.06	20.77	1983-06-01	5.6%
Ivalo (IVA)	68.56	27.29	2001-02-01	4.7%
Abisko (ABK)	68.35	18.82	1998-01-01	0.4%
Muonio (MUO)	68.02	23.53	1982-10-01	11.0%
Lovozero (LOZ)	67.97	35.08	1996-01-01	13.0%
Kiruna* (KIR)	67.84	20.42	1996-01-01	3.9%
Røst (RST)	67.52	12.09	2017-05-01	1.5%
Sodankylä* (SOD)	67.37	26.63	1996-01-01	1.2%
Pello* (PEL)	66.90	24.08	1982-10-01	6.5%
Jäckvik (JCK)	66.40	16.98	2010-09-01	7.2%
Dønna (DON)	66.11	12.50	2007-11-01	7.6%
Ranua (RAN)	65.90	26.41	2014-10-01	6.4%
Rørvik (RVK)	64.94	10.98	1999-09-01	4.6%
Lycksele (LYC)	64.61	18.75	1998-07-01	29.0%
Oulujärvi* (OUJ)	64.52	27.23	1992-11-01	4.4%
Mekrijärvi (MEK)	62.77	30.97	2004-10-01	6.4%
Hankasalmi* (HAN)	62.25	26.60	1992-08-01	7.5%
Dombås (DOB)	62.07	9.11	2000-01-01	1.4%
Solund (SOL)	61.08	4.84	2007-03-01	4.0%
Nurmijärvi* (NUR)	60.50	24.65	1992-01-01	0.4%
Harestua (HAR)	60.21	10.71	2018-01-01	1.5%
Uppsala (UPS)	59.90	17.35	1998-01-01	0.4%
Karmøy (KAR)	59.21	5.24	2004-01-01	2.1%
Tartu* (TAR)	58.26	26.46	2001-09-01	4.0%
Birzai (BRZ)	56.17	24.86	2015-01-01	1.7%
Hel (HLP)	54.61	18.82	2018-01-01	0%
Wingst (WNG)	53.74	9.07	2015-01-01	2.3%
Niemegk (NGK)	52.07	12.68	2015-01-01	1.4%
Polesie (PPN)	51.45	23.13	2018-01-01	0.01%

Table 1: Geographical coordinates and start dates of the IMAGE stations. Asterisks mark the subset of stations. The percents of missing data (NaNs) are also listed to mark the percentage of data gaps (`https://space.fmi.fi/image/www/index.php?page=stations`).

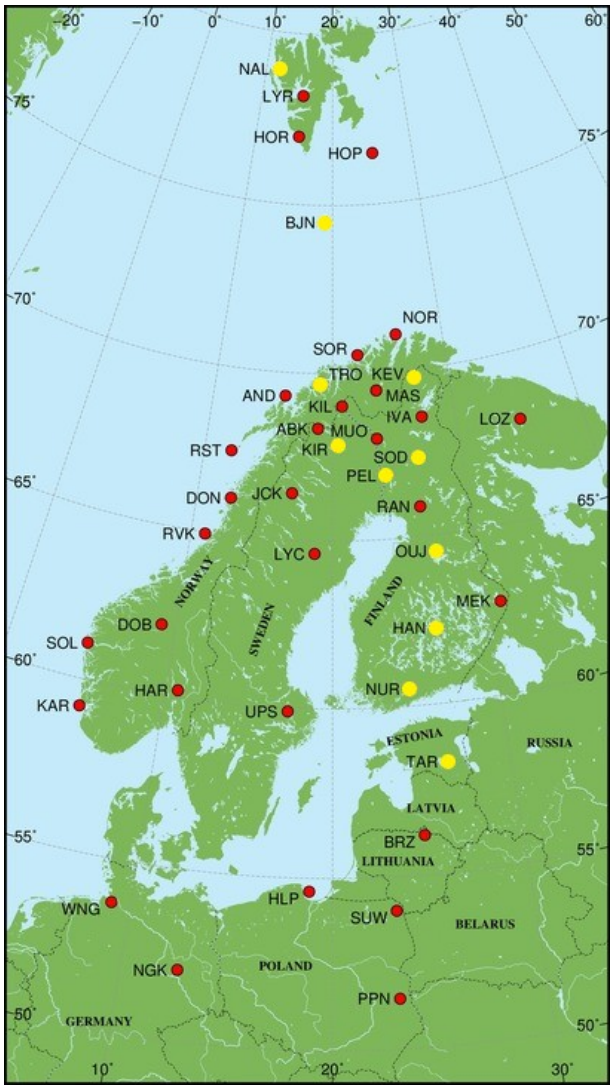

Figure 24: Map of the IMAGE magnetometer network (stations with red and yellow dots). The eleven stations with yellow dots mark the subset of stations (see also Table 1) selected for the study of latitudinal distribution of substorms (`https://space.fmi.fi/image/www/index.php?page=maps`).

the SML (Newell & Gjerloev, 2011) index and the IL index (Tanskanen, 2009). The SML index is the product of the SuperMAG collaboration (Gjerloev, 2009), which is a global collaboration of multiple magnetometer networks. The IL index uses the IMAGE magnetometer network. The IL index is used in this thesis extensively. The 40 IMAGE stations used in this thesis to form the IL index, are listed in Table 1 and shown on a map in Figure 24.

The derivation of the IL index follows that of the AL index: every minute, the smallest H component measured by any station of the IMAGE network determines the IL index. A notable difference, other than the different magnetometer network, is the selection of the baseline. In the original IL index, the baseline of each station

is selected daily, from the visually most quiet 15 to 60 min period. In this thesis, the baseline is calculated daily for each station by detecting the most quiet 21-03 local time (LT) interval (night) in a sliding 11-night window (±5 nights). The activity level of the nightly 21-03 LT interval is evaluated locally at each station as an average of absolute differences of (6∗60) successive minute values of the H component. The night with the smallest activity level in the 11-night window is then chosen as the most quiet, and the (6 h) average value of the H component of the most quiet night is the daily baseline for the whole day. The night interval (21-03) of the day is determined to be the following night. The daily baselines are then further smoothed with a 11-night moving mean. The selection of the 6 our LT interval around midnight discards the diurnal effects by the Sq current system. However, these effects are shown in the IL index during the daytime. The calculation of the baseline can also be limited further, for example by selecting only the quietest hour inside the quietest night in the 11-night window. This gives even a less disturbed average. However, the 6-hour average is statistically more robust and sufficient, since quiet nights surely exist in the sliding 11-night window.

In this thesis a standardized $IL_S(st)$ index is also used. The station $IL_S(st)$ index can be created for any station by standardization

$$IL_S(st) = \frac{IL(st) - \overline{IL(st)}}{\sigma_{IL}(st)}, \tag{4.9}$$

where st is the IAGA code of the station, $\overline{IL(st)}$ is the mean value of the whole $IL(st)$ index and $\sigma_{IL}(st)$ is the corresponding standard deviation. Equation (4.9) transforms the deviations (distance from the mean value) in the IL index into units of standard deviation. The $IL_S(st)$ indices are used to examine the latitudinal differences between the station $IL(st)$ indices. Note that $IL(st)$ (and $IL_S(st)$) index derived from a single station simply describes the magnetic deviation from the stations baseline, since no superposing of stations is done with only one station.

4.4 Geomagnetically induced currents

Geomagnetically induced currents (GIC) are electric currents induced in electric conductors, caused by near-Earth currents. GIC are driven by the geoelectric field induced from the variability of the geomagnetic field. The geoelectric field drives the GIC, e.g., in man-made technological infrastructures, such as power lines, pipelines and railways, potentially imposing a natural threat to the technology-dependent societies (Pulkkinen et al., 2017). However, the geoelectric field also drives currents inside the conductive seawater and the crust of the Earth, affecting the ground-based geomagnetic measurements, and eventually the geomagnetic indices.

Figure 25 shows two geoelectric field distributions. Figure 25a has an eastward geoelectric field with a large average in the green group. Figure 25b has an westward geoelectric field with a large average in the red group. Much stronger and more local station-specific intensity spikes can also exist (Pulkkinen et al., 2015). Horizontal

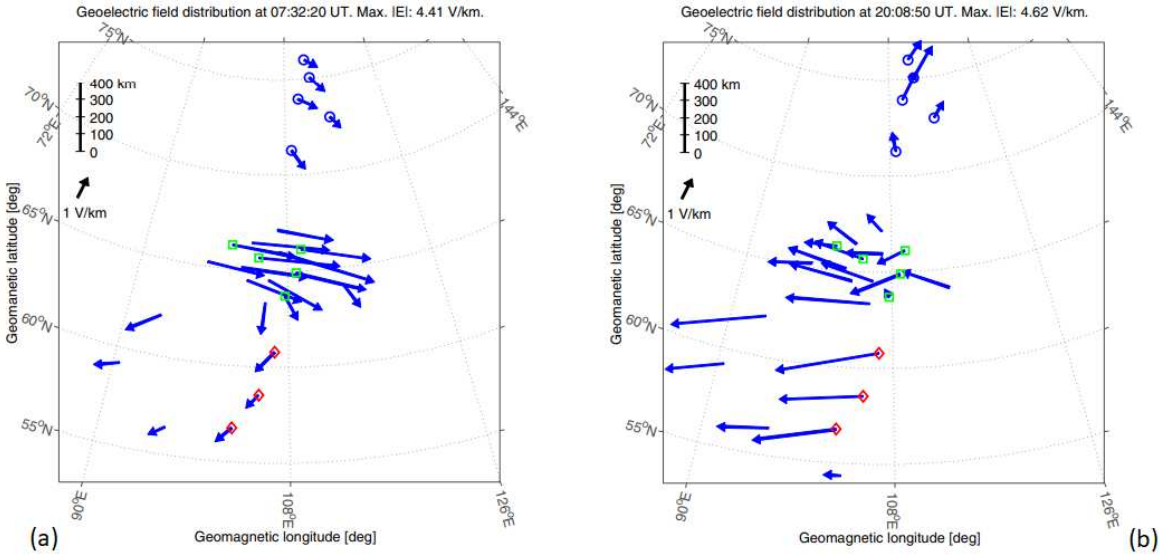

Figure 25: (**a**) Geoelectric field distribution computed from 23 IMAGE magnetometers on November 24, 2001 at 07:32 UT. The *blue*, *green* and *red* colors indicate the three station groups used in spatial averaging. The *green* group generates the largest average geoelectric field magnitude of 2.8 V/km. Corrected geomagnetic coordinates and Oblique Mercator map projection are used. (**b**) Same as in (**a**), but for October 30, 2003 at 20:08 UT. The red group generates the largest average geoelectric field magnitude of 4.0 V/km (Pulkkinen et al., 2015).

$\mathrm{d}B/\mathrm{d}t$ ($\mathrm{d}H/\mathrm{d}t$) values have been found to vary in small spatial scales which contributes to the difference in local GIC (Dimmock et al., 2020). In the GIC research, the local variations of the geoelectric field can be approximated to originate from external sources (near-Earth currents). Compared to these sources, the variability of the local conductivity of the crust plays a smaller role (Pulkkinen et al., 2008). However, knowledge of the conductivity of the crust is also of high importance (Dimmock et al., 2020).

In the case of the IL index, the time-varying magnetic fields leading to induced geoelectric fields and currents are mainly due to the auroral electrojets. However, the exact magnetospheric processes responsible for the time variations of the magnetic field are unclear. The direction of the geoelectric current is usually east-west oriented (Pirjola, 2000; Pulkkinen et al., 2015), which can affect the X and Z components of the geomagnetic field measurements. The Z component is strongly affected if the station is northward or southward of a strong GIC. The X component (IL index) is evaluated to be affected up to about 20% on average by GIC, but the amount can rise to 40% at a substorm onset (Tanskanen et al., 2001). Figure 26a shows, as a superposed epoch curve, how much the internal sources (GIC) contribute to substorms, on average, in the IL index. Figure 26b shows similarly the percentual amount of the external source.

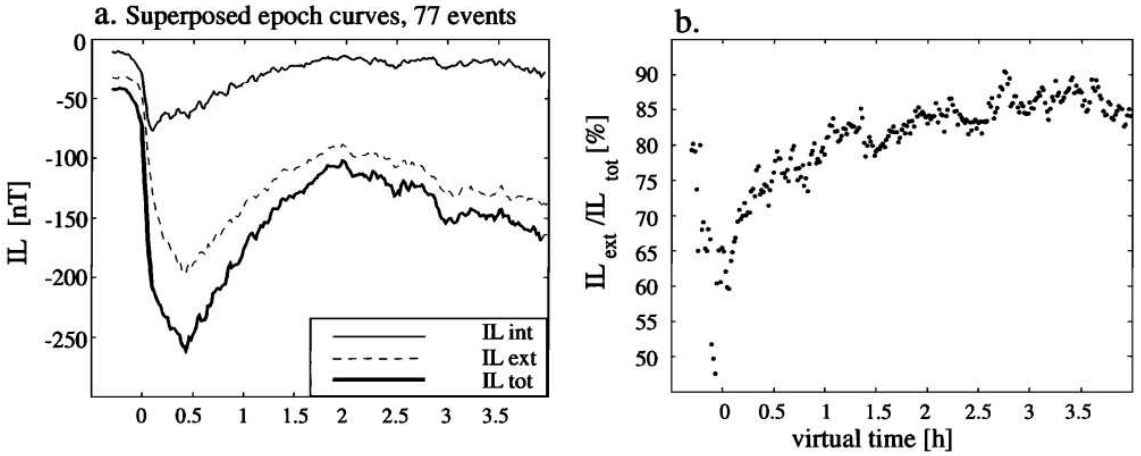

Figure 26: (**a**) Superposed epoch analysis for 77 substorms during 1997, showing the internal (GIC) contributions IL_{int}, the external contributions IL_{ext} and the total index IL_{tot}. (**b**) Same analysis for the ratio IL_{ext}/IL_{tot} (Tanskanen et al., 2001).

5 Data and methods

The data source in this thesis is the International Monitor for Auroral Geomagnetic Effects (IMAGE) magnetometer network. The IL index is formed from 40 IMAGE stations listed in Table 1 and shown in Figure 24. The standardized station $IL_S(st)$ indices are formed following Equation (4.9), for the subset of 11 IMAGE stations. The subset is marked with asterisks in Table 1 and yellow dots in Figure 24.

The IL index is used to study magnetic disturbances caused by the westward electrojet during substorms. Substorms leave distinct magnetic signatures to the index. Thus, times with such signatures can be identified from the index with an algorithmic approach. These substorm identification algorithms are created and used to form a list of substorm onsets.

5.1 IMAGE magnetometer network

The IMAGE stations are located in Northern Europe, distributed in a narrow longitude range, but extensively in latitude. The long and dense latitudinal coverage makes the network exceptionally good for the studies of high-latitude currents, i.e., the auroral electrojets. Geographical latitudes and longitudes, the measuring start date and the data coverage of the used 40 IMAGE stations are shown in Table 1. The same information plus the CGM coordinates for all of the stations can be found from the IMAGE website (`https://space.fmi.fi/image/www/index.php?page=stations`). Data availability for all 44 IMAGE stations can be seen in Figure 27. Stations ALT, KAU, LEK and SUW were not used in this work due to ALT and KAU having no data for 1993-2020, LEK having data only for years 2000-2006 and SUW having poor data quality. As seen, data availability is quite good for most of the stations. Stations of the subset form the most uniform dataset, with a very good

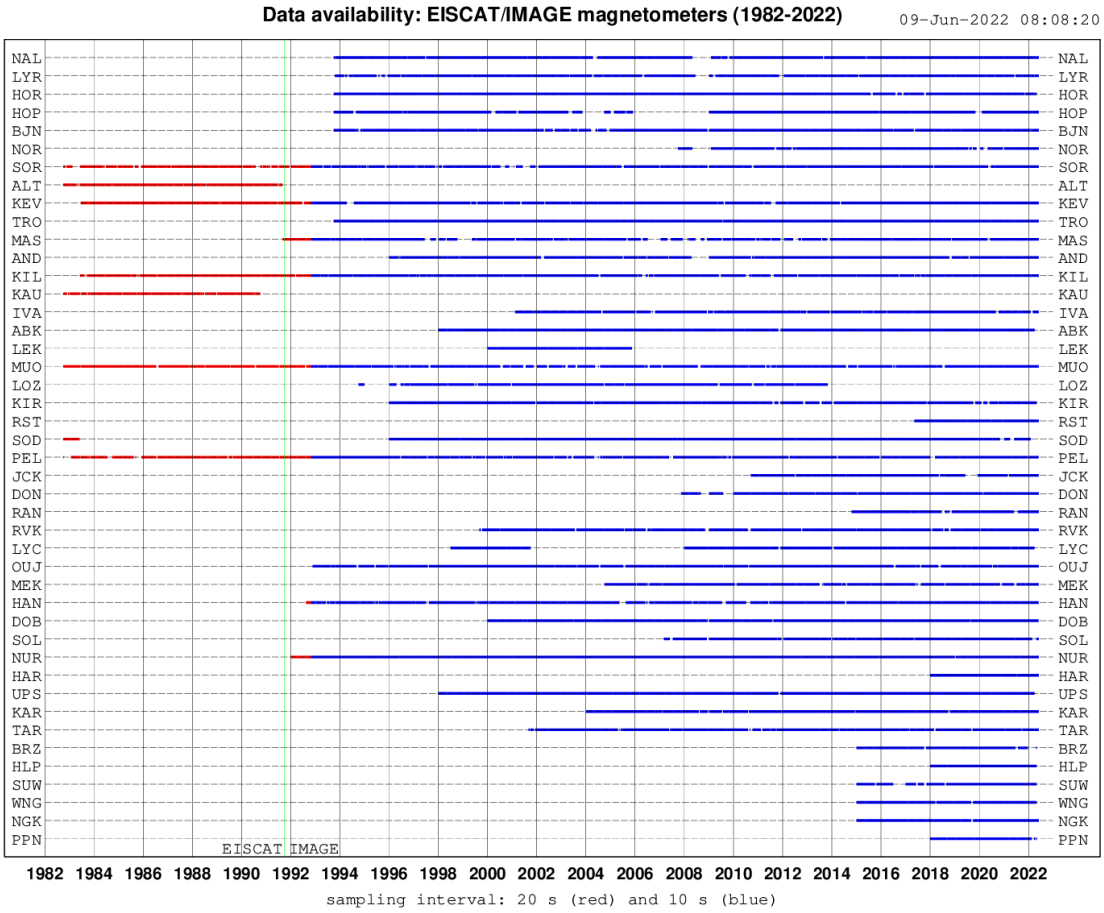

Figure 27: IMAGE magnetometer network data availability. The change from red to blue bars depict the change of the resolution from 20 s to 10 s. The green bar shows the start time of the IMAGE project (`https://space.fmi.fi/image/www/index.php?page=availability`).

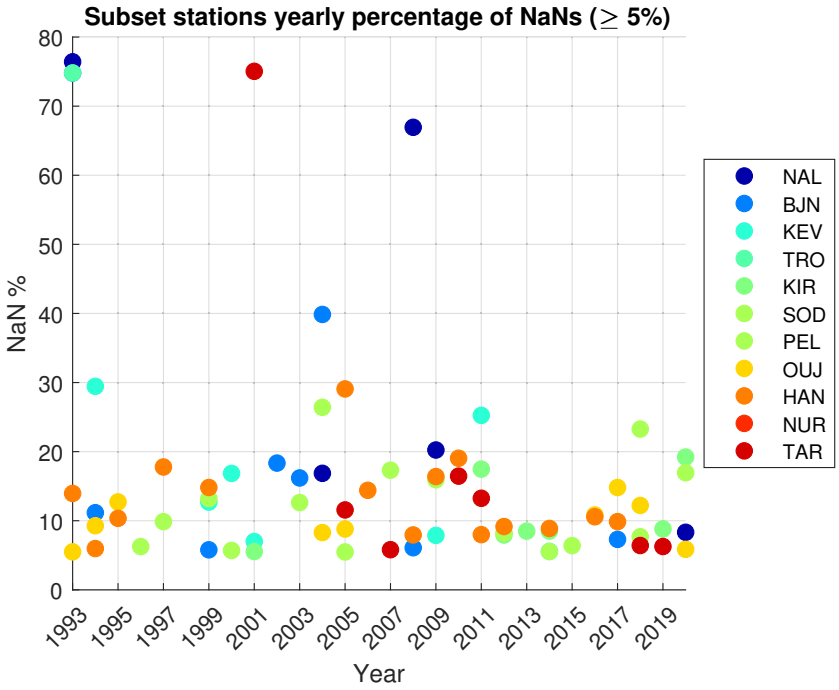

Figure 28: Yearly data gap (NaN) percentages for the subset stations for years when the NaN percentages were larger than 5%. Color is ordered by station latitude, blue indicating the northernmost, red the southernmost station.

data coverage.

Data coverage of the $IL(st)$ index directly depends on the data coverage of the respective station of the subset, since no superposed value from another station is used to replace the missing value. Thus, the yearly data gaps (NaN percentages) of the subset of stations are shown in Figure 28. The yearly NaN percentages were plotted only if they were larger or equal to 5%. Figure 28 shows that in all years except 1996, 1998, 2012-2015 and 2019, at least one stations has a NaN percentage larger than 10%, but NaN percentages above 20% are relatively rare. Stations with large NaN percentages of >20% of NaNs or more and years are: NAL in 1993 (77%, start year), 2008 (67%), 2009 (21%), BJN in 2004 (40%), KEV in 1994 (30%), 2011 (26%), TRO in 1993 (75%, start year), PEL in 2004 (27%), 2018 (24%), HAN in 2005 (30%), TAR in 2001 (76%, start year).

5.1.1 Data corrections

In general, ground-based magnetometer data is prone to data defects, and their correction is a laborious task. IMAGE data are no exception. The main problems in the IMAGE data are baseline jumps and data outliers. The instrument baselines can hold for a long time, and then abruptly jump to a different value. Even more erratic, short-term baseline jumps exist. Nonetheless, the data was carefully curated. Many baseline jumps were detected and fixed to correspond the current

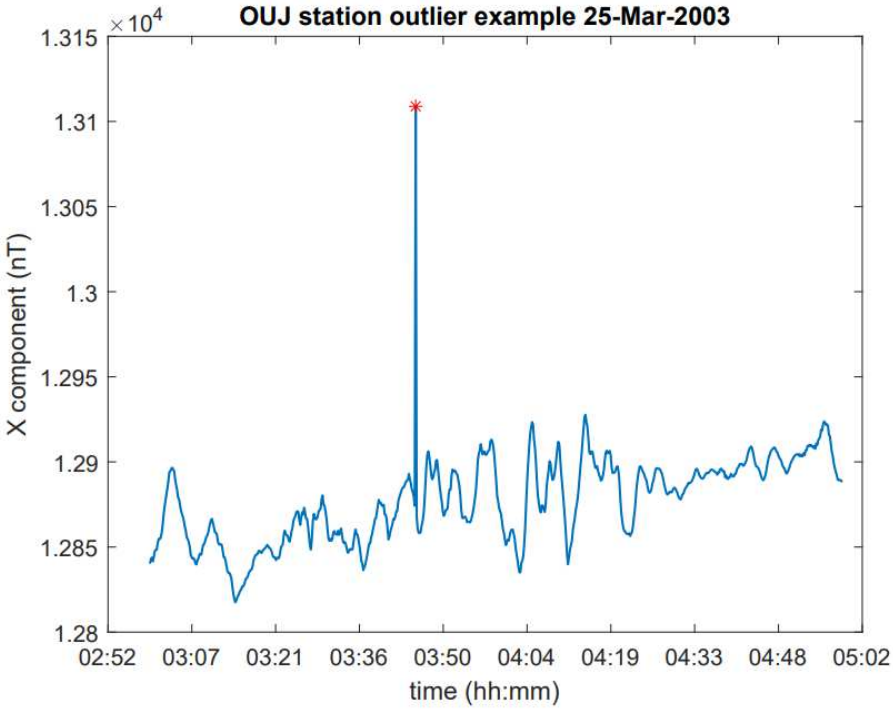

Figure 29: Example of a data outlier in 10s resolution data of the X component of the OUJ station, from 15 March 2003. The outlier value is marked with a red asterisk.

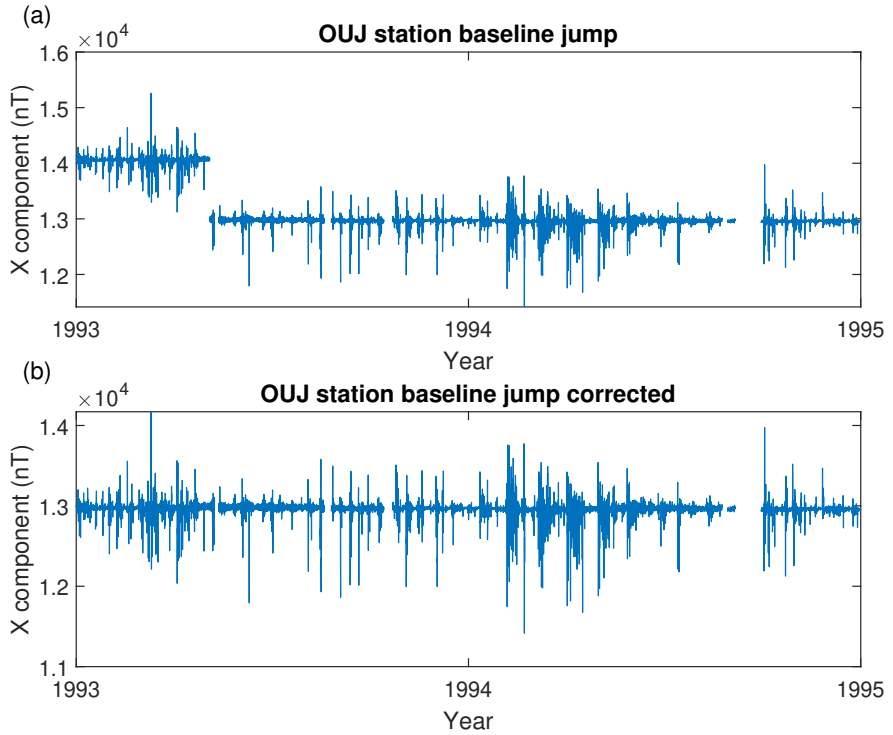

Figure 30: (**a**) Raw OUJ data with a baseline jump at the beginning. (**b**) Corrected OUJ data. Data before the baseline jump lowered to correspond the current baseline.

baseline or a model baseline. A geomagnetic model (yearly IGRF values) for the station coordinates was acquired from the NOAA magnetic field calculator (`https://www.ngdc.noaa.gov/geomag/calculators/magcalc.shtml#igrfwmm`) and used as a model baseline, if the instrument baseline was missing. Potential outliers were detected with an automated method that uses median filtering, and compares the distance of data points to the filtered data. The potential outliers were examined visually, and clear outliers were changed to NaNs. Figure 29 shows an example of a found outlier in raw 10s resolution data from OUJ station. The outlier was a one-value spike of $\sim 230\,\mathrm{nT}$, and thus interpreted as a data defect. Figure 30 shows an example of a baseline jump in raw 10s resolution data from OUJ station. The data before the jump was lowered 1086 nT to correspond the (current) baseline after the jump.

5.2 Substorm identification algorithms

The algorithmic approach to identify substorms from IL-type indices follows the assumption, that the sudden enhancement of the westward electrojet marks the onset of substorm expansion. The algorithms usually use certain threshold values for the depression of the H component to interpret it as a substorm onset (Newell & Gjerloev, 2011). Additional criteria, such as a threshold for the growth or the recovery phase can be added to validate the found onset (Tanskanen, 2009). The substorm theory supports the idea that a large and sudden depression of the H component is an indication of substorm expansion. However, there is a problem in the actual criteria, since unique threshold values indicating a substorm depression do not exist. Accordingly, methods for identifying substorms without thresholds have also been developed, for example, the SOPHIE technique that identifies substorms by evaluating the percentiles of negative and positive $\mathrm{d}B/\mathrm{d}t$ moments (Forsyth et al., 2015).

Since other current systems are also known to enhance along with the westward electrojet, the disturbances from these currents can be detected as well. One example is the MPB index that measures the positive bay signal in the X and Y components from the SCW FAC at low to mid-latitudes. The MPB index is defined as the mean value of the sum $X^2 + Y^2$ measured by all the nightside stations at each instant of time (McPherron & Chu, 2017).

5.2.1 Negative bays

In this thesis, a substorm list from the IL index is formed, using a modified SSeeker identifying algorithm (Tanskanen, 2009). The algorithm finds abrupt and notable negative deviations in the IL index, and is defined as follows:

1. The expansion phase is found by studying the IL index within a +15 minute running window. If the IL index decreases more than 80 nT in the 15 minute window, the drop is steep and large enough to indicate an expansion phase. Then, the onset of the expansion phase (substorm onset) is determined to be the moment, when the IL index has decreased by more than 20 nT from the start of the same window. This is

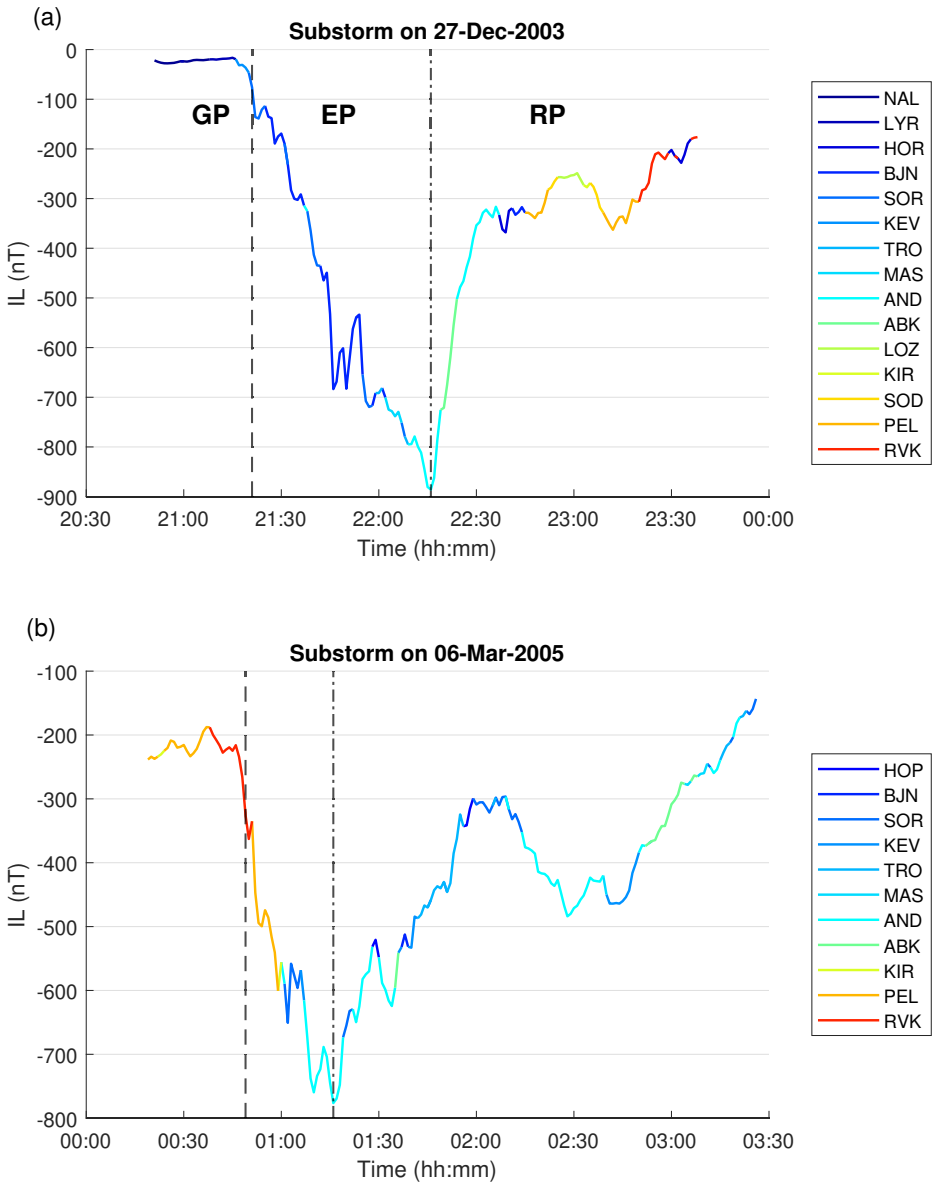

Figure 31: (**a**) Example of an algorithmically found substorm from 27 December 2003, showing the growth phase (GP), expansion phase (EP) and the recovery phase (RP). The color shows the station contributing to the IL index. The stations in the legend are in latitudinal order. The dashed line indicates the substorm onset, and the dash-dotted line the substorm peak value. The IL index was close to zero at the onset. (**b**) Same as (**a**), but for a substorm from 6 March 2005, when the IL index was smaller than $-200\,\mathrm{nT}$ at the onset.

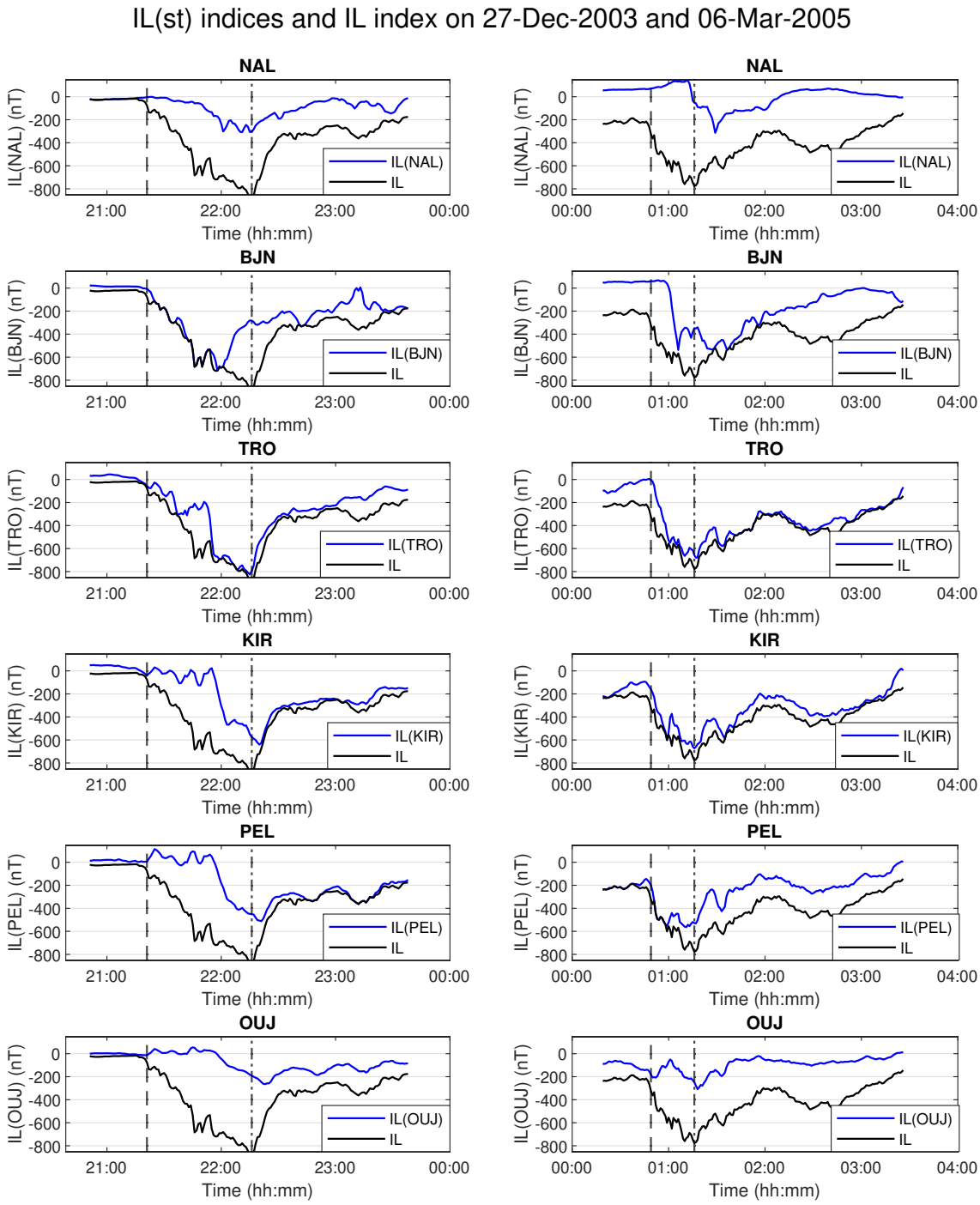

Figure 32: Left panel: same substorm as in Figure 31a, in $IL(st)$ indices of NAL, BJN, TRO, KIR, PEL and OUJ stations. The dashed line indicates the substorm onset and the dash-dotted line the substorm peak value from Figure 31a. Right panel: same as right, but for the substorm from Figure 31b, and the dashed line and the dash-dotted line are the onset and peak from 31b.

because the actual onset is the moment the IL index starts decreasing, which is not (necessarily) the first value in the window.

2. The growth phase (substorm start) was defined to start at maximum 30 min before the substorm onset. This is only half of the growth phase duration determined in Section 4. The growth phase was determined to be 30 minutes, if the whole 30 min period was equal or smaller than -20 nT (i.e., overall negative IL index), or the whole 30 min period was larger than -20 nT. Otherwise the first moment when the IL index decreased to be equal or smaller than -20 nT in the 30 min period, was determined to be the beginning of the growth phase.

3. The substorm was defined to end, when the IL index had recovered to 20% of the minimum value since the start of the expansion phase onset. Maximum length after onset time was set to be 240 minutes (4 h). Then, the maximum possible length for the whole substorm (30 min + onset + 240 min) was thus 271 minutes (4 h 31 min). Substorms with growth phase starting less than 10 min after the end of the previous substorm were combined to the previous substorm. Thus, multiple onsets were combined as one substorm if the substorm did not recover enough (end) before the subsequent onset.

4. Substorm had to be longer than 15 min (from start to end), the peak amplitude (minimum value between onset and end) had to be larger than 100 nT and the substorm onset had to occur between 16-03 UT (optimal IMAGE coverage).

The above method found only fairly evident substorms. The growth and recovery criteria were essential for the success of the method. With the definition of the growth and recovery phases, properties such as the duration and amplitude of the substorm are acquired. The amplitude of the substorm is quite accurate, since the good latitudinal coverage detects the expansion of the auroral oval and the momentary intensity of the electrojet. The same algorithm was also implemented and applied to the station $IL(st)$ indices to form station-related substorm lists for each IMAGE station in the subset of 40 stations (Table 1).

Figures 31a and 31b show the IL index during a substorm. In Figure 31a, the IL index is close to zero at the onset, and in 31b the IL index is smaller than -200 nT at the onset. Each of the three substorm phases are evident in both Figures. The color of line shows the station measuring the largest negative H deviation, contributing its measurement to the IL index. The color depends on latitude, thus stations with similar color are roughly at the same latitude. The contributing station varies strongly. However, no large conclusions of how the contributing stations vary under substorms should be drawn from two examples.

In the case presented in Figure 31a, the westward electrojet affects mostly the stations from BJN (74.50° N, 19.20° W) to SOR (70.54° N, 22.22° W) during most of the expansion phase, but during the last 15 minutes of the expansion phase, the electrojet affects mostly the TRO (69.66° N, 18.94° W), MAS (69.46° N, 23.70° W) and AND (69.30° N, 16.03° W) stations. During the recovery phase, the electrojet diminishes, but the largest negative deviations are still seen at AND and ABK (68.35°

N, 18.82° W). A sudden change to northern stations and back to SOD (67.37° N, 26.63° W) is seen at ∼22:45, indicating that the electrojet is quite wide in latitude. The fact that even during the recovery phase the IL index is still quite largely negative indicates that the electrojet is still enhanced and expanded. Even RVK (64.94° N, 10.98° W), the southernmost (and westernmost) station is mostly affected at the end of the recovery phase.

In the case represented in Figure 31b, the already enchanced westward electrojet affects the stations from KIR (67.84° N, 20.42° W) to RVK during the growth and expansion phases, indicating that the already enhanced westward electrojet is at rather low latitudes. During the last 30 minutes of the expansion phase, stations SOR (68.02° N, 23.53° W), KEV (69.76° N, 27.01° W) and AND are mostly affected, indicating that the westward electrojet is enhanced at the higher latitudes. Stations AND and ABK are mostly affected throughout the recovery phase, with the westward electrojet occasionally affecting the northern stations as well, indicating that the electrojet is at higher latitudes than during the growth phase and during the onset.

The left panel of Figure 32 shows the substorm from Figure 31a in $IL(st)$ indices of stations NAL, BJN, TRO, KIR, PEL and OUJ (blue line), and the resulted IL index (black line). The onset (dashed line) is seen mostly in IL(TRO), and the largest negative bay is seen in IL(BJN) and IL(TRO), with the IL(TRO) decreasing clearly after IL(BJN). IL(NAL) reaches its minimum at the same time as IL(TRO), but has the smallest negative bay. The substorm peak (dash-dotted line) coincides with the peak in IL(TRO). IL(KIR) and IL(PEL) share a similar magnetic time evolution, with IL(KIR) having the largest peak amplitude. IL(OUJ) show similar time evolution, but weaker in amplitude. All three stations peak slightly after IL(TRO), indicating that the westward electrojet descends to slightly lower latitudes after the peak. IL(PEL) and IL(OUJ) oscillate during the recovery phase, while IL(TRO) and IL(KIR) recover more steadily. IL(PEL) contributes to the IL index during the recovery phase. At the onset, a small positive bay of roughly 110 nT is seen in IL(PEL) indicating an enhanced eastward electrojet.

The right panel of Figure 32 shows a similar stackplot for the substorm from Figure 31b. The onset (dashed line) is seen mostly at IL(TRO), IL(KIR) and IL(PEL). IL(NAL) and IL(BJN) increase to positive values during the expansion phase. IL(OUJ) increases during the expansion phase. IL(BJN) starts decreasing roughly 10 minutes after the onset. A positive bay is seen in IL(NAL) during the expansion phase. IL(NAL) and IL(BJN) show a negative bay right after the expansion phase, indicating that the westward electrojet enhances in higher latitudes after the expansion. At roughly 01:30 IL(TRO)-IL(PEL) show another negative bay. IL(OUJ) shows similar recovery phase as well, only smaller in amplitude.

6 Statistical properties of substorms

The algorithm defined above was implemented and used on the IL index of 40 stations listed in Table 1. A total of 14246 substorms were found for the years 1993-2020. The average duration was 3 h 1 min. 24% of the substorms had the length of 271 minutes (the determined maximum length). The average amplitude was 411 nT. In 15.2% of the substorms, the IL index was smaller than -200 nT at the onset. With the substorm list and the acquired properties for each substorm, we can analyse the long-term change of the substorm number, mean duration and mean amplitude.

6.1 Solar cycle variation

As stated in Section 2.4, the geomagnetic activity is seen to maximize in the declining phase, due to the HSS and CME hitting the Earth. Accordingly, yearly substorm numbers show similar behavior. Figure 33a shows the yearly substorm numbers in 1993-2020 with the yearly sunspot numbers. The yearly substorm numbers do not correlate significantly with the yearly sunspot numbers (correlation coefficient $r = 0.20$ and p-value $p = 0.31$). The substorm number is seen to maximize in the declining phase. Solar cycle 23 has the largest substorm number maximum of 786 in year 2003, end of the solar cycle 22 (only the end of the declining phase visible) has the second largest yearly substorm number of 687 in year 1994. In solar cycle 24 the substorm number maximum of 565 is in year 2016. In general, substorm number minima seem to occur close to the sunspot minima, at the start of the ascending phase. The smallest yearly substorm number minimum by far was in 2009. The substorm numbers during the two other solar minima were much higher.

Figure 33b shows the yearly substorm numbers together with the yearly time percentages of CMEs and HSS (see Section 2.4 and Figure 5). The yearly substorm numbers correlate fairly with the yearly HSS time percentages ($r = 0.69$ and $p = 4.92{\cdot}10^{-5}$). On the other hand CME time percentages correlate very weakly with the yearly substorm numbers ($r = 0.08$ and $p = 0.70$). However, the yearly substorm numbers correlate even slightly better with the sum of the yearly CME and HSS time percentages ($r = 0.74$ and $p = 8.00 \cdot 10^{-6}$), than with the HSS time percentages alone. Figure 33b shows that CMEs increase the yearly substorm number especially in solar maximum years, when the time percentage of HSS is low (1998-2000 and 2012).

Figures 33c and 33d show the yearly substorm numbers together with yearly averages of the solar wind speed and the IMF intensity, respectively. The yearly substorm numbers correlate very strongly with the yearly averages of the solar wind speed ($r = 0.90$ and $p = 8.06 \cdot 10^{-11}$). Fair correlation is also found between the yearly substorm numbers and the yearly IMF intensity ($r = 0.61$ and $p = 6.01 \cdot 10^{-4}$). Thus, Figure 33 shows that the solar wind speed is the main driver of the substorm activity at least of yearly resolution. This also leads to the good correlation between substorm numbers and HSS.

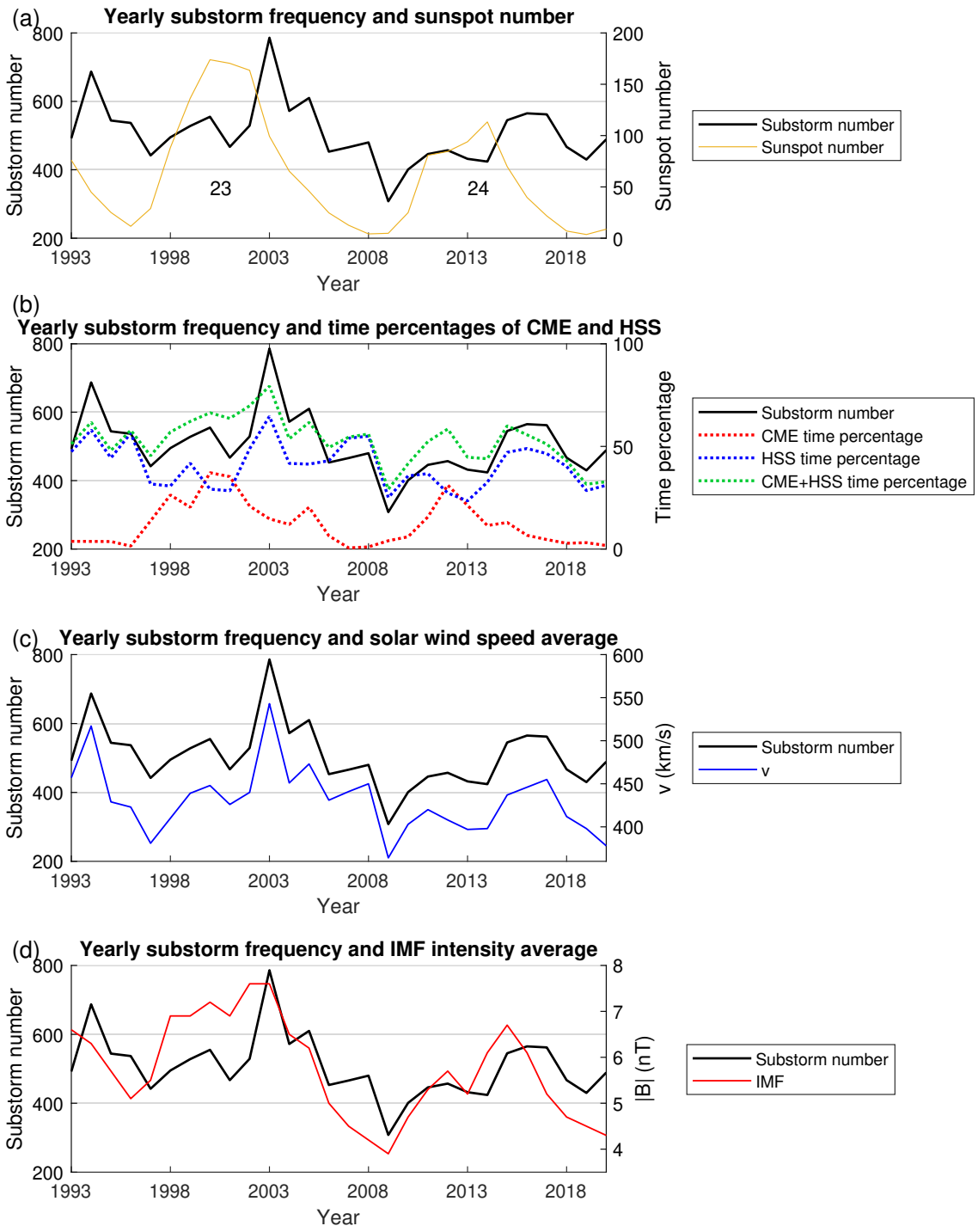

Figure 33: (**a**) Yearly substorm numbers with yearly mean total sunspot numbers for years 1993-2020; (**b**) Yearly substorm numbers with yearly percentages of CME flows and high-speed streams; (**c**) and (**d**) Yearly substorm numbers with yearly solar wind speed and IMF intensity averages (`https://www.sidc.be/silso/`; `https://omniweb.gsfc.nasa.gov/`).

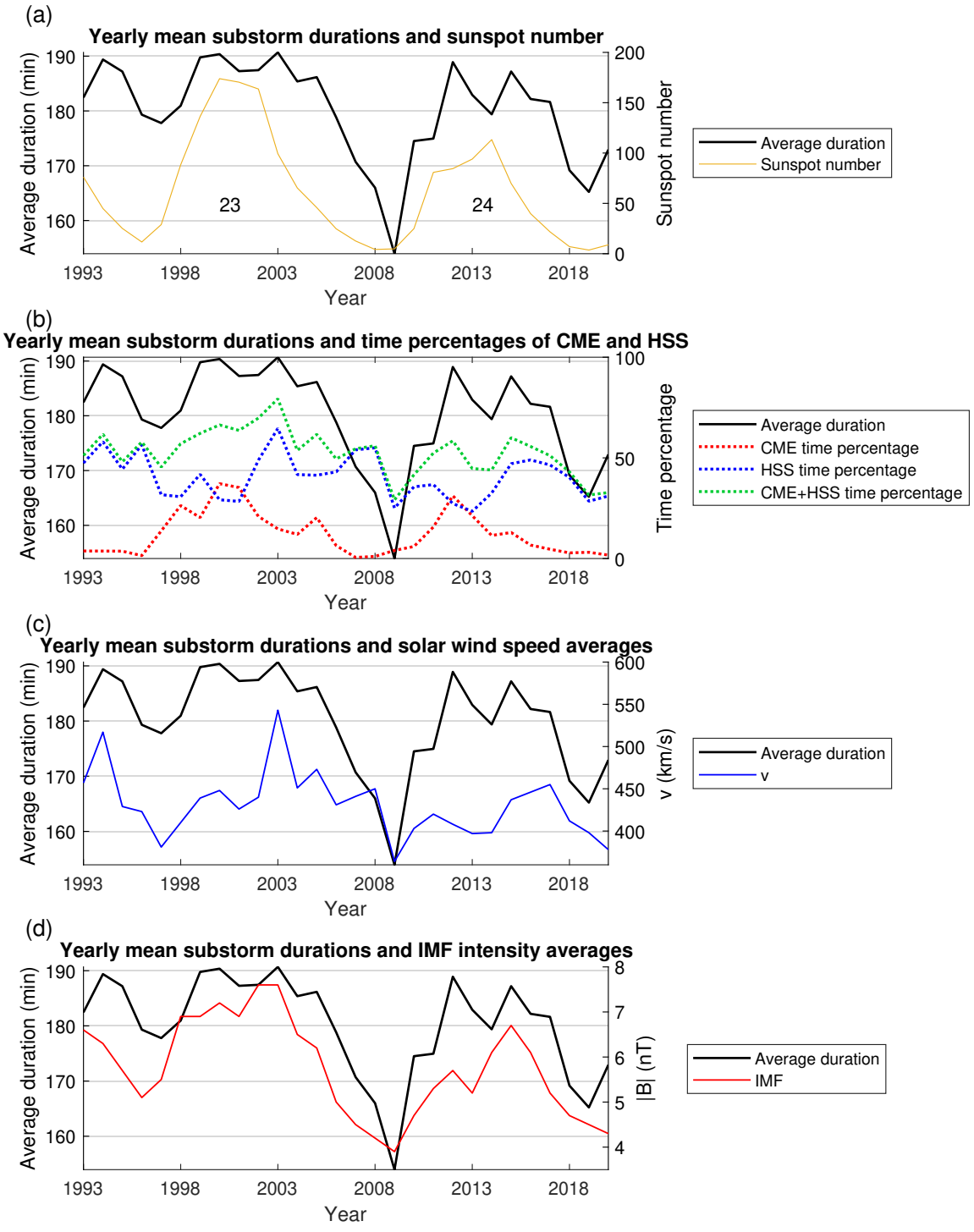

Figure 34: (**a**) Yearly mean substorm durations with yearly mean total sunspot numbers for years 1993-2020; (**b**) Yearly mean substorm durations with yearly percentages of CME flows and high-speed streams; (**c**) and (**d**) Yearly mean substorm durations with yearly solar wind speed and IMF intensity averages (`https://www.sidc.be/silso/`; `https://omniweb.gsfc.nasa.gov/`).

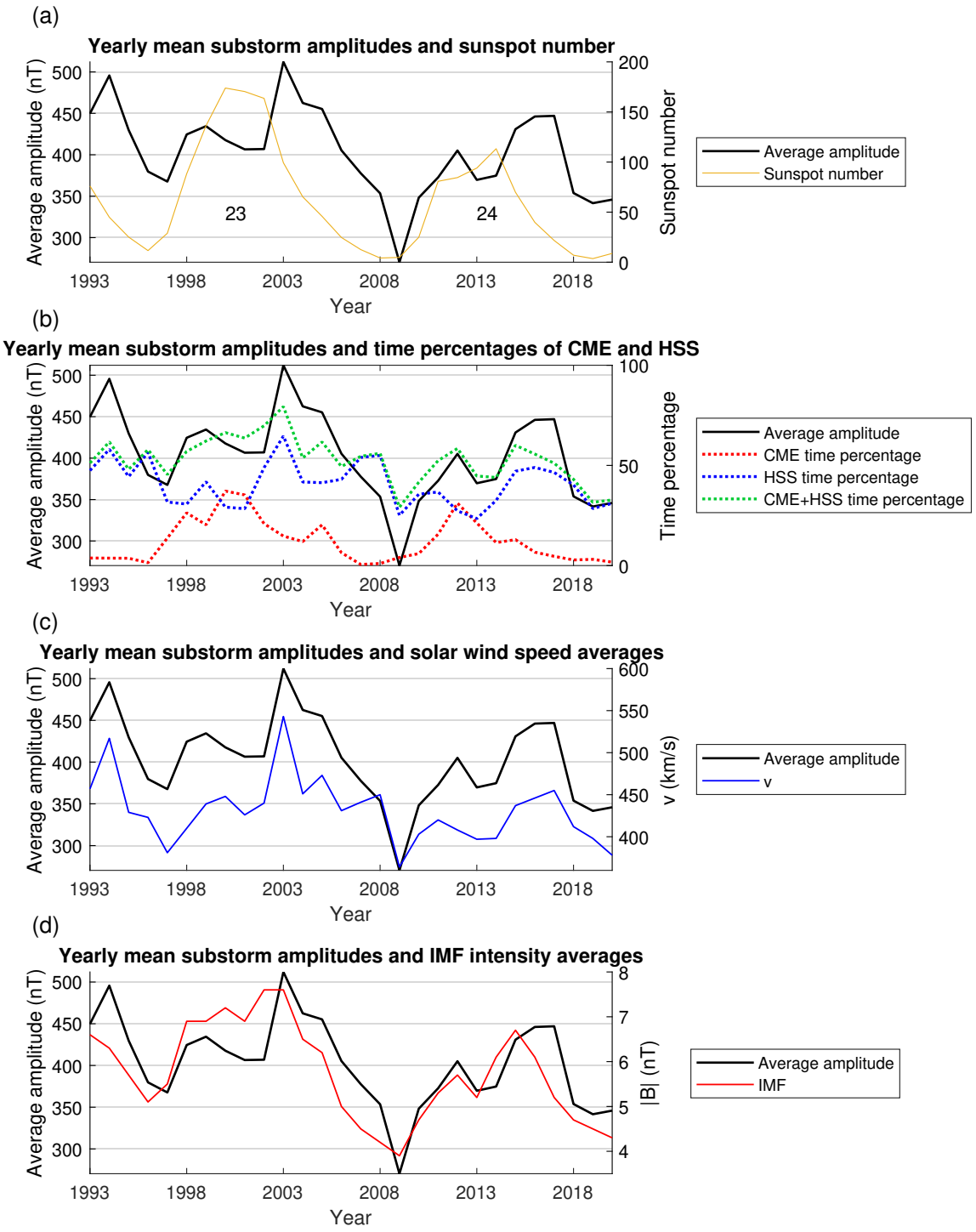

Figure 35: (**a**) Yearly mean substorm amplitudes with yearly mean total sunspot numbers for years 1993-2020; (**b**) Yearly mean substorm amplitudes with yearly percentages of CME-associated flows and high-speed streams; (**c**) and (**d**) Yearly mean substorm amplitudes with yearly solar wind speed and IMF intensity averages (`https://www.sidc.be/silso/`; `https://omniweb.gsfc.nasa.gov/`).

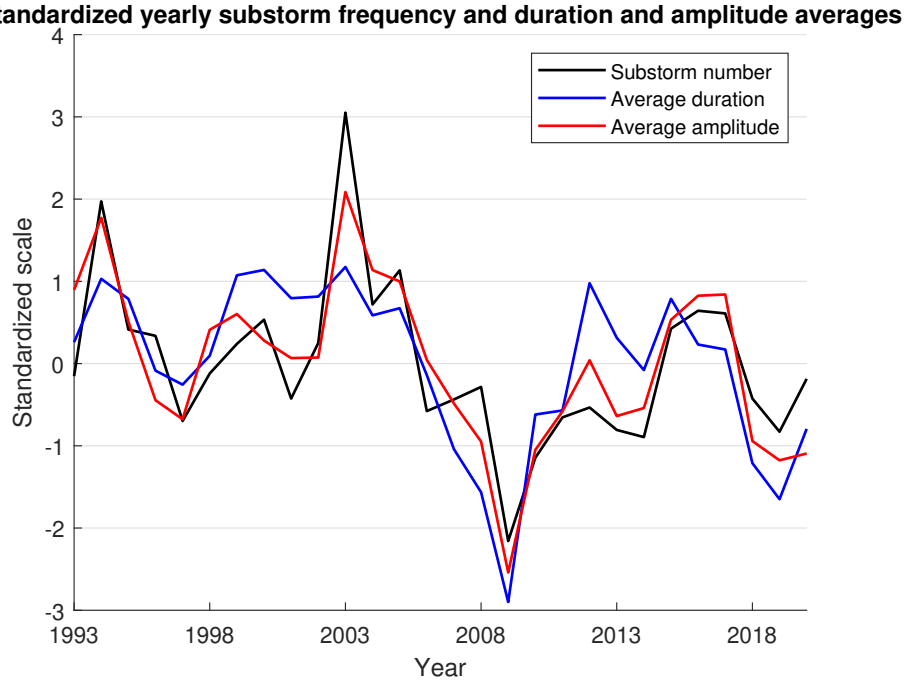

Figure 36: Standardized yearly substorm number, duration average and amplitude average for years 1993-2020.

Figure 34a shows the yearly mean substorm durations (mean length of substorms) with the yearly sunspot numbers. The yearly mean substorm durations correlate fairly well with the yearly sunspot numbers ($r = 0.65$ and $p = 1.59 \cdot 10^{-4}$). The longest substorms (3 h 11 min) of solar cycle 23 are found in 2003, 1994 and of solar cycle 24 (3 h 9 min) in 2012. The shortest substorms (2 h 34 min) by far are found in 2009. Duration has minima also at solar minima in 2019 and in 1997.

Figure 34b shows the yearly mean substorm durations for the yearly percentages of CMEs and HSS. The yearly mean substorm durations do not correlate with the yearly HSS time percentages ($r = 0.23$ and $p = 0.24$), but do correlate weakly with CME percentages ($r = 0.57$ and $p = 0.002$). Instead, the sum of the yearly CME and HSS percentages correlates strongly with the yearly mean substorm durations ($r = 0.76$ and $p = 3.27 \cdot 10^{-6}$).

Figures 34c and 34d show the yearly mean substorm durations with yearly averages of the solar wind speed and the IMF intensity, respectively. The yearly mean substorm durations correlate weakly with the yearly solar wind speed averages ($r = 0.57$ and $p = 0.002$), but a stronger correlation is found between the yearly mean substorm durations and the yearly IMF intensity ($r = 0.84$ and $p = 2.37 \cdot 10^{-8}$). Figure 34 thus shows that yearly mean substorm duration depends quite strongly on the yearly average IMF intensity.

Figure 35a shows the yearly mean substorm amplitudes in 1993-2020 together with the yearly sunspot numbers. The temporal variation of the yearly mean amplitude is quite similar to the variation of the yearly substorm number. Similarly as substorm

numbers, the yearly mean substorm amplitudes do not correlate with the sunspot numbers ($r = 0.36$ and $p = 0.06$). The largest substorm amplitude of 512 nT is obtained in 2003. The largest mean amplitude of solar cycle 24 (447 nT) is found in 2017. The smallest substorm amplitude of 270 nT is found in 2009, while the smallest amplitude of solar cycle 24 in 2019 is much larger (342 nT).

Figure 35b shows the yearly mean substorm amplitudes with the yearly percentages of CMEs and HSS. The yearly mean substorm amplitudes correlate weakly with the yearly HSS time percentages ($r = 0.55$ and $p = 0.002$), but does not correlate with CMEs ($r = 0.23$ and $p = 0.24$). Interestingly, as for substorm numbers, the sum of the yearly CME and HSS time percentages correlates quite strongly with the yearly substorm amplitude averages ($r = 0.75$ and $p = 4.53 \cdot 10^{-6}$).

Figures 35c and 35d show the yearly mean substorm amplitudes with the yearly averages of the solar wind speed and the IMF intensity, respectively. The yearly substorm amplitude averages correlate strongly with the yearly solar wind speed averages ($r = 0.85$ and $p = 9.61 \cdot 10^{-9}$), thus further confirming the great similarity with substorm numbers. A fairly strong correlation is found even between the yearly mean substorm amplitudes and the IMF intensity ($r = 0.75$ and $p = 3.85 \cdot 10^{-6}$).

Figure 36 shows the standardized yearly mean substorm numbers, durations and amplitudes, to study their correlation on a yearly scale. Standardization was done by Equation 4.9. The yearly substorm number correlates very strongly with the yearly mean amplitudes ($r_{NA} = 0.88$ and $p_{NA} = 6.11 \cdot 10^{-10}$). The yearly mean substorm durations and amplitudes also correlate fairly strongly even with each other ($r_{DA} = 0.83$ and $p_{DA} = 3.72 \cdot 10^{-8}$). The yearly substorm number correlates fairly strongly even with the yearly mean durations ($r_{ND} = 0.67$ and $p_{ND} = 8.53 \cdot 10^{-5}$). The yearly substorm duration is relatively higher than others close to solar maxima (years 1999-2000 and 2012). In year 2003, the substorm mean durations increases less than the other two. The correlation is mainly driven by the deep miminum in 2009. Without the two years 2008-2009 correlations are weaker: $r_{NA} = 0.86$ and $p_{NA} = 1.59 \cdot 10^{-8}$, $r_{DA} = 0.76$ and $p_{DA} = 6.69 \cdot 10^{-6}$, $r_{ND} = 0.60$ and $p_{ND} = 0.001$.

The overall picture of the Figures 33-36 is that the yearly substorm number is strongly modulated by the yearly solar wind speed average. This is mostly due to the HSS, which occur more often than CMEs (except in sunspot maxima). HSS events are prolonged periods of fast solar wind, where Alfvén waves fluctuate the magnetic field enhancing the southward IMF component and increasing the dayside reconnection. CMEs hit the Earth as a massive structure of magnetized plasma, with suddenly increased solar wind speed and enhanced IMF (see Section 2). On the other hand, the yearly means substorm durations are more affected by the yearly IMF intensity average than the solar wind speed average. HSS time percentages showed no correlation with the yearly average durations, while CME time percentages correlated only weakly with the duration averages. The yearly substorm amplitude averages are more affected by the solar wind speed averages. Thus, the HSS percentage correlates better with the yearly amplitude averages than the CME time percentage.

These results mean that on average, the stronger IMF tends to cause longer substorms, while the mean amplitude of the substorms depend more on the solar wind speed. Physically, these results can be explained so that the solar wind speed v increases the dayside reconnection rate (e.g., Equation (3.12)), thus increasing substorm occurrence. Also due to the increased v, more magnetic flux accumulates into the magnetotail (growth phase), enhancing the magnetotail currents and thus leading to larger substorms. It is difficult to tell from these results alone, why the yearly duration averages correlate better with the yearly IMF intensity. Both the yearly mean durations and amplitudes correlate strongly with each other, meaning that on a yearly scale, stronger substorms are usually longer as well. A possible explanation could come from the fact that storm-time substorms are usually 10% longer in duration, than nonstorm substorms (e.g., Tanskanen et al., 2011). On the other hand, IMF intensity also affects storm intensity.

6.2 Seasonal variation

The seasonal variation was analysed using the whole substorm list (14246 substorms), by plotting the mean substorm number, duration and amplitude for each calendar month separately. Figure 37a shows seasonal variation of the substorm number. Substorm number peaks at winter month 1 and at the spring and fall months 3 and 10. A slight drop can be seen between the winter and equinox peaks at months 2 and 11. Substorm number descends in summer, reaching its minimum at month 6 (summer solstice). Figure 37b shows the seasonal variation of substorm duration. The result is straightforward: substorms seem to be longest in month 6, and shortest in month 12 (winter solstice). At month 6, substorms have an average duration of 3 h 19 min, and at month 12 2 h 41 min. In months 3 and 10, substorms have the average duration of 3 h and 0 min, which is very close to the overall average duration of the substorms (3 h 1 min). Accordingly, there is a dominant semiannual variation in substorm amplitude, a dominant annual variation in substorm duration and a dominant annual and subdominant semiannual variation in substorm number. Figure 37c shows the seasonal variation of substorm amplitudes. Substorm amplitudes peak in months 3 and 10. In month 3, substorms have the average amplitude of 442 nT, and in month 10, 453 nT. The weakest substorms (366 nT) are in month 6.

Figure 38 shows the standardized seasonal variation of the substorm number, duration and amplitude. The seasonal substorm number hardly correlates with the seasonal amplitude average ($r = 0.64$ and $p = 0.02$), which duration has a clean anticorrelation with the seasonal substorm number ($r = -0.76$ and $p = 0.004$), but no correlation with the seasonal amplitude average ($r = -0.1$ and $p = 0.78$).

The overall picture of the seasonal variation of substorms is that in summer, substorms are less frequent, weaker, but longer. Substorms are more frequent and stronger at equinoxes. In winter, substorms are frequent, but shorter and weaker. There are several processes contributing to the seasonal variation of geomagnetic activity in

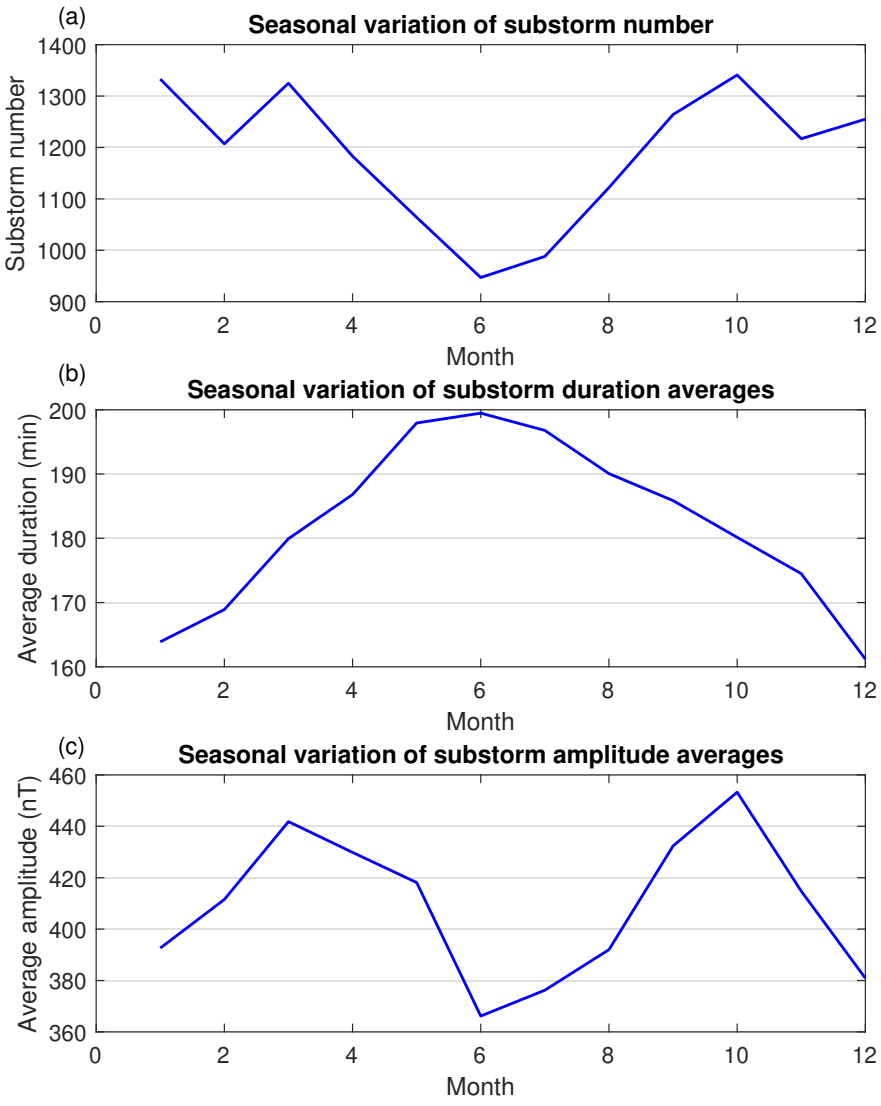

Figure 37: (**a**) Seasonal variation of the substorm number. (**b**) Average duration. (**c**) Average amplitude.

general. Three main explanations exist: the axial hypothesis (e.g., Lockwood et al., 2020a), the equinoctial hypothesis (Cliver et al., 2000) and the Russell-McPherron effect (Russell & McPherron, 1973). Another contribution is the enhanced conductivity of the ionosphere in the summer solstice, when photoionization is increased in the northern hemisphere (Lyatsky et al., 2001). The enhanced conductivity of the ionosphere increases the baseline of magnetic measurements. Thus, substorms show weaker onsets and amplitudes in the IL index in summer, making the algorithmic criteria for the onset detection (80 nT in 15 minutes) too large. This would result into fewer substorms found. This would also partly explain why the substorms are longer but weaker in summer; substorms appear to be weaker due to the increased baseline, however the duration corresponds to that of a stronger substorm. Also, substorms are found to be triggered more easily during lower ionospheric (Pedersen) conductance,

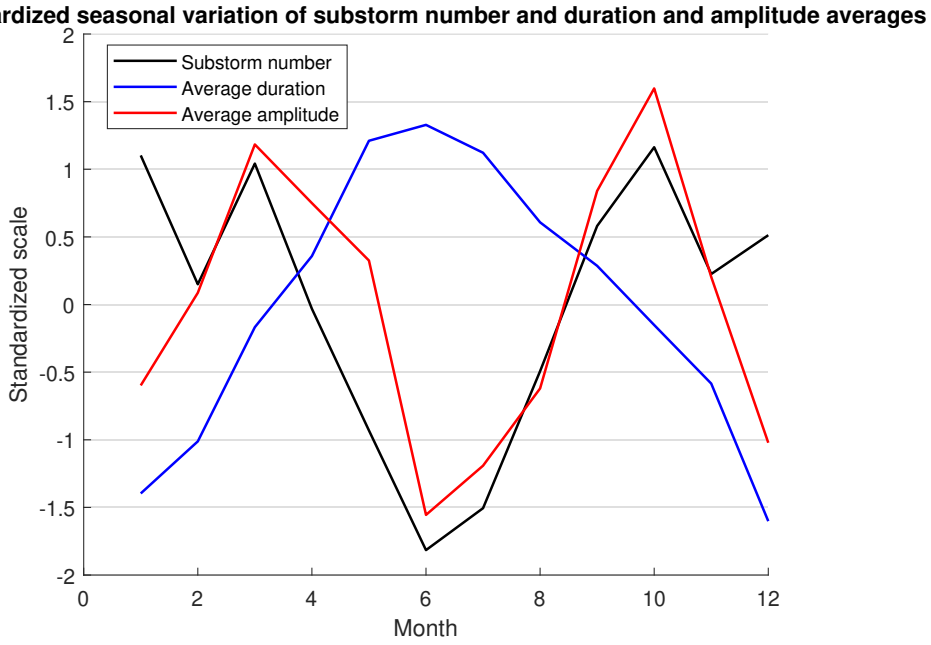

Figure 38: Standardized seasonal variation of the substorm number, average duration and average amplitude.

when the ionospheric conductance of the associated flux tube is lower (Wang & Lühr, 2007). However, this theory is under controversy (Lockwood et al., 2020b).

6.3 Latitudinal distribution

Analysis of the latitudinal variation is based on 11 stations (marked yellow in Figure 24). A substorm list is created from the $IL(st)$ index of the respective station, with an implemented algorithm defined in Section 5.2.1. Each list gives information of the substorm properties at latitude of the respective station.

Figure 39a shows the total number of substorms found from each $IL(st)$ index. The total number of substorms found from the IL index (14246) is shown with the dashed line. Their ratio is shown on top of each bar. The stations found the following number of substorms: NAL 4403, BJN 12637, KEV 9544, TRO 10334, KIR 6383, SOD 5565, PEL 5735, OUJ 2740, HAN 840, NUR 516 and TAR 83. The substorm number decreases almost linearly in latitude from BJN to TAR. However, KEV has smaller substorm number than TRO, although being even slightly higher in latitude (69.76° N). KIR, SOD and PEL have a similar substorm number, due to being close to the same latitude.

Figure 39b shows the total mean duration of the substorms from each $IL(st)$ index. Their ratio to the total mean duration of the substorms from the IL index (3 h and 1 min) is shown on top of every bar. The mean duration of substorms from each station is: NAL 1 h 48 min, BJN 2 h 19 min, KEV 3 h 25 min, TRO 3 h 29 min, KIR

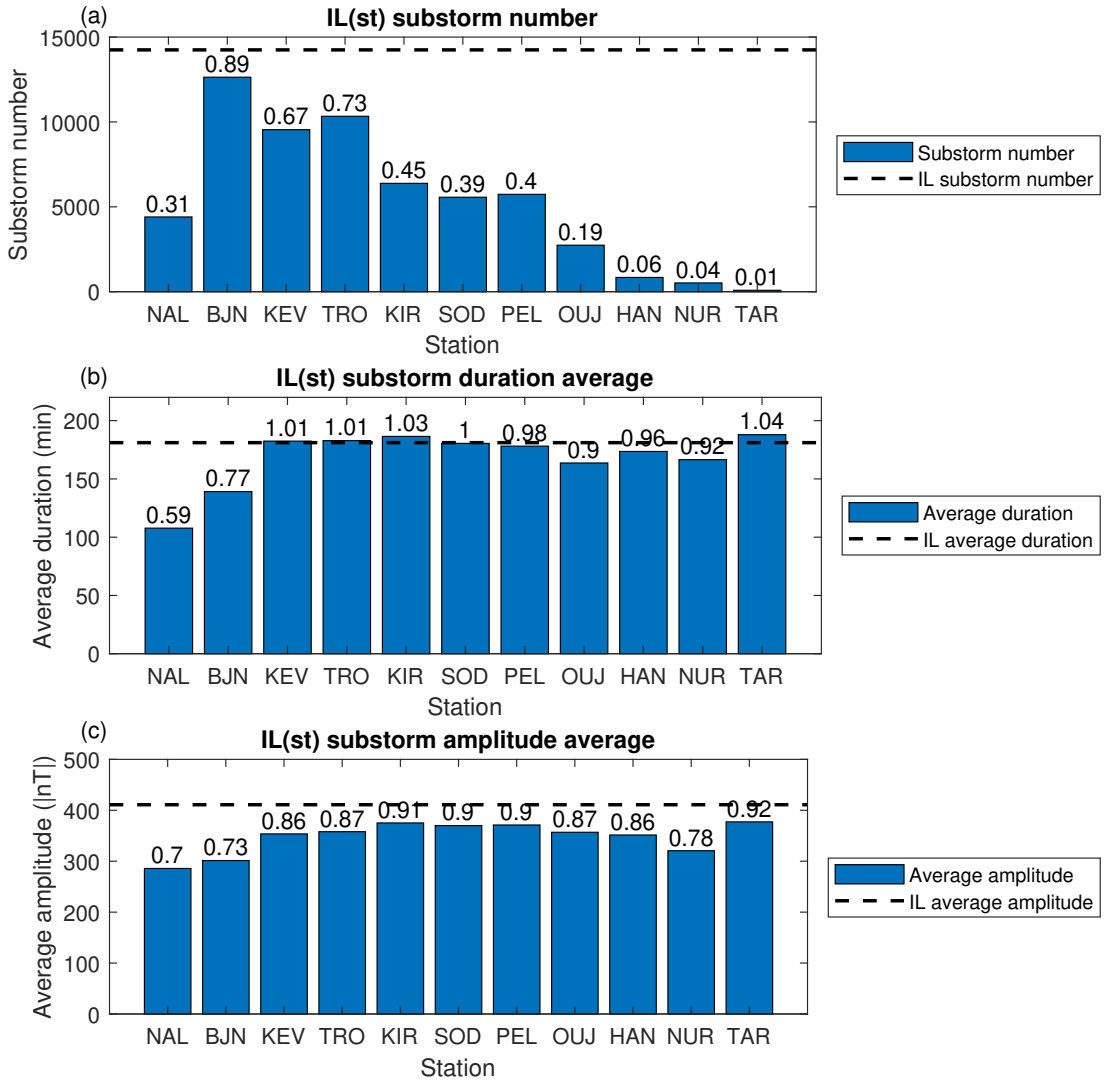

Figure 39: (**a**) Total number of substorms found from each $IL(st)$ index. Dashed line is the total number of substorms found from the IL index. The ratio of the station substorm number and the IL substorm number is shown on top of each bar. (**b**) and (**c**) Correspondingly for total averages of substorm duration and amplitude.

3 h 7 min, SOD 3 h 0 min, PEL 2 h 58 min, OUJ 2 h 44 min, HAN 2 h 54 min, NUR 2 h 47 min, TAR 3 h 8 min. The average duration increases steadily from NAL to KEV. KEV, TRO and KIR have slightly longer mean durations than the mean duration of the IL substorms. SOD has the same mean duration as the IL substorms, and PEL OUJ, HAN and NUR have slightly shorter durations. TAR has the longest substorm duration average, with a ratio of 1.04.

Figure 39c shows the total mean amplitudes of the substorms form each $IL(st)$ index. The ratios to the mean amplitude of the substorms from the IL index (411 nT) is shown on top of every bar. The mean amplitude of found substorms from each station is: NAL 286 nT, BJN 301 nT, KEV 354 nT, TRO 358 nT, KIR 375 nT, SOD

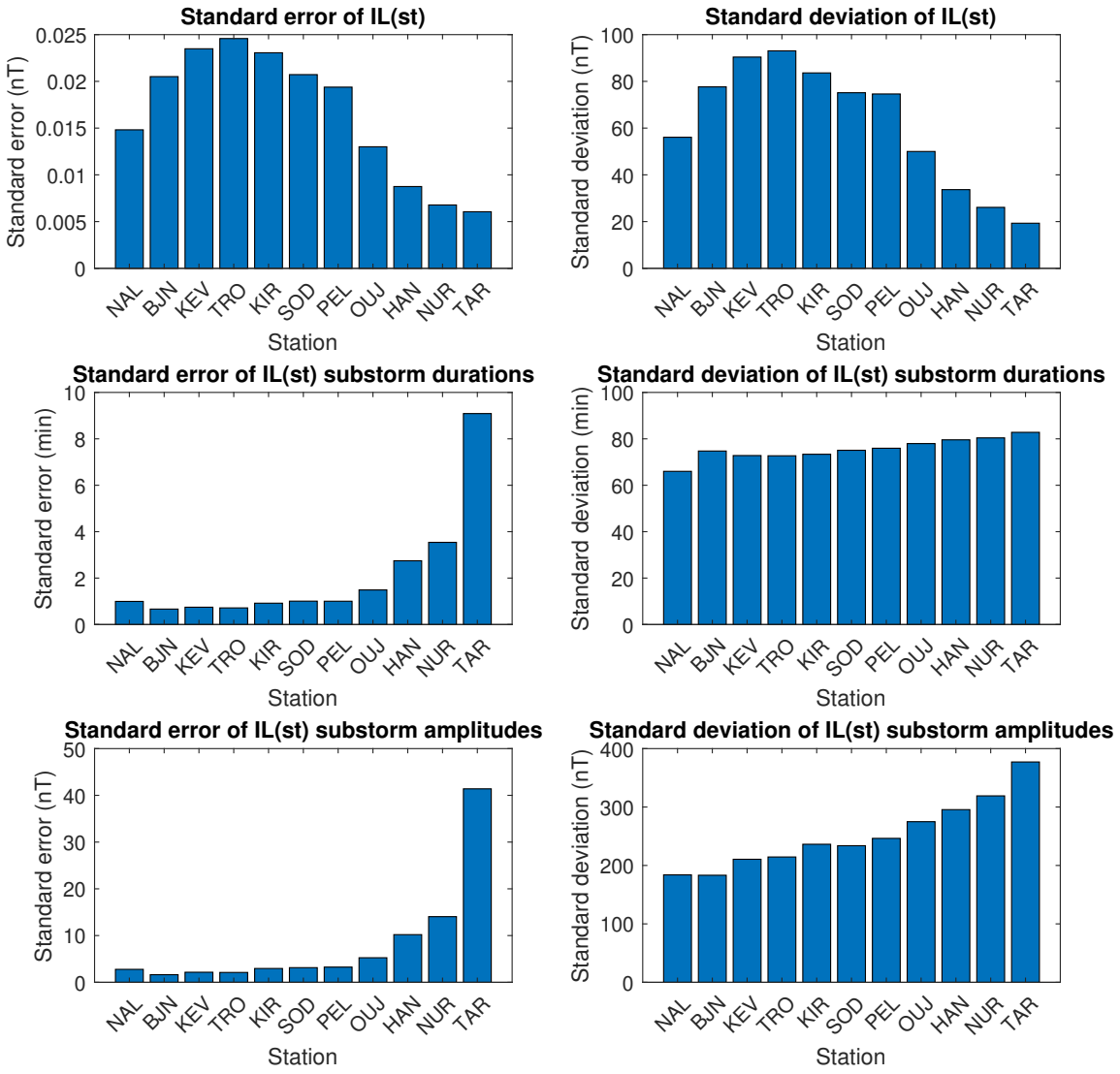

Figure 40: Left panel: Standard errors of the $IL(st)$ indices, average duration of substorms from each $IL(st)$ index and average amplitude of substorms from each $IL(st)$ index. Right panel: Standard deviations of the $IL(st)$ indices, average duration of substorms from each $IL(st)$ index and average amplitude of substorms from each $IL(st)$ index.

370 nT, PEL 371 nT, OUJ 357 nT, HAN 351 nT, NUR 321 nT, TAR 377 nT. The amplitude averages increase from NAL to KIR. KIR, SOD and PEL have similar amplitudes. The amplitude averages decrease from PEL to NUR. TAR has the largest amplitude average.

The left panel of Figure 40 shows the standard error ($SE = \sigma/\sqrt{n}$, where σ is the standard deviation and n is the number of data points) of the $IL(st)$ indices, and the standard error of mean durations and amplitudes of substorms found from each $IL(st)$ index. The standard error measures the error of the mean value. The standard error is larger with smaller n, meaning that with smaller n the mean value

is not as well known. The standard error increases from NAL to TRO, maximizing in TRO, and then decreases from TRO to TAR. Both standard errors of $IL(st)$ substorm amplitudes and durations increase rapidly with decreasing latitude from PEL to TAR.

The right panel of Figure 40 shows the standard deviation of the $IL(st)$ indices, and the standard deviation of mean durations and amplitudes of substorms found from each $IL(st)$ index. The standard deviation of the $IL(st)$ indices are similar to the standard errors of $IL(st)$ indices. However, the standard deviation of the $IL(st)$ substorm durations and amplitudes increase more linearly towards TAR, than the corresponding standard errors. The standard deviations of the $IL(st)$ subsorm amplitudes increase more than standard deviations of the $IL(st)$ substorm durations. Meaning, that the substorm durations increase only a little, but the amplitude increases notably with decreasing latitude.

6.3.1 Superposed epoch curves

The average magnetic signature at a station during the 14246 substorms of the IL index was calculated by superposing the $IL(st)$ and the standardized $IL_S(st)$ indices 90 minutes before and 150 minutes after the substorm onset, and then averaging all superposed indices. This method is called the superposed epoch (SPE) analysis, and substorm onset is taken as the zero epoch time of the SPE analysis. SPE gives an averaged magnetic signature of the combined substorms.

Figure 41a shows the superposed $IL(st)$ indices, during all (14246) IL substorms. Latitudinal differences in SPE curves are clearly seen. NAL increases towards zero, experiences a small negative deviation at onset and then continues growing. This is experienced among all IL stations. BJN has the steepest decrease after onset, and third largest amplitude. Largest amplitude is seen in KEV and second largest in TRO. KIR, SOD, and PEL share similar signatures, and their steepness and amplitude decreases with decreasing latitude. OUJ shows the weakest negative deviation at substorm onset. HAN, NUR and TAR show a positive bay after onset that increases with decreasing latitude.

Correspondingly, Figure 41b shows the superposed $IL_S(st)$ indices, during all IL substorms. Since a significant amount of onsets are from the BJN station (Figure 39), BJN is relatively most often disturbed at onset times and before onset. The amplitude of the relative negative deviations and their steepness decreases with decreasing latitude, so that KEV is second most disturbed and TRO is third most disturbed. KIR and SOD share more similar signatures than in Figure 41a. OUJ is the last station experiencing negative disturbances after substorm onset. The positive bays of HAN, NUR and TAR are seen clearer in the standardized scale. Two current systems are known to create positive bays during substorms: the eastward electrojet and the SCW (Section 4.1). The eastward electrojet creates larger positive bays at auroral latitudes. Thus, for the HAN, NUR and TAR stations, the main source for these positive bays is likely the SCW. The SCW is known to create positive bays at midlatitudes (McPher-

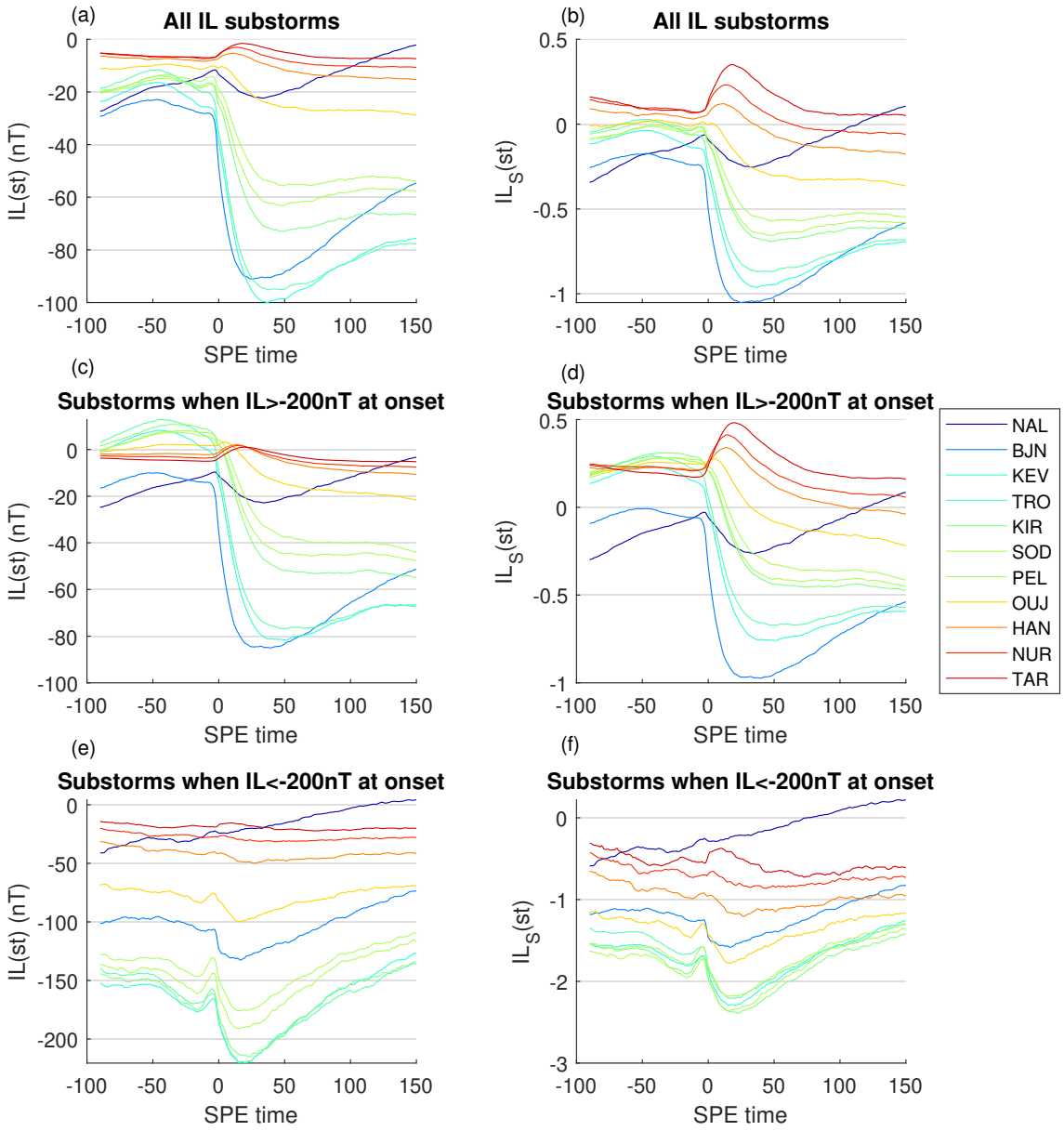

Figure 41: (**a**) Superposed epoch (SPE) curves of $IL(st)$ indices of each subset station, with the zero epoch time as the substorm onset (of all 14246 IL substorms). (**b**) Correspondingly, SPE curves of $IL_S(st)$ indices. (**c**) SPE curves of $IL(st)$ indices for substorms when IL index was larger than -200 nT at onset. (**d**) Correspondingly, SPE curves of $IL_S(st)$ indices. (**e**) SPE curves of $IL(st)$ indices for substorms when IL was smaller than -200 nT at onset. (**f**) Correspondingly, SPE curves of $IL_S(st)$ indices.

ron & Chu, 2017, 2018), due to the magnetic fields associated with both downward and upward FACs disturbing a station between the R1 and R2-sense FACs of the SCW.

Figure 41c shows the superposed $IL(st)$ indices during weak and moderate substorms, when the IL index was above (weaker than) $-200\,\mathrm{nT}$ at onset. Compared to Figure 41a, BJN has the steepest negative bay with largest amplitude. KEV and TRO have the second and third largest amplitudes. $IL(st)$ indices from KEV to OUJ are positive during the growth phase. On the other hand HAN, NUR and TAR are slightly negative before the onset, but increase towards and slightly above zero at onset. Figure 41d shows the superposed $IL_S(st)$ indices during substorms, when the IL index was above $-200\,\mathrm{nT}$ at onset. The result is similar to Figure 41b, stations from KEV to OUJ are positive before onset, and keep decreasing after onset. HAN, NUR and TAR are positive as well before onset and show positive bays that increase in amplitude with decreasing latitude.

Figure 41e shows the superposed $IL(st)$ indices during substorms, when the IL index was below (stronger than) $-200\,\mathrm{nT}$ at onset. All $IL(st)$ indices are negative the whole time, except NAL in the end. NAL increases during the whole substorm time and does not show a negative bay. BJN is roughly at $-100\,\mathrm{nT}$, above stations from KEV to PEL. KEV, TRO and KIR are roughly at $-150\,\mathrm{nT}$ before onset and they have the largest amplitude. Stations from KEV to OUJ show a small decrease and a notable increase right before onset. HAN and NUR show a very small decrease at onset. TAR shows a very small increase at onset. Figure 41f shows the superposed $IL_S(st)$ indices during corresponding strong substorms. Stations from KEV to PEL show similar magnetic signatures. HAN, NUR and TAR show a small positive and negative bay. Figures 41e and 41f show that an already enhanced westward electrojet ($IL < -200\,\mathrm{nT}$ at onset) is located in lower latitudes. This also shows that the westward electrojet at lower latitudes affects the positive bays at stations HAN, NUR and TAR. Positive bays can be seen more clearly, if the westward electrojet is not enhanced ($IL > -200\,\mathrm{nT}$) prior to the onset and is located at higher latitudes.

Figure 42 shows the standard errors of the superposed $IL(st)$ indices. The zero epoch time was the onset of all IL substorms. The standard errors were calculated for each superposed time for each SPE minute separately. All standard errors are small in nT. All standard errors decrease at onset, but increase after the onset. Thus, the $IL(st)$ values are more similar at the onset than before and after, and the variability of the superposed $IL(st)$ values increases after the substorm onset.

Figures 43 and 44 show the superposed $IL(st)$ indices during all IL substorms in different universal time (UT) hours (16-03 UT). NAL shows the largest negative bay, when the IL onset time was 16 UT hour. The negative bays decrease in amplitude with increasing UT hour, and the NAL sees no negative bay during UT hours 21-01 (23-03 LT). This indicates that on average, the westward electrojet affects the NAL station most at the evening sector 16-19 UT (18-21 LT). BJN shows a large negative bay when the onset is at UT hours 16-18 (18-20 LT). The negative bays move to later SPE time and back. This might be due to westward electrojet enhancing the most

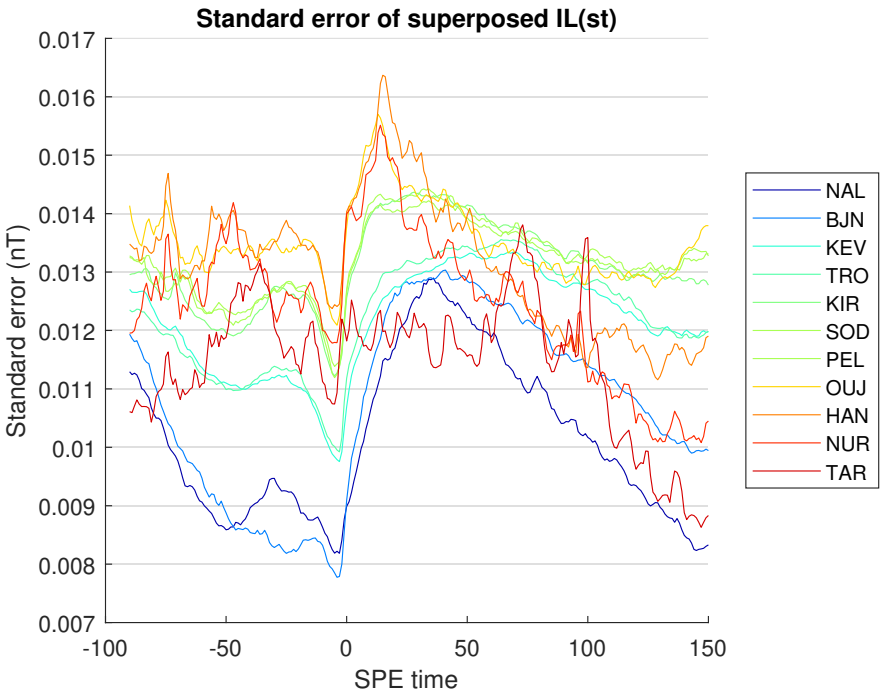

Figure 42: Standard errors of the superposed $IL(st)$ indices in each SPE minute separately, during all IL substorms.

under the connection area of the FAC (e.g., Figure 16), and flowing above the eastward electrojet at BJN UT hours 16-18. Start level of KEV decreases systematically between 16-00 UT (18-02 LT). The start level increases between 02-03 UT (04-05 LT). Also, the negative bays decrease in amplitude in UT hours 01-03. This indicates that the westward electrojet affects KEV most between UT hours 23-01. TRO shows similar magnetic signatures as KEV. KIR shows a small increase at onset in UT hours 16-18 (18-20 LT) that decreases in amplitude with increasing UT hour. Otherwise the magnetic signatures are similar to KEV and TRO. Indices from SOD to HAN show similar signatures as KIR as well, but the positive bay at 16-21 UT (18-23 LT) increases with decreasing latitude. Also the positive bay can be seen in later UT hours (18-23) at lower latitudes (from OUJ to TAR). Note that the scale of the y-axis changes, thus UT hours show relatively larger increases at onset. A small increase is seen in NUR UT hours 22-23 (00-01 LT). Also, a small decrease is seen in UT hours 00-03 (02-05 LT). TAR shows clear positive bays in UT hours 16-23 (18-01 LT). UT hours 18 and 20 (20 and 22 LT) show the largest amplitudes, and UT hour 19 (21 LT) the third largest. UT hours 00-03 (02-05 LT) do not show clear bays.

Figures 43 and 44 show that stations below KIR are affected by the eastward electrojet in the evening sector. This positive bay signal is not to be confused with the SCW positive bay signal. The SCW positive bays are seen in NUR and mostly in TAR. The separation of eastward electrojet and the SCW positive bays is difficult at the latitudes of the IMAGE stations. For example, the positive bay in UT hour 16 in

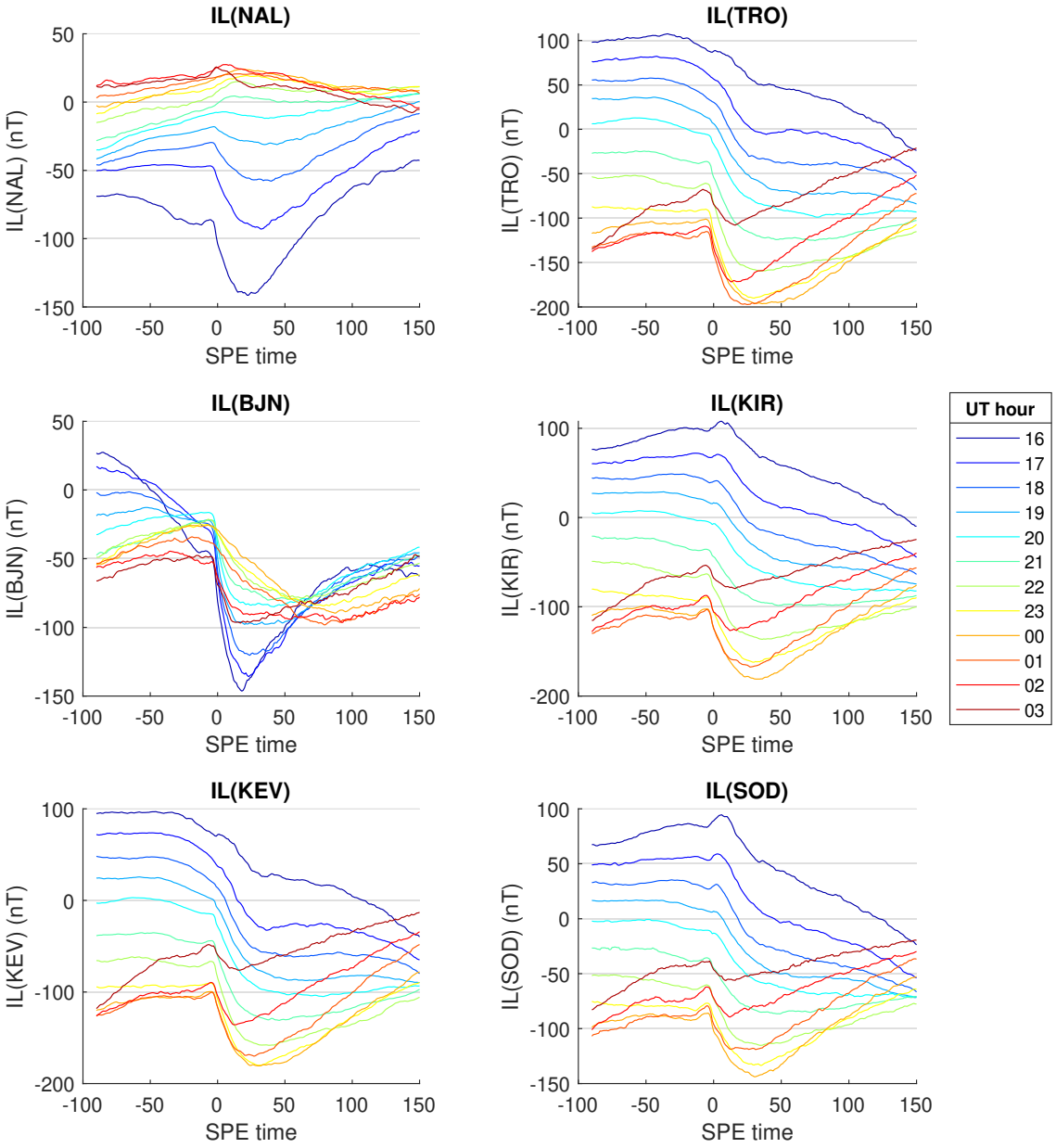

Figure 43: Superposed epoch curves of NAL, BJN, KEV, TRO, KIR, SOD, OUJ $IL(st)$ indices. Zero epoch time is the substorm onset delimited to universal time (UT) hours. Color indicates the UT hour of the substorm onset (16 to 03 UT).

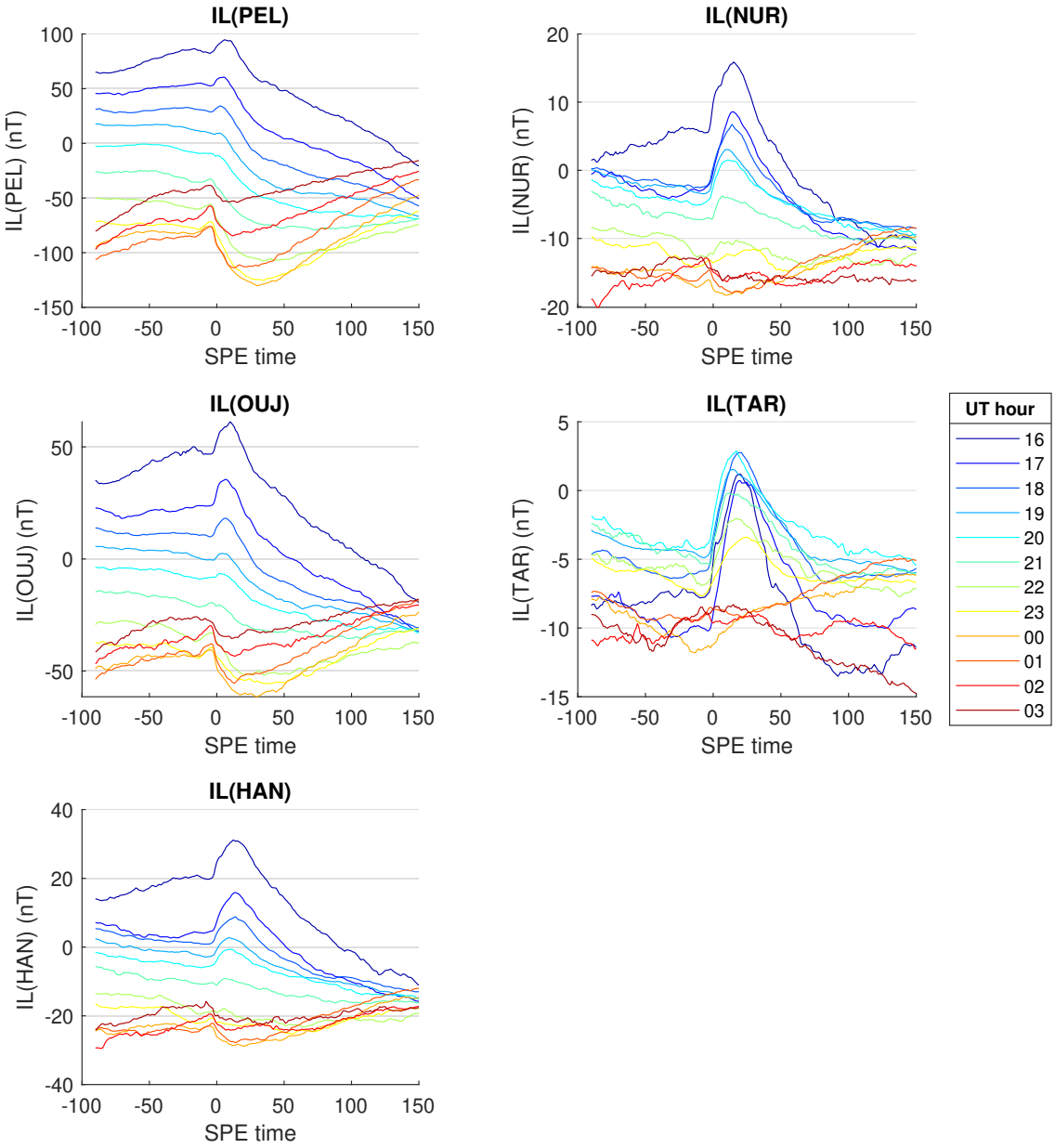

Figure 44: Superposed epoch curves of PEL, OUJ, HAN, NUR and TAR $IL(st)$ indices. Zero epoch time is the substorm onset delimited to universal time (UT) hours. Color indicates the UT hour of the substorm onset (16 to 03 UT).

NUR is most likely from the eastward electrojet from higher latitudes. However, the SCW could contribute to the positive bay in UT hours 19-20. The same applies for the TAR. However, the positive bays in TAR can be more safely assumed to origin from the SCW, since the largest deviations (positive bays) locate around the midnight sector.

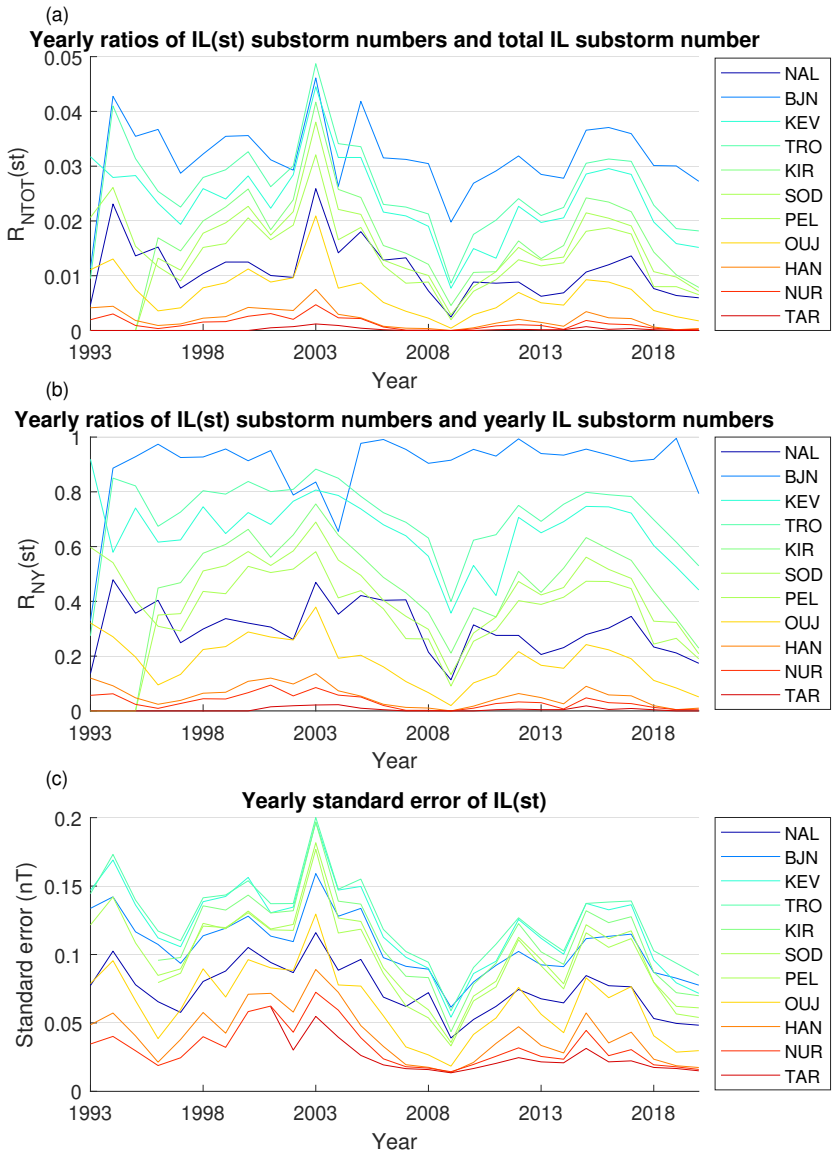

Figure 45: (**a**) Yearly ratios of $IL(st)$ substorm numbers and the total IL substorm number (14246). Color changes from cold to warm, as an indication of the station latitudes. (**b**) Correspondingly, yearly ratios of $IL(st)$ substorm numbers and yearly IL substorm numbers. (**c**) Yearly standard error of $IL(st)$ indices.

6.3.2 Solar cycle variation of different latitudes

The yearly ratio (notated as $R_{NTOT}(st)$) of the $IL(st)$ substorm number and the total IL substorm number (14246) for each station is seen in Figure 45a. $R_{NTOT}(st)$ ratios decrease in latitude from BJN to TAR, except TRO has larger $R_{NTOT}(st)$ than KEV, which agrees with Figure 39a. Each station follows the solar cycle variation as the yearly substorm number (Figure 33). BJN has the largest $R_{NTOT}(st)$ in all years, except in 2003. In 2003, more substorms are detected at KEV, TRO and KIR. Figure 45b shows the yearly ratio (notated as $R_{NY}(st)$) of $IL(st)$ substorm numbers and the

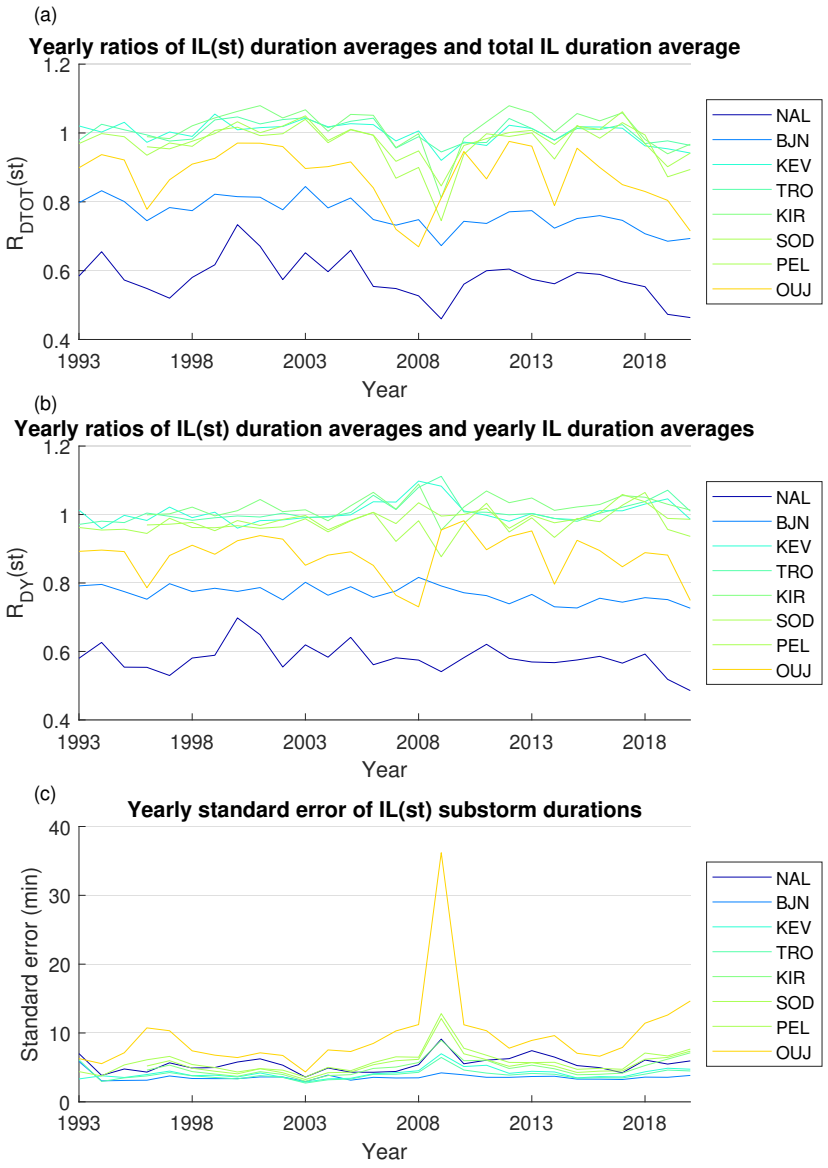

Figure 46: (**a**) Yearly ratios of $IL(st)$ substorm duration averages and the total IL substorm duration average (3 h and 1 min). Color changes from cold to warm, as an indication of the station latitudes. (**b**) Correspondingly, yearly ratios of $IL(st)$ substorm duration averages and yearly IL substorm duration averages. (**c**) Yearly standard error of substorm durations of $IL(st)$ substorms.

yearly IL substorm numbers (see Figure 33). BJN has larger than 0.9 $R_{NY}(st)$ in all years except 2002-2004 and 2020. Year 1993 was the start year of BJN and the years 2002-2004 coincide with the years of high data gap percentages in BJN (Figure 28). The yearly $R_{NY}(st)$ from KEV to TAR (and NAL) follow the solar cycle variation, indicating that in years with a high IL substorm number, relatively more substorms are detected in lower latitudes as well. Figure 45c shows the yearly standard error of $IL(st)$ indices (see also Figure 40a). Standard errors also follow the solar cycle

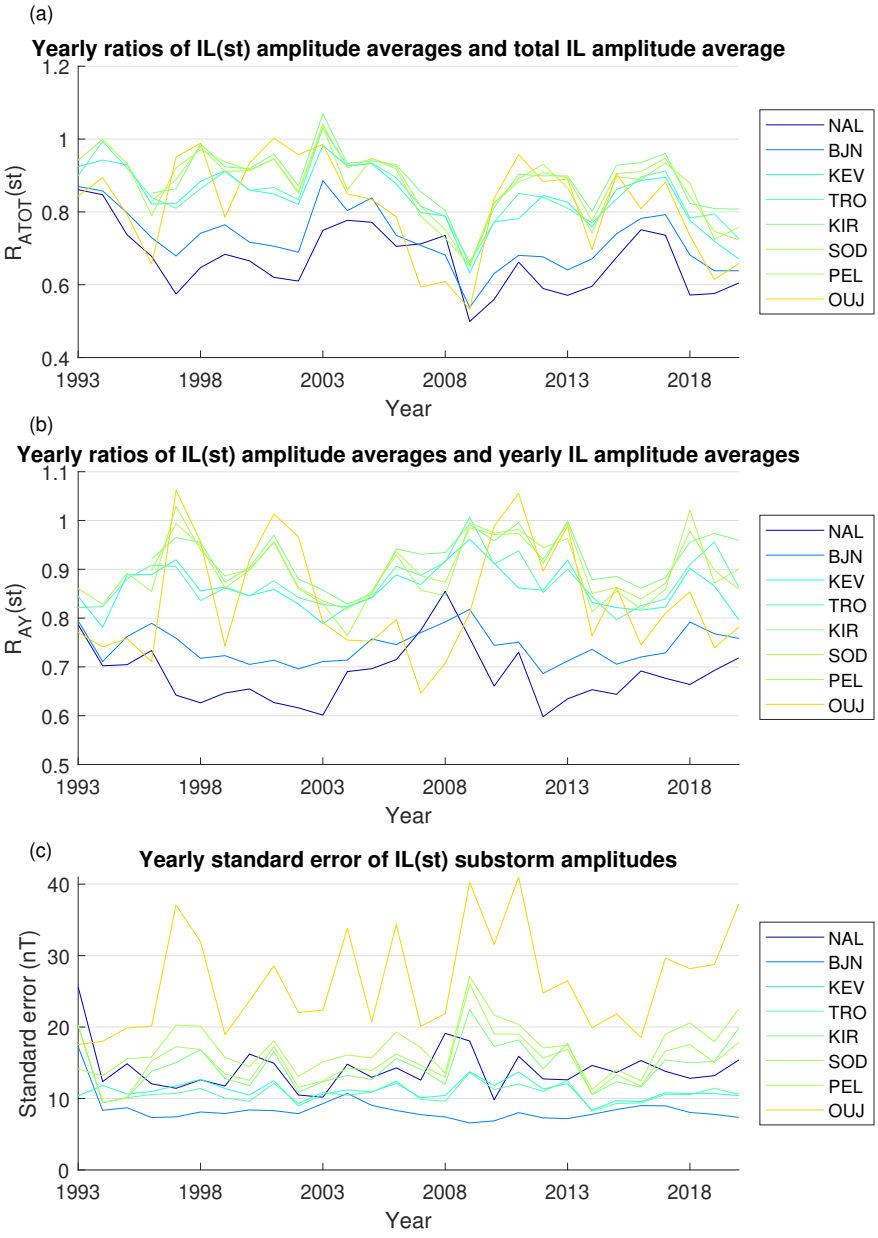

Figure 47: (**a**) Yearly ratios of $IL(st)$ substorm amplitude averages and the total IL substorm amplitude average (411 nT). (**b**) Correspondingly, yearly ratios of $IL(st)$ substorm amplitude averages and yearly IL substorm amplitude averages. (**c**) Yearly standard error of substorm amplitudes of $IL(st)$ substorms.

variation of the substorm number.

Figure 46a shows the yearly ratios (notated as $R_{DTOT}(st)$) of $IL(st)$ substorm duration averages and the total duration average of IL substorms (3 h and 1 min). Stations HAN, NUR and TAR are left out since they do not have enough of substorms to construct a robust duration average (see also Figure 40b). NAL and BJN substorms are consistently shorter in duration, with NAL having the smallest, and BJN having the

second smallest $R_{DTOT}(st)$. On average, the longest substorms occur in stations from KEV to PEL. OUJ has the third smallest $R_{DTOT}(st)$. NAL and OUJ shows solar cycle variation more clearly. Other stations variate, but show less of solar cycle variation. Stations from NAL to TRO decrease slightly in 2009. All stations decrease in 2009. OUJ decreases in 2008. However, OUJ durations are not robust in years 2008-2010 due to low number of substorms (see Figure 45). Figure 46b shows similar results as Figure 46a, for yearly ratios (notated as $R_{DY}(st)$) of $IL(st)$ substorm duration averages and yearly IL substorm duration averages (see Figure 34). KEV and TRO $R_{DY}(st)$ increase in 2009, and the decrease in KIR, SOD and PEL is not as large (~ 0.05 smaller than in Figure 46a). Figure 46c shows the yearly standard error of $IL(st)$ substorm durations. Stations have an yearly standard error of roughly 5 min. Yearly standard error increases in 2009 in all stations except BJN. OUJ station has the largest yearly standard errors, and peaks roughly 25 min in year 2009. This peak is explained by Figure 45, which shows that the IL(OUJ) substorm number was very low in year 2009, meaning that the duration average is not robust. The smaller number of substorms in 2009 affects the standard errors of other stations as well.

Figure 47a shows the yearly ratios (notated as $R_{ATOT}(st)$) of $IL(st)$ amplitude averages and the total amplitude average of IL substorms (411 nT). Stations HAN, NUR and TAR are left out since they do not have enough of substorms to construct a robust amplitude average. All stations show the same solar cycle variation. NAL and BJN have the smallest $R_{ATOT}(st)$. KEV and TRO have slightly smaller $R_{ATOT}(st)$ than KIR to PEL. Stations from KIR to PEL have largest $R_{ATOT}(st)$. OUJ variation differs from stations KEV to PEL, due to low number of substorms found from the IL(OUJ) index. All $R_{ATOT}(st)$ decrease in 2009. Figure 47b shows the yearly ratios (notated as $R_{AY}(st)$) of $IL(st)$ amplitude averages of the yearly amplitude averages of IL substorms (see Figure 35). NAL and BJN have the lowest $R_{AY}(st)$ (except in 2007). R_{AY}(NAL) increases in 2008 and R_{AY}(BJN) increases in 2009. KEV and TRO have slightly smaller $R_{AY}(st)$ than stations from KIR to PEL. Stations from KIR to PEL have often the largest $R_{AY}(st)$. Solar cycle variation of the $R_{AY}(st)$ in stations from KEV to PEL is the decrease in 2003 and the increase in 2009 and 2018. However, R_{AY}(OUJ) increases most in some years. Similarly as in Figure 47b the strong variations are due to the low number of substorms found from the IL(OUJ) index. Figure 47c shows the yearly standard error of $IL(st)$ substorm amplitudes. NAL has yearly standard errors increase in 2008. BJN has the lowest yearly standard errors below 10 nT (NAL and BJN start date is October 1993, thus standard errors are high in 1993). KEV and TRO standard errors are roughly 10 nT. The standard errors for the stations from KIR to PEL increase considerably more in 2009 than in other years. This is mostly due to the low substorm number in year 2009, because the standard error is much smaller during other years with similar $R_{AY}(st)$ value (e.g., in years 1997, 2013 and 2018). Standard error of OUJ variate strongly between 20-40 nT, due to low number of substorms found from the IL(OUJ) index.

The latitudinal distribution of substorm properties in Figures 45-47 follow Fig-

ure 39. $R_{NTOT}(st)$ and $R_{ATOT}(st)$ follow the same solar cycle variation. However, $R_{DTOT}(st)$ shows only weak solar cycle variation. The decrease of duration in 2009 in Figures 46a and Figure 46b coincide with the decrease of all $IL(st)$ substorm numbers in Figure 45a (see also Figure 33), which is due to the solar cycle variation. The decrease of the $R_{DTOT}(st)$ of stations KIR, SOD and PEL to 0.75-0.85 in year 2009, shows that during such low substorm number, substorms are considerably shorter in stations KIR, SOD and PEL. The increases of $R_{AY}(st)$ show that the stations from KIR to PEL correspond to the yearly IL substorm amplitudes.

6.3.3 Seasonal variation of different latitudes

Figure 48a shows seasonal variation of $R_{NTOT}(st)$. All station $R_{NTOT}(st)$, except R_{NTOT}(NAL) increase in months 3 and 10 (close to equinoxes), and have a global minimum in month 6. NAL and BJN have a local maximum differ from the rest of the stations in that they have the global maximum in winter.

Figure 48b shows seasonal ratio (notated as $R_{NM}(st)$) of $IL(st)$ substorm numbers and seasonal IL substorm numbers (see Figure 37a). R_{NM}(NAL) is smaller than 0.4, and has a semiannual variation with a summer minimum. R_{NM}(BJN) varies between 0.8-0.9. BJN has a minimum in April and maximum in October. This shows that BJN has relatively more substorms around fall than spring. KEV and TRO have $R_{NM}(st)$ between 0.6-0.8, while KIR, SOD and PEL $R_{NM}(st)$ vary between 0.3-0.5. R_{NM}(OUJ) varies between 0.1-0.3 and HAN, NUR and TAR $R_{NM}(st)$ are smaller than 0.1. Note that all stations below KEV have a dominant semiannual variation, in difference to Figure 48a

Figure 48c shows seasonal variation of the standard error of the $IL(st)$ indices. All standard errors are smaller than 0.1 nT. IL(NAL) standard error has a notable annual variation with maximum in month 6, and minimum in month 12. IL(BJN) standard errors depict hardly any seasonal variation. IL(KEV) and IL(TRO) have the largest standard errors. All stations from TRO to NUR depict a mixture of annual and semiannual variation with maxima in month 4 and 9 and 10, and global minimum in winter. Note that the fall maximum is larger than the spring maximum, and thus asymmetry increases toward lower latitudes. TAR has no local maximum in spring, only global maximum in October.

Since the seasonal variation of the NAL and BJN substorm numbers differs greatly from the rest of the stations with their large annual variation with maxima in winter months, this aspect is studied further. Figure 49a shows the standardized seasonal variation of the $IL(st)$ substorm numbers. Seasonal substorm numbers from IL(TAR) are included, even though TAR has a very small substorm number. The standardization of the seasonal substorm numbers (for each station) was done with Equation (4.9), by replacing the IL in the equation with the seasonal substorm numbers. The standardization shows the similarity of the seasonal variations from KEV to NUR. Figure 49b shows the correlation coefficients and p-values of the correlation between NAL

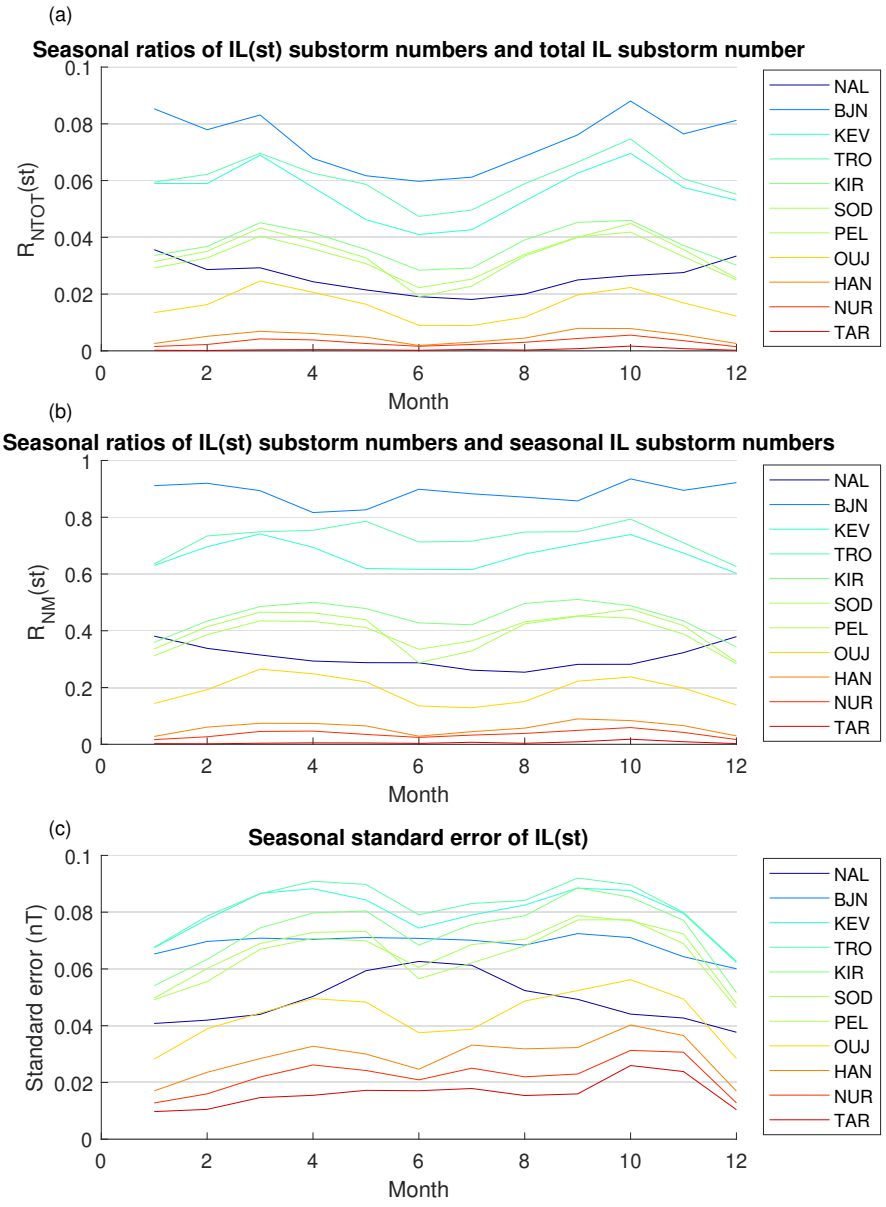

Figure 48: (**a**) Seasonal ratios of $IL(st)$ substorm numbers and total IL substorm number (14246). Color changes from cold to warm, as an indication of the station latitudes. (**b**) Correspondingly, seasonal ratios of $IL(st)$ substorm numbers and seasonal IL substorm numbers. (**c**) Seasonal standard error of $IL(st)$ indices.

and all other stations. NAL and BJN seasonal variations correlate quite strongly with each other, and NAL and KEV correlate marginally. With all other stations, NAL shows no correlation. Figure 49c shows the correlation coefficients and p-values of the correlation between BJN and all other stations. Overall, BJN correlates somewhat better with the other stations than NAL. BJN correlates quite strongly with NAL and KEV and marginally with TRO and PEL. BJN does not correlate significantly (95% confidence interval) with other stations. The correlation results in Figures 49b and

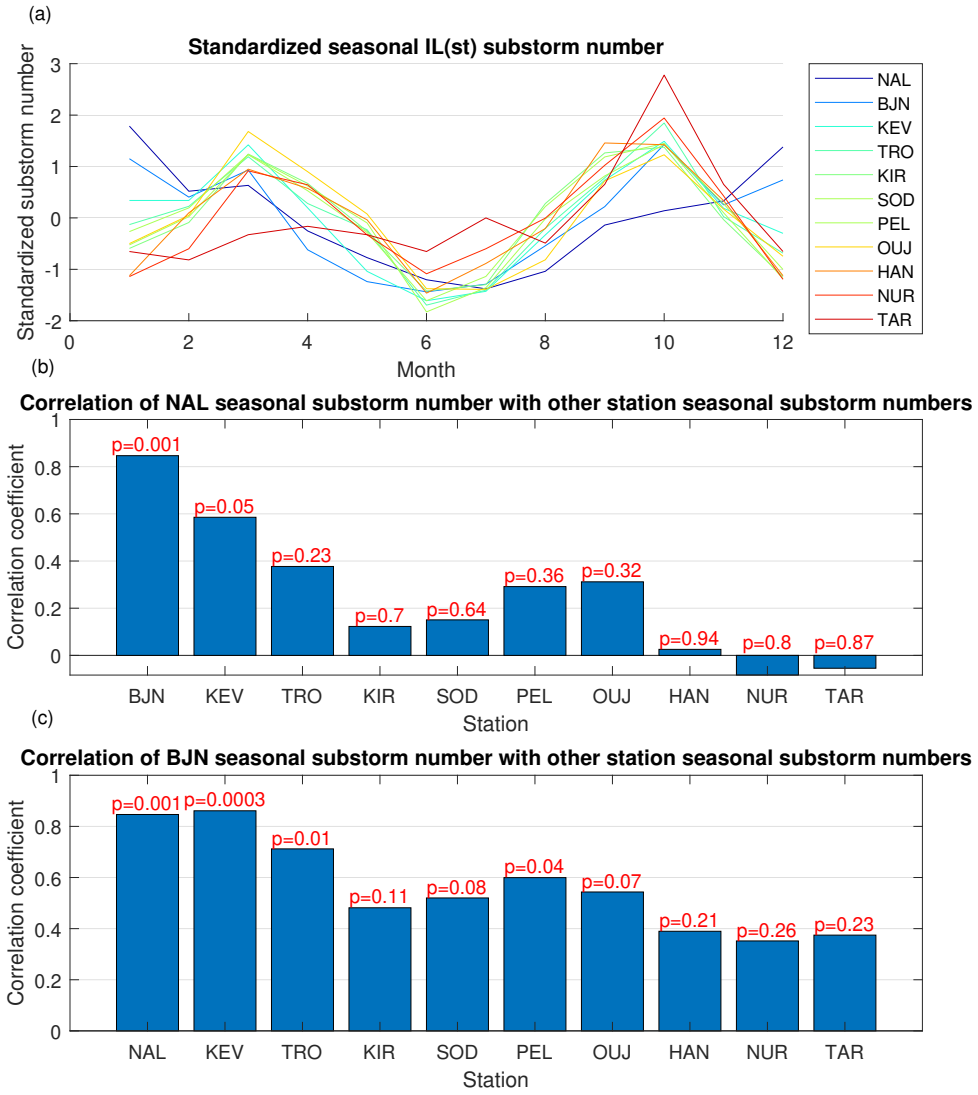

Figure 49: (**a**) Standardized seasonal substorm numbers from $IL(st)$ indices. (**b**) Correlation coefficients of the correlation between NAL seasonal substorm number and seasonal substorm numbers of other stations. P-value of the correlation is on top of each bar. (**c**) Correspondingly, correlation coefficients of the correlation between BJN seasonal substorm number and seasonal substorm numbers of other stations. P-value of the correlation is on top of each bar.

49c show how seasonal variation changes with decreasing latitude.

Figure 50a shows seasonal variation of the $R_{DTOT(st)}$ IL(st). NAL and BJN show a weak annual variation with maximum in month 6. Stations from KEV to OUJ share a similar seasonal variation of duration and depict a strong annual variation with maximum in month 5, and minimum in winter (months 1 and 12). Figure 50b shows seasonal ratio (notated as $R_{DM}(st)$) of $IL(st)$ substorm duration averages and seasonal IL substorm duration averages (see Figure 37b). NAL and BJN durations has now also an semiannual component with a seasonal maximum in winter. Annual

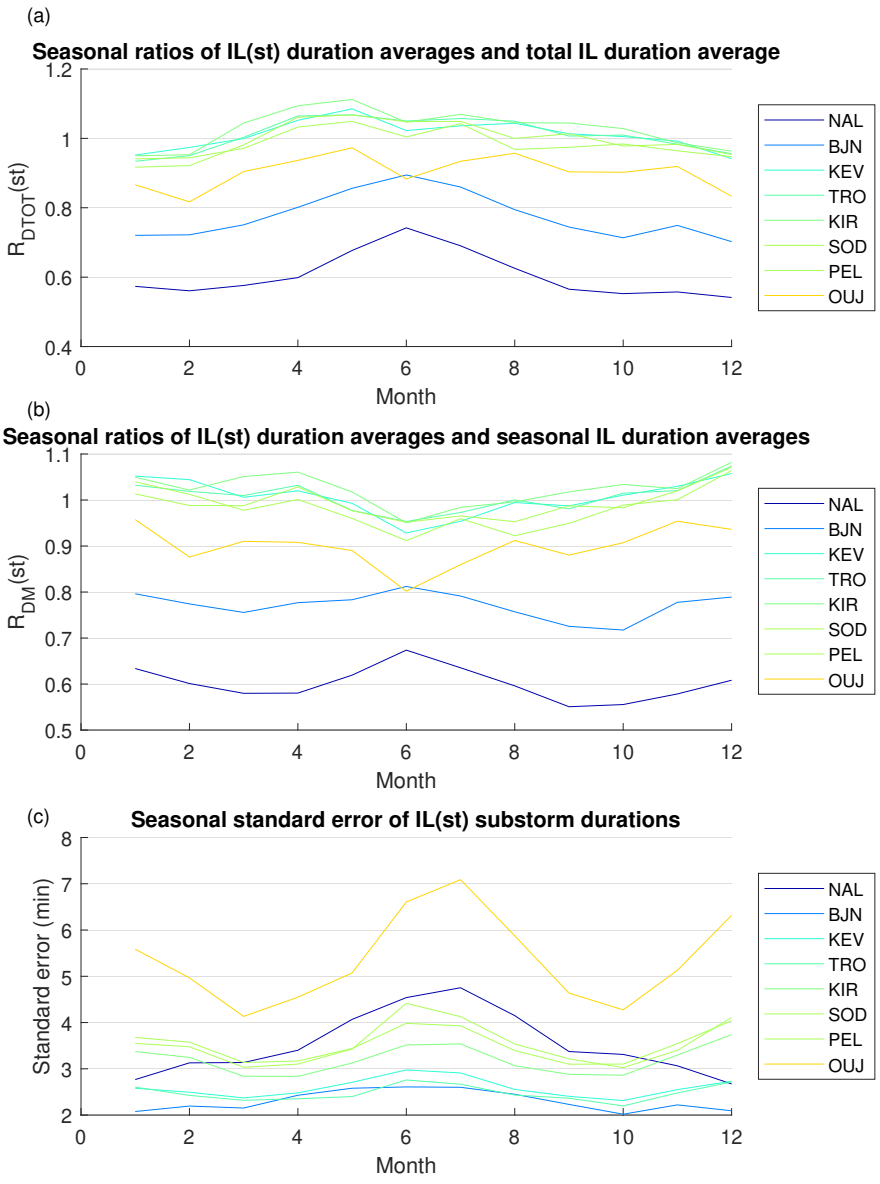

Figure 50: (**a**) Seasonal ratios of $IL(st)$ duration averages and total IL duration average (3 h and 1 min). Color changes from cold to warm, as an indication of the station latitudes. (**b**) Correspondingly, seasonal ratios of $IL(st)$ duration averages and seasonal IL duration average. (**c**) Seasonal standard error of substorm durations of $IL(st)$ substorms.

variation with winter maximum now dominates all other stations, and the seasonal maximum is now found in April. Figure 50c shows the seasonal standard error of the $IL(st)$ substorm durations. Seasonal standard errors are smaller than 5 min in all station except for OUJ. All station depict a dominant annual variation with summer maximum and some semiannual variation with secondary maximum in winter.

Figure 51 shows the standardized seasonal variation of the $IL(st)$ substorm duration averages. NAL and BJN has a strong annual variation with a maximum in summer

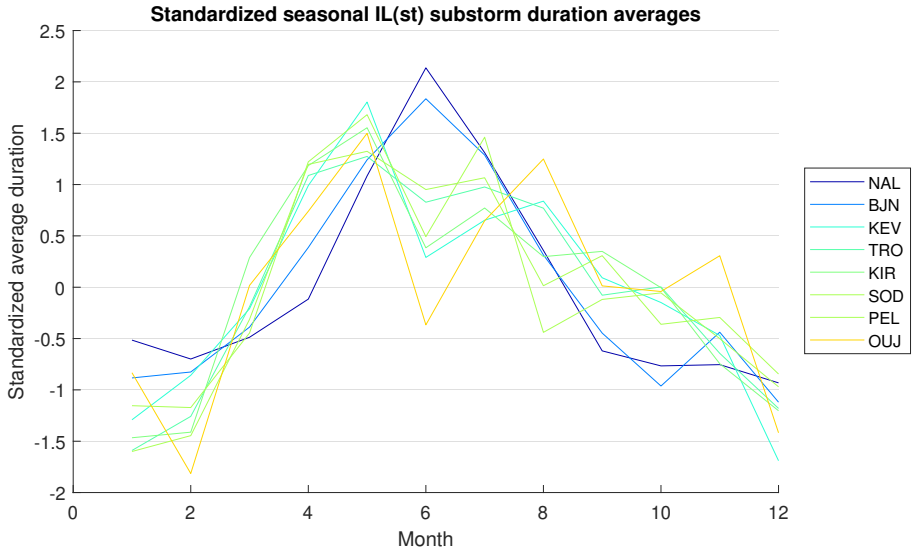

Figure 51: Standardized seasonal substorm duration averages from $IL(st)$ indices.

and minimum in winter. All other stations show annual variation with maximum in May and minimum in winter.

Figure 52a shows seasonal variation of $R_{ATOT}(st)$. NAL and BJN depict a dominant annual variation with minimum in June and a subdominant semiannual variation with maximum in months 2, 3 and 10 and second minimum in months 11 and 12. All other stations have almost an opposite seasonal variation, with a dominant semiannual variation with maximum in months 3, 5 and 8 and global minimum in winter (months 1 and 12). Note also that the fall maximum is systematically larger than the spring max.

Figure 52b shows seasonal ratio ($R_{AM}(st)$) of the $IL(st)$ substorm duration averages and seasonal IL duration averages (see Figure 37c). NAL and BJN depict dominant annual variation with a summer minimum and maximum in winter (months 1 and 12). All other stations show dominant annual variation with maximum in July and minimum in January, except OUJ has maximum in August.

Figure 52c shows the seasonal standard error of the $IL(st)$ substorm durations. Seasonal standard errors of stations NAL to PEL remain below 15%. NAL and BJN show weak annual variation with small semiannual component with maximum in October and second maximum in March, and minimum in June. Stations from KEV to PEL show weak semiannual component, almost opposite to NAL and BJN. OUJ standard errors are twice larger than the rest of the stations.

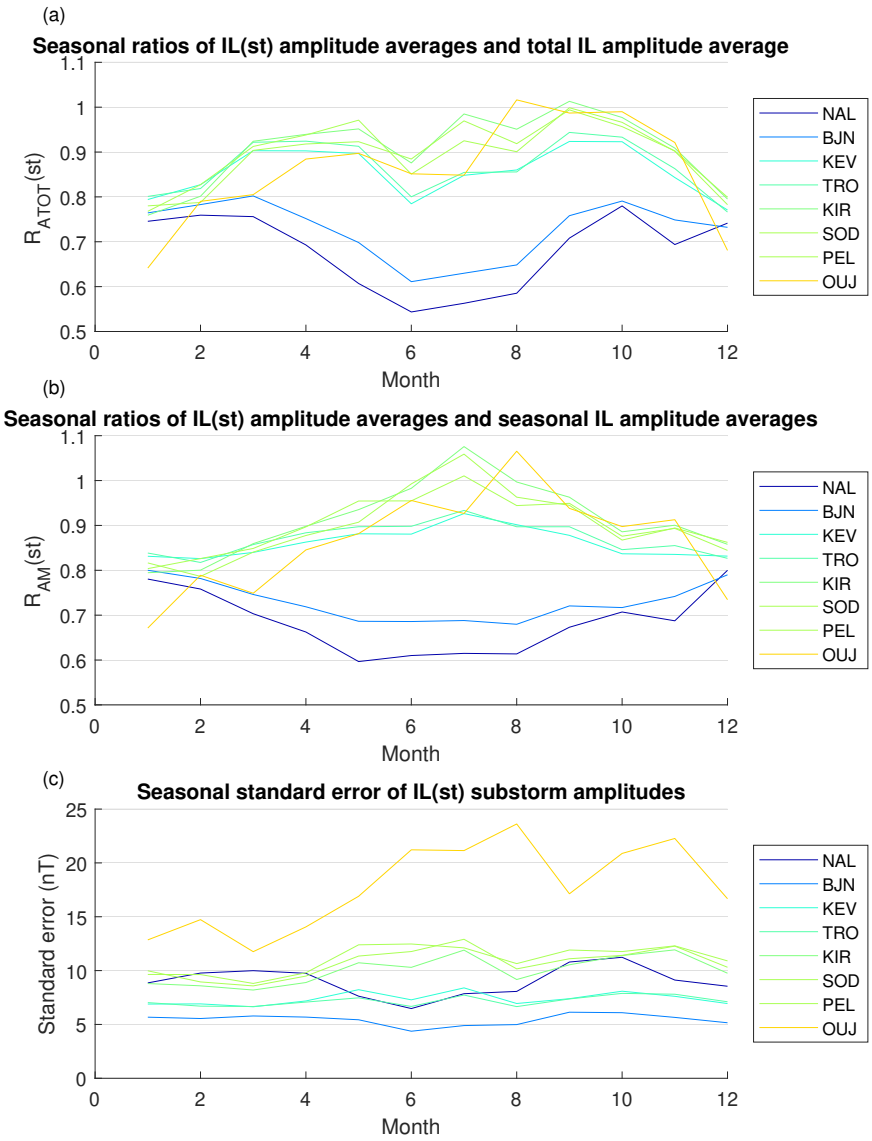

Figure 52: (**a**) Seasonal ratios of $IL(st)$ amplitude averages and total IL amplitude average (411 nT). Color changes from cold to warm, as an indication of the station latitudes. (**b**) Correspondingly, seasonal ratios of $IL(st)$ amplitude averages and seasonal IL amplitude averages. (**c**) Seasonal standard error of substorm amplitudes of $IL(st)$ substorms.

7 Conclusions

The solar cycle variation of the IL substorm number, duration and amplitude was studied as yearly averages (Figures 33-35). HSS were found to be the main driver for the substorm occurrence on a yearly scale. This was in agreement with the results of Tanskanen (2009). However, the mean substorm durations were found to correlate better with the IMF intensity and with CMEs, and the mean substorm amplitudes

were found to correlate better with the solar wind speed and with HSS.

The latitudinal distribution of substorms was studied using a subset of eleven IMAGE stations. This distribution showed that majority of substorms were detected in BJN station. Also a large amount of substorms were detected by KEV and TRO stations. This showed that majority of the substorm onsets in the IL substorm list (14246 onsets) are from stations from similar latitudes as BJN (74.50° N), KEV (69.76° N) and TRO (69.66° N). This gave insights of what stations contribute most often to the substorm list by Tanskanen (2009).

I studied the latitudinal distribution of the average magnetic signatures using superposed epoch (SPE) analysis. In the case of all IL substorms, the amplitude of the negative bays were found to be largest at KEV, TRO and BJN stations (in that order), and the negative bay amplitudes of the stations below TRO decreased with decreasing latitude. The magnetic signatures showed a positive bay at onset at stations HAN (62.25° N), NUR (60.505° N) and TAR (58.26° N). The same SPE analysis of the standardized $IL_S(st)$ indices showed that the amplitude of these positive bays increased with decreasing latitude. This implied that the main source for these positive bays was likely field-aligned currents associated with the SCW (McPherron & Chu, 2017, 2018).

The SPE analysis also showed that when the IL index was above -200 nT at onset, the amplitude of the negative bays were found to be largest at BJN, KEV and TRO. Otherwise, the magnetic signatures showed similar behaviour as in the case of all IL substorms. However, when the IL index was below -200 nT at onset (already enhanced westward electrojet), the amplitude of the negative bays were largest at stations KEV, TRO and KIR (latitudinal range of 69.76° N - 67.84° N). However, the BJN station (74.50° N) showed a weaker negative bay and NAL, the northernmost station (78.92° N) did not show a negative bay at all. Also the positive bays in HAN, NUR and TAR were less distinct. This showed that the westward electrojet descends and affects the stations at lower latitudes if it is already enhanced prior to the onset.

The SPE analysis was also done for substorm onsets at different UT hours (Figures 43 and 44). This showed how the eastward and westward electrojets affect the stations at different UT hours at the substorm onset. The distinction between the two possible sources of positive bays (eastward electrojet and the SCW) was found to be difficult even in TAR, which should be the best station of the subset to measure the positive bay signal from field-aligned currents of the SCW, as the southernmost station of the subset.

The solar cycle variation of substorm occurrence at different latitudes was studied (Figures 45). The solar cycle variation of yearly substorm numbers were roughly similar for all stations. However, subauroral stations from KEV to OUJ showed relatively stronger solar cycle variation than the polar cap stations NAL and BJN. Substorm durations showed only weak solar cycle variation for all stations from NAL to OUJ (Figure 46). Solar cycle variation of substorm amplitudes was very similar for all stations outside the polar cap (Figure 47).

The seasonal variation of substorm properties of different latitudes was studied (Figures 48-52). I found that the polar cap stations NAL and BJN show dominant annual variation. However, other stations show semiannual variation, which increases in amplitude towards lower latitudes. Actually, the lowest latitude stations only exhibit semiannual variation, without any clear annual variation. The seasonal maximum of substorm occurrence observed by NAL and BJN stations occurs at the winter solstice. However, the seasonal maxima of lower latitudes occur around spring and fall equinoxes, due to strong semiannual variation. Since the majority of IL substorms were detected at BJN stations, the seasonal variation of the IL substorm number follows the seasonal variation (with strong winter-summer annual variation) of the BJN station. Some previous studied by Tanskanen (2009) showed spring-fall asymmetry in substorm occurrence. This asymmetry is seen only at BJN station, and it is actually seen to reverse at OUJ station. Thus, no systematic spring-fall asymmetry was found.

All stations showed annual variation of the substorm durations. NAL and BJN showed maximum durations in month 6, while other stations showed maximum durations in month 5. Thus, stations from KEV to OUJ differed slightly from the seasonal variation of the IL substorm durations. NAL and BJN showed dominant annual variation of the substorm amplitudes with maxima in winter and minima in summer. The other stations had almost an opposite annual variation. Also, the other stations showed strong semiannual variation.

References

Akasofu, S.-I. (1964). The development of the auroral substorm. *Planet. Space Sci.*, 12, 273–282.

Allen, J. V., Ludwig, G., Ray, E., & McIlwain, C. (1958). Observation of high intensity radiation by satellites 1958 alpha and gamma. *Journal of Jet Propulsion*, 28, 588––592.

Angelopoulos, V., Baumjohann, W., Kennel, C., Coroniti, F., Kivelson, M., Pellat, R., Walker, R., Lühr, H., & Paschmann, G. (1992). Bursty bulk flows in the inner central plasma sheet. *J. Geophys. Res.*, 97, 4027–4039.

Angelopoulos, V., McFadden, J. P., Larson, D., Carlson, C. W., Mende, S. B., Frey, H., Phan, T., Sibeck, D. G., Glassmeier, K.-H., Auster, U., Donovan, E., Mann, I. R., Rae, I. J., Russell, C. T., Runov, A., Zhou, X.-Z., & Kepko, L. (2008). Tail reconnection triggering substorm onset. *Science*, 321, 931–935.

Axford, W. & Hines, C. O. (1961). A unifying theory of high latitude geophysical phenomena and geomagnetic storms. *Can. J. Phys.*, 39, 1433–1464.

Axford, W., Petschek, H., & Siscoe, G. (1965). Tail of the magnetosphere. *J. Geophys. Res.*, 70, 1231–1236.

Baker, D., Pulkkinen, T., Angelopoulos, V., Baumjohann, W., & McPherron, R. (1996). Neutral line model of substorms: Past results and present view. *J. Geophys. Res.*, 101, 12975–13010.

Baker, D., Zwickil, R., Bame, S., E.W. Hones, J., Tsurutani, B., Smith, E., & Akasofu, S.-I. (1983). An isee 3 high time resolution study of interplanetary parameter correlations with magnetospheric activity. *J. Geophys. Res.*, 88, 6230–6242.

Balogh, A. & Erdõs, G. (2013). The heliospheric magnetic field. *Space. Sci. Rev.*, 176, 177–215.

Bame, S., Asbridge, J., Felthauser, I.-I., Hones, E., & Stron, I. (1967). Characteristics of the plasma sheet in the earth's magnetotail. *J. Geophys. Res.*, 72, 113–129.

Birn, J., Nakamura, R., Panov, E., & M.Hesse (2011). Bursty bulk flows and dipolarization in mhdsimulations of magnetotail reconnection. *J. Geophys. Res.*, 116, A01210.

Biskamp, D. (1996). Magnetic reconnection in plasmas. *Astrophys Space Sci*, 242, 165–207.

Brekke, A., Doupnik, J., & Banks, P. (1974). Incoherent scatter measurements of e region conductivities and currents in the auroral zone. *J. Geophys. Res.*, 79, 3773–3790.

Burlaga, L., Sittler, E., Mariani, F., & Schwenn, R. (1981). Magnetic loop behind an interplanetary shock: Voyager, helios, and imp 8 observations. *J. Geophys. Res.*, 86, 6673–6684.

Burton, R., McPherron, R., & Russell, C. (1975). An empirical relationship between interplanetary conditions and dst. *J. Geophys. Res.*, 80, 4204–4214.

Cahill, L. & Amazeen, P. (1963). The boundary of the geomagnetic field. *J. Geophys. Res.*, 68, 1835—-1843.

Carpenter, D. (1963). Whistler evidence of a knee' in the magnetospheric ionization density profile. *J. Geophys. Res.*, 68, 1675–1682.

Carpenter, D. (1966). Whistler studies of the plasmapause in the magnetosphere, 1: temporal variation in the position of the knee and some evidence on plasma motions near the knee. *J. Geophys. Res.*, 71, 693–709.

Chapman, S. & Ferraro, V. (1931). A new theory of magnetic storms. *Terrestrial Magnetism and Atmospheric Electricity*, 36, 77–97.

Christon, S., Mitchell, D., & Williams, D. (1988). Energy spectra of plasma sheet ions and electrons from 50 ev/e to 1 mev during plasma temperature transitions. *J. Geophys. Res.*, 93, 2562–2572.

Cliver, E., Kamide, Y., & Ling, A. (2000). Mountains versus valleys: Semiannual variation of geomagnetic activity. *J. Geophys. Res.*, 105, 2413–2424.

Cowley, S. (2000). *Magnetosphere-ionosphere interactions: a tutorial review, in: Magnetospheric Current Systems, edited by: Ohtani, S.-I., Fujii, R., Hesse M., and Lysak, R. L.* American Geophysical Union, Washington, D. C., USA.

Cowley, S. & Lockwood, M. (1992). Excitation and decay of solar wind-driven flows in the magnetosphere-ionosphere system. *Ann. Geophys.*, 10, 103–115.

Coxon, J., Milan, S., Clausen, L., Anderson, B., & Korth, H. (2014). A superposed epoch analysis of the regions 1 and 2 birkeland currents observed by ampere during substorms. *J. Geophys. Res. Space Physics*, 119, 9834–9846.

Daglis, I., Thorne, R., Baumjohann, W., & Orsini, S. (1999). The terrestrial ring current: Origin, formation, and decay. *Rev. Geophys.*, 37, 407–438.

Davis, T. & Sugiura, M. (1966). Auroral electrojet activity index ae and its universal time variations. *J. Geophys. Res.*, 71, 785–801.

Dimmock, A. P., Rosenqvist, L., Welling, D. T., Viljanen, A., Honkonen, I., Boynton, R. J., & Yordanova, E. (2020). On the regional variability of db/dt and its significance to gic. *Space Weather*, 18(8), e2020SW002497.

Dungey, J. (1961). Interplanetary magnetic field and the auroral zones. *Phys. Rev. Lett.*, 6, 47–48.

Forbes, T. (2000). A review on the genesis of coronal mass ejection. *J. Geophys. Res.*, 105, 23153–23165.

Forsyth, C., Rae, I., Coxon, J., Freeman, M., Gjerloev, C. J. A. J., & Fazakerley, A. (2015). A new technique for determining substorm onsets and phases from indices of the electrojet (sophie). *J. Geophys. Res. Space Physics*, 120, 10,592–10,606.

Ganushkina, N., Liemohn, M., & Dubyagin, S. (2018). Current systems in the earth's magnetosphere. *Rev. Geophys.*, 56, 309–332.

Ganushkina, N., Liemohn, M., Dubyagin, S., Daglis, I., Dandouras, I., Zeeuw, D. D., Ebihara, Y., Ilie, R., Katus, R., Kubyshkina, M., Milan, S., Ohtani, S., Ostgaard, N., Reistad, J., Tenfjord, P., Toffoletto, F., Zaharia, S., & Amariutei, O. (2015). Defining and resolving current systems in geospace. *Annales Geophysicae*, 33, 1369–1402.

Gjerloev, J. W. (2009). A global ground-based magnetometer initiative. *EOS*, 90, 230–231.

Gjerloev, J. W. (2012). The supermag data processing technique. *J. Geophys. Res.*, 117, A09213.

Gjerloev, J. W., Hoffman, R. A., Friel, M. M., Frank, L. A., & Sigwarth, J. B. (2004). Substorm behavior of the auroral electrojet indices. *Ann. Geophys.*, 22, 2135–2149.

Gonzales, W., Joselyn, J., Kamide, Y., Kroehl, H., Rostoker, G., Tsurutani, B., & Vasyliunas, V. (1994). What is a geomagnetic storm? *J. Geophys. Res.*, 99, 5771–5792.

Hathaway, D. (2015). The solar cycle. *Living Rev. Solar Phys.*, 12, 4.

Hughes, W. (1995). *Introduction to Space Physics*, (pp. 227). Cambridge university press.

Iijima, T. & Potemra, T. (1967). Field-aligned currents in the dayside cusp observed by triad. *J. Geophys. Res.*, 81, 5971–5979.

Iijima, T. & Potemra, T. (1982). The relationship between interplanetary quantities and birkeland current densities. *Geophys. Res. Lett.*, 9, 442–445.

Jokipii, J. & Thomas, B. (1981). Effects of drift on the transport of cosmic rays iv. modulation by a wavy interplanetary current sheet. *The Astrophysical Journal*, 243, 1115–1122.

Jorgensen, A., Spence, H., Hughes, W., & Singer, H. (2004). A statistical study of the global structure of the ring current. *J. Geophys. Res.*, 109, A12204.

Kamide, Y., Perreault, P., Akasofu, S.-I., & Winningham, J. (1977). Dependence of substorm occurrence probability on the interplanetary magnetic field and on the size of the auroral oval. *J. Geophys. Res.*, 82, 5521–5528.

Kan, J. & Lee, L. (1979). Energy coupling and the solar wind dynamo. *Geophys. Res. Lett.*, 6, 577–580.

Karinen, A. & Mursula, K. (2005). A new reconstruction of the dst index for 1932–2002. *Ann. Geophys.*, 23, 475–485.

Karinen, A. & Mursula, K. (2006). Correcting the dst index: Consequences for absolute level and correlations. *J. Geophys. Res*, 111, A08207.

Keiling, A., Angelopoulos, V., Runov, A., Weygand, J., Apatenkov, S., Mende, S., McFadden, J., Larson, D., Amm, O., Glassmeier, K.-H., & Auster, H. U. (2009). Substorm current wedge driven by plasma flow vortices: Themis observations. *J. Geophys. Res.*, 114, A00C22.

Kepko, L., McPherron, R., Amm, O., et al. (2015). Substorm current wedge revisited. *Space. Sci. Rev.*, 190, 1–46.

Kilpua, E., Balogh, A., von Steiger, R., & Liu, Y. (2017). Geoeffective properties of solar transients and stream interaction regions. *Space. Sci. Rev.*, 212, 1271–1314.

King, J. & Papitashvili, N. (2005). Solar wind spatial scales in and comparisons of hourly wind and ace plasma and magnetic field data. *J. Geophys. Res.*, 110, A02104.

Kivelson, M. & Russell, C. (1995). *Introduction to Space Physics*. Cambridge university press.

Koskinen, H. (2011). *Physics of space storms, from solar surface to the earth*. Springer Berlin, Heidelberg.

Koskinen, H. & Kilpua, E. (2022). *Physics of Earth's Radiation Belts: Theory and Observations*. Springer Nature.

Le, G., Russell, C., & Takahashi, K. (2004). Morphology of the ring current derived from magnetic field observations. *Ann. Geophys.*, 22, 1267—-1295.

Lepping, R., Jones, J., & Burlaga, L. (1990). Magnetic field structure of interplanetary magnetic clouds at 1 au. *J. Geophys. Res.*, 95, 11957–11965.

Lockwood, M., Bentley, S., Owens, M., Barnard, L., Scott, C., Watt, C., & Allanson, O. (2019). The development of a space climatology: 1. solar wind magnetosphere coupling as a function of time scale and the effect of data gaps. *Space Weather*, 17, 133—-156.

Lockwood, M., Owens, M. J., Barnard, L. A., Haines, C., Scott, C. J., McWilliams, K. A., & Coxon, J. C. (2020a). Semi-annual, annual and universal time variations in the magnetosphere and in geomagnetic activity: 1. geomagnetic data. *J. Space Weather Space Clim.*, 10, 23.

Lockwood, M., Owens, M. J., Barnard, L. A., Watt, C. E., Scott, C. J., Coxon, J. C., & McWilliams, K. A. (2020b). Semi-annual, annual and universal time variations in the magnetosphere and in geomagnetic activity: 3. modelling. *J. Space Weather Space Clim.*, 10, 61.

Lui, A. (1991). A synthesis of magnetospheric substorm models. *J. Geophys. Res.*, 96, 1849–1856.

Lui, A. (1996). Current disruption in the earth's magnetosphere: Observations and models. *J. Geophys. Res.*, 101, 13067–13088.

Lui, A., McEntire, R., & Krimigis, S. (1987). Evolution of the ring current during two geomagnetic storms. *J. Geophys. Res.*, 92, 7459–7470.

Lyatsky, W., Newell, P., & Hamza, A. (2001). Solar illumination as cause of the equinoctial preference for geomagnetic activity. *Geophys. Res. Lett.*, 28, 2353–2356.

McPherron, R. (1970). Growth phase of magnetospheric substorms. *J. Geophys. Res.*, 75, 5592–5599.

McPherron, R. (1972). Substorm related changes in the geomagnetic tail: the growth phase. *Planet. Space Sci.*, 20, 1521.

McPherron, R. (1979). Magnetospheric substorms. *Rev. Geophys.*, 17, 657–681.

McPherron, R. & Chu, X. (2017). The mid-latitude positive bay and the mpb index of substorm activity. *Space. Sci. Rev.*, 206, 91—122.

McPherron, R. & Chu, X. (2018). The midlatitude positive bay index and the statistics of substorm occurrence. *J. Geophys. Res. Space Physics*, 123, 2831–2850.

McPherron, R., Russell, C., & Aubry, M. (1973). Satellite studies of magnetospheric substorms on august 15, 1968 9. phenomenological model for substorm. *J. Geophys. Res.*, 78, 3131–3149.

Milan, S., Provan, G., & Hubert, B. (2007). Magnetic flux transport in the dungey cycle: A survey of dayside and nightside reconnection rates. *J. Geophys. Res.*, 112, A01209.

Milan, S. E., Boakes, P., & Hubert, B. (2008). Response of the expanding/contracting polar cap to weak and strong solar wind driving: Implications for substorm onset. *J. Geophys. Res.*, 113, A09215.

Milan, S. E., Lester, M., Cowley, S. W. H., Oksavik, K., Brittnacher, M., Greenwald, R. A., Sofko, G., & Villain, J.-P. (2003). Variations in the polar cap area during two substorm cycles. *Ann. Geophys.*, 21, 1121–1140.

Nagai, T., Fujimoto, M., Saito, Y., Machida, S., Terasawa, T., Nakamura, R., Yamamoto, T., Mukai, T., Nishida, A., & Kokubun, S. (1998). Structure and dynamics of magnetic reconnection for substorm onsets with geotail observations. *J. Geophys. Res.*, 103, 4419–4440.

Ness, N. (1965). The earth's magnetic tail. *J. Geophys. Res.*, 70, 2989—-3005.

Newell, P. & Gjerloev, J. W. (2011). Evaluation of supermag auroral electrojet indices as indicators of substorms and auroral power. *J. Geophys. Res.*, 116, A12211.

Newell, P., Sotirelis, T., Liou, K., Meng, C.-I., & Rich, F. J. (2007). A nearly universal solar wind-magnetosphere coupling function inferred from 10 magnetospheric state variables. *J. Geophys. Res.*, 112, A01206.

Nishida, A. (1966). Formation of plasmapause, or magnetospheric plasma knee, by the combined action of magnetospheric convection and plasma escape from the tail. *J. Geophys. Res.*, 71, 5669–5679.

Owens, M. & Forsyth, R. (2013). The heliospheric magnetic field. *Living Rev. Solar Phys.*, 10, 5.

Parker, E. (1958). Dynamics of the interplanetary gas and magnetic fields. *Astrophys. J.*, 128, 664—-676.

Parker, E. (1963). The solar-flare phenomenon and the theory of reconnection and annihilation of magnetic fields. *Astrophys. J. Suppl. Ser*, 8, 177–211.

Perreault, W. & Akasofu, S.-I. (1978). A study of geomagnetic storms. *Geophys. J. R. Astron. Soc.*, 54, 547.

Petrinec, S. & Russell, C. (1996). Near-earth magnetotail shape and size as determined from the magnetopause flaring angle. *J. Geophys. Res.*, 110, 137–152.

Petschek, H. (1964). Magnetic field annihilation, in aas-masa symposium on physics of solar flares. *NASA Spec. Publ.*, 50, 425.

Pirjola, R. (2000). Geomagnetically induced currents during magnetic storms. *IEEE Transactions on Plasma Science*, 28, 1867–1873.

Pulkkinen, A., Bernabeu, E., Eichner, J., Viljanen, A., & Ngwira, C. (2015). Regional-scale high-latitude extreme geoelectric fields pertaining to geomagnetically induced currents. *Earth, Planets and Space*, 67.

Pulkkinen, A., Bernabeu, E., Thomson, A., Viljanen, A., Pirjola, R., Boteler, D., Eichner, J., Cilliers, P. J., Welling, D., Savani, N. P., Weigel, R. S., Love, J. J., Balch, C., Ngwira, C. M., Crowley, G., Schultz, A., Kataoka, R., Anderson, B., Fugate, D., Simpson, J. J., & MacAlester, M. (2017). Geomagnetically induced currents: Science, engineering, and applications readiness. *Space Weather*, 15(7), 828–856.

Pulkkinen, A., Pirjola, R., & Viljanen, A. (2008). Statistics of extreme geomagnetically inducedcurrent events. *Space Weather*, 6, S07001.

Richardson, I., Cane, H., & Cliver, E. (2002). Sources of geomagnetic activity during nearly three solar cycles. *J. Geophys. Res.*, 107, 1187.

Richardson, I., Cliver, E., & Cane, H. (2000). Sources of geomagnetic activity over the solar cycles: Relative importance of coronal mass ejections, high-speed streams, and slow solar wind. *J. Geophys. Res.*, 105, 18203–18213.

Rostoker, G. (1972). Geomagnetic indices. *Rev. Geophys. and Spa. Phys.*, 10, 935–950.

Rostoker, G., Akasofu, S.-I., Foster, J., Greenwald, R., Kamide, Y., Kawasaki, K., Lui, A., McPherron, R., & Russell, C. (1980). Magnetospheric substorms—definition and signatures. *J. Geophys. Res.*, 85, 1663–1668.

Russell, C., Luhmann, J., & Strangeway, R. (2017). *Space Physics an Introduction*. Cambridge university press.

Russell, C. & McPherron, R. (1973). Semiannual variation of geomagnetic activity. *J. Geophys. Res.*, 78, 92–108.

Sergeev, V. A., Angelopoulos, V., & Nakamura, R. (2012). Recent advances in understanding substorm dynamics. *Geophys. Res. Lett.*, 39, L05101.

Shukhtina, M. A., Dmitrieva, N. P., & Sergeev, V. A. (2004). Quantitative magnetotail characteristics of different magnetospheric states. *Ann. Geophys.*, 22, 1019–1032.

Singer, S. (1958). Radiation belt' and trapped cosmic ray albedo. *Physical Review Letters*, 1, 173.

Singh, A., Singh, R., & Siingh, D. (2011). State studies of earth's plasmasphere: A review. *Planetary and Space Science*, 59, 810–834.

Siscoe, G. & Huang, T. (1985). Polar cap inflation and deflation. *J. Geophys. Res.*, 90, 543–547.

Smith, E. & Tsurutani, B. (1978). Observations of the interplanetary sector structure up to heliographic latitudes of 16: Pioneer 11. *J. Geophys. Res.*, 83, 717–724.

Stern, D. (1983). The origins of birkeland currents. *Reviews of Geophysics*, 21, 125–138.

Stern, D. (1989). A brief history of magnetospheric physics before the spaceflight era. *Rev. Geophys.*, 27, 103–114.

Sugiura, M. (1964). Hourly values of equatorial dst for the igy. *Ann. Int. Geophys. Year*, 95, 9.

Sweet, P. (1958). The production of high energy particles in solar flares. *Nuovo Cim*, 8, 188–196.

Tanskanen, E., Pulkkinen, T., Viljanen, A., Mursula, K., Partamies, N., & Slavin, J. (2011). From space weather toward space climate time scales: Substorm analysis from 1993 to 2008. *J. Geophys. Res.*, 116, A00I34.

Tanskanen, E., Viljanen, A., Pulkkinen, T., Pirjola, R., Hikkinen, L., Pulkkinen, A., & Amm, O. (2001). At substorm onset, 40% of al comes from underground. *J. Geophys. Res.*, 106(A7), 13,119–13,134.

Tanskanen, E. I. (2009). A comprehensive high-throughput analysis of substorms observed by image magnetometer network: Years 1993–2003 examined. *J. Geophys. Res.*, 114, A05204.

Tsurutani, B. T., Gonzalez, W. D., Gonzalez, A. L. C., Guarnieri, F. L., Gopalswamy, N., Grande, M., Kamide, Y., Kasahara, Y., Lu, G., Mann, I., McPherron, R., Soraas, F., & Vasyliunas, V. (2006). Corotating solar wind streams and recurrent geomagnetic activity: A review. *J. Geophys. Res.*, 111, A07S01.

Vasyliunas, V. (1970). *Mathematical models of magnetospheric convection and its coupling to the ionosphere, in Particles and Fields in the Magnetosphere, ed. by B.M. McCormac.* p. 60.

Wang, H. & Lühr, H. (2007). Seasonal-longitudinal variation of substorm occurrence frequency: Evidence for ionospheric control. *Geophys. Res. Lett.*, 34, L07104.

Yamada, M., Kulsrud, R., & Hantao, J. (2010). Magnetic reconnection. *Rev. Mod. Phys.*, 82, 603–664.

Yao, Z. H., Pu, Z. Y., Fu, S. Y., Angelopoulos, V., Kubyshkina, M., Xing, X., Lyons, L., Nishimura, Y., Xie, L., Wang, X. G., Xiao, C. J., Cao, X., Liu, J., Zhang, H., Nowada, M., Zong, Q. G., Guo, R. L., Zhong, J., & Li, J. X. (2012). Mechanism of substorm current wedge formation: Themis observations. *Geophys. Res. Lett.*, 39, L13102.

Zirker, J. (1977). Coronal holes and high-speed wind streams. *Reviews of Geophysics and Space Physics*, 15(3), 257–269.